Muon Pair Production

in

Electron-Proton Collisions

vorgelegt von

Diplom-Physiker

Boris Leißner

aus Rheydt

Kurzfassung

Ereignisse mit mindestens zwei isolierten Myonen hoher invarianter Masse, die in Endzuständen der Elektron-Proton Streuung am HERA Speicherring auftreten, wurden mit dem H1 Detektor bei einer Schwerpunktsenergie von $\sqrt{s} = 318$ GeV gemessen. Die analysierten Daten entsprachen einer integrierten Luminosität von 70.9 pb^{-1}. Myonpaarproduktion, erzeugt durch die Wechselwirkung zweier Photonen, beherrscht hauptsächlich die Vorhersage des Standardmodells, die gut mit der Messung übereinstimmt. Signaturen, die über das Standardmodell hinausgehen, konnten nicht entdeckt werden.

Abstract

Events containing pairs of isolated muons at high invariant masses have been detected at HERA with the H1 detector in a data sample corresponding to an integrated luminosity of 70.9 pb^{-1} of $e^{\pm}p$ scattering at $\sqrt{s} = 318$ GeV. The results are well described by the Standard Model prediction which is dominated by photon-photon collisions. No evidence of processes beyond the standard model has been observed.

Contents

Introduction

Presently the Standard Model comprises our knowledge of the structure of matter. Three of the four fundamental forces are unified within the Standard Model: the electromagnetic, the strong and the weak interactions. The theory of Quantum Electrodynamics (QED) allows us to understand electromagnetic interactions, strong interactions are described by Quantum Chromo-dynamics (QCD). The electroweak theory (EW) unifies electromagnetic and weak interactions.

Scattering experiments proof the validity of the Standard Model and aim to access the physics beyond the Standard Model (BSM) at highest centre of mass energies. Supersymmetric theories (SUSY) are the most popular extensions. To perform a search for new physics it has to be proven that the present theories are really understood and that experimentalists do fully control their devices. The best candidates for searches are clear signatures in the detector: isolated leptons and especially isolated muons.

In electron-proton scattering the proton structure is probed by a photon probe emitted from the electron side. If also the proton emits a photon, the domain of two-photon physics is entered, which has been analysed in detail at e^+e^- colliders. At electron-proton machines photon-photon scattering is the dominant production process for muon pairs at high energetic scales. Muon pairs, which are produced via this QED process, form the dominant background source for almost all processes with muons in the final state. A single muon event may be easily faked, if one muon of the pair remains undetected. The undetected muon may be misinterpreted as a neutrino.

In comparison with e^+e^- colliders the scattering situation at ep-colliders is much more complicated due to the structure of the proton. Knowledge from a large variety of former experiments enters the description of the proton. It has to be proofed that this covers the whole relevant phase space.

Thus the task is clear: the main QED process has to be measured. It must be shown that muon pair production is very well understood in a phase space as large as possible. Examining differential distributions it will then be possible to recognise discrepancies from the Standard Model prediction. After having understood di-muon production one is prepared to investigate all other muon channels.

Let us review some experimental results. The list of the latest HERA-results comprises:

- H1 and Zeus have observed an Υ signal in the muon channel [H100, Zeu98].
  Both analyses were based on low luminosity data samples (27.5 pb^{-1} and 43.2 pb^{-1}), and would be improved by increased statistics.

- In a search for events with a high energy isolated lepton and missing transverse momentum at the H1 experiment an excess of about 4.8 standard deviations from the Standard Model has been observed [H198, Mal00, H102d]. Table 1.1 list the observed and predicted event rates for different cuts on the transverse hadronic momentum P_T^X.

P_T^X	Data	SM	W
> 12 GeV	13	5.1 ± 1.3	4.2 ± 1.3
> 25 GeV	10	2.8 ± 0.7	2.3 ± 0.7
> 40 GeV	6	1.0 ± 0.3	0.9 ± 0.3

Table 1.1: *Observed and predicted events rates in the electron and muon channel combined for all e^+p data.*

While H1 reports an excess of 4.8 standard deviations in the highest P_t^X bin, the measurement of the Zeus collaboration is in good agreement with the standard model [Zeu00]. The question which has to be answered is whether the distribution of the hadronic transverse momentum in the di-muon channel is well described. Missing transverse momentum may arise also from measurement errors. In the di-muon channel this is the only source of missing transverse momentum within the Standard Model. It is obligatory to check the distribution of the missing transverse momentum in this channel.

- In an analysis of multi electron events H1 has observed six events with a di-electron mass greater than 100 GeV [H102e, Val02]. Three events have been attributed to a sample of two visible electrons (2e) and the other three events to a a sample of three visible electrons (3e). In each sample about 0.25 events are expected.
  Are these events also observable in the muon channel?

Thus there are a number of open question in leptonic channels which are worthwhile to be analysed in detail. All of them involve final states with at least two leptons, if the missing transverse momentum is interpreted as a neutrino, which is the only standard model explanation. The possible combinations for at least two leptons in the final state are listed in table 1.2. Since the identification of τ-leptons is experimentally much more difficult, a τ signature cannot be assigned as 'clear signature' and hence is omitted. Six different combinations have to be considered. Experimentally, a final state with two neutrinos is not accessible. The neutrino has only to be considered together with an electron or muon, which typically stems from the decay of a W-boson and forms the Standard Model interpretation of the 'isolated leptons with

missing transverse momentum'. Remaining are the lepton pair combinations ee and $\mu\mu$ and the combination μe. The uncovered topics are the di-muon and the muon-electron channel. The analysis of the $\mu\mu$ channel is presented in this work[1]. In total an integrated luminosity of 70.9 pb^{-1} of $e^{\pm}p$-scattering at centre of mass energies of $\sqrt{s} \approx 318$ GeV have been analysed. Within the Standard Model a relevant high-P_t process with μe pairs in the final state does not exist. The most probable explanation for such a signature is the combination of a muon with the scattered beam electron. The μe signature is necessary for a complete comparison of muonic and electronic channels, because combinations of one lepton with the beam-lepton are naturally contained in the ee signature.

Signature	SM Process	Excess in H1 data
$\mu\mu$	Z^0-Production, $\gamma\gamma$ process	**NONE !!**
ee	Z^0-Production, $\gamma\gamma$ process	**YES**
$\nu\nu$	*not observable*	
$\mu\nu$	W-Production	**YES**
$e\nu$	W-Production	**YES**
μe	***no direct process***	**??**

Table 1.2: *Combinations of at least two leptons in the final state.*

Three out of five observable signatures reveal excesses of more than 4 standard deviations from the Standard Model. Is there an underlying common process behind this? This question may be posed, but it should be pointed out straight away that the observed topology of these processes is completely different. The multi-electron events occur preferably as elastic or quasi-elastic events while the excess in events with the lepton neutrino topology is seen at large hadronic transverse momenta, thus in inelastic events.

---

[1]The results of this analysis are H1-Preliminary and appeared partly in [Lei02, H102c].

Production of Muons

Multi muon events appearing in the final state of electron (e) - proton (p) scattering stem almost completely from muon pair production. The muon pairs are produced in elastic (2.1) and inelastic (2.2) scattering processes:

$$ep \longrightarrow e'p'\mu^+\mu^- \tag{2.1}$$
$$ep \longrightarrow e'X\mu^+\mu^-. \tag{2.2}$$

The final state of these reactions consists of two muons μ, the scattered electron e' and the scattered proton p' (2.1) or a more complex hadronic system X (2.2). If both scattered particle are lost in the beam pipe, only two muons are contained in the detector.

The cross section calculation of these processes is complicated, even the one of the simple $2 \longrightarrow 4$ process (2.1) is not trivial due to the structure of the proton. A simplification of the calculation may be achieved by reducing the multi-particle processes to $2 \longrightarrow 2$ scattering reactions. At high di-muon masses electroweak processes form the only notable source of muon pair production. Especially quasi-real two photon collisions lead to such signatures in the detector. Two-photon physics allows to formulate the cross section in a good approximation as product of photon fluxes and the central $2 \longrightarrow 2$ process: $\gamma\gamma \longrightarrow \mu^+\mu^-$. The decay of heavy particles produces muons at lower di-muon mass scales and non isolated single muons.

An overview of single and di-muon production processes is given in table 2.1. The first group contains the electroweak muon pair production processes (section 2.1). Interactions of two neutral gauge bosons and in particular photon-photon collisions $\gamma\gamma \longrightarrow \mu^-\mu^+$ are the most relevant source of muon pairs. In addition Bremsstrahlungs processes with subsequent photon conversion into muon pairs occur. Also electroweak effects, especially the Z^0-production, which is Bremsstrahlung of the Z-Boson with a subsequent conversion into a muon pair, may be observed. The decay of the vector meson resonances completes the description of lepton pair production within the standard model (section 2.2).

Electroweak Muon Pair Production [1] [2] :

Two-boson	ep	$\longrightarrow$	$ep\gamma\gamma$	$\hookrightarrow$	$\gamma\gamma$	$\longrightarrow$	$\mu^+\mu^-$
	ep	$\longrightarrow$	$ep\gamma Z^0$	$\hookrightarrow$	γZ^0	$\longrightarrow$	$\mu^+\mu^-$
	ep	$\longrightarrow$	$epZ^0 Z^0$	$\hookrightarrow$	$Z^0 Z^0$	$\longrightarrow$	$\mu^+\mu^-$
Bremsstrahlung			ep	$\longrightarrow$	$ep\gamma$	$\longrightarrow$	$ep\mu^+\mu^-$
Z^0-production			ep	$\longrightarrow$	epZ^0	$\longrightarrow$	$ep\mu^+\mu^-$

Decay of Vector Meson Resonances:

J/Ψ decay	J/Ψ	$\longrightarrow$	$\mu^+\mu^-$
Υ decay	Υ	$\longrightarrow$	$\mu^+\mu^-$

Single Muon Production:

Heavy quark decay	Q	$\longrightarrow$	$q\mu\nu$
τ decay	τ	$\longrightarrow$	$\mu\nu_\mu\nu_\tau$
W decay	W	$\longrightarrow$	$\mu\nu$

Table 2.1: *Sources of muon production. The upper two groups contain the pair production mechanisms and the lower one collects single muon production processes.*

Single leptons result mainly from semileptonic heavy quark decays in boson-gluon fusion. Another source of single muon production is given by the decay of a τ lepton. Via these mechanisms also two muons in the final state may be produced. At large transverse momenta single muons stemming from the decay of W-bosons are expected (section 2.3). Finally the Monte Carlo Generators which are necessary for the generation and simulation of the different production processes are presented (section 2.5).

---

[1]Following the process classification used at LEP (eg.: [OPA93]), where 4 processes are distinguished namely Annihilation, Conversion, Bremsstrahlung and Multiperipheral (two-photon process). Annihilation and Conversion do not occur in ep scattering, while the Feynman diagrams of the Bremsstrahlungs process and the two-photon process in e^+e^- and ep scattering have the same structure. The Bremsstrahlungs processes are also referred to as 'QED Compton' processes. A naming convention introduced in [Art91] contraproductively assigns the two-photon process as 'Bethe-Heitler' process. This causes confusion since at HERA this expression refers to the Bremsstrahlungs process which is used to measure the Luminosity. Especially here these two processes have to be distinguished. Bethe and Heitler calculated the Bremsstrahlung of an electron in a potential and electron pair production in an external field, whose corresponding Feynman diagram contains a kernel similar to the two-photon process [Bet34].

[2]Charged Current Pair Production processes are strongly suppressed and thus omitted.

2.1 Electroweak Muon Pair Production

2.1.1 Two-Photon Process

The cross section determination of the multi-particle reactions $ep \longrightarrow ep\mu\mu$ and $ep \longrightarrow eX\mu\mu$ may be simplified by identifying suitable $2 \longrightarrow 2$ reactions which allow to reduce these complex reactions. Since the first calculation of Weizs"acker and Williams this is a popular access to the cross section expression of complex scattering situations. Electroweak muon pair production of the type which is depicted in the Feynman diagram in figure 2.1 dominates the electroweak production mechanisms. A photon emitted from the electron line interacts with a photon emitted from the proton side and produces a lepton pair. In the Feynman diagram the two-photon collision $\gamma\gamma \longrightarrow \mu^+\mu^-$ can be identified as a suitable $2 \longrightarrow 2$ subprocess. The full cross section is derived by folding the two-photon cross section with the corresponding photon flux. For the complete electroweak calculation the two-boson processes $Z^0\gamma \longrightarrow \mu^+\mu^-$ and $Z^0Z^0 \longrightarrow \mu^+\mu^-$ have to be considered in addition. Due to the large mass of the Z^0-boson in the propagator the latter processes are strongly suppressed.

Kinematics

The kinematics of the two-photon process which is depicted in figure 2.1 as elastic process, is determined by the virtualities of the two-photons Q_e^2 and Q_p^2 and the centre of mass energy in the photon-photon system $\sqrt{\hat{s}}$, which is the invariant mass of the produced muon pair. These kinematical variables can be derived from the incoming and outgoing beam particles, which are characterised by their four-momenta:

- p the momentum of the incoming proton

- k the momentum of the incoming electron

- p' the momentum of the outgoing proton

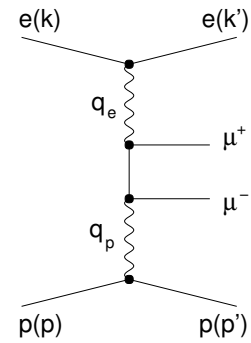- k' the momentum of the outgoing electron

Figure 2.1: *Kinematics of the two-photon process.*

The virtualities of the two photons is the negative squared momentum transfer of the respective photon:

$$Q_e^2 = -q_e^2 = -(k - k')^2, \qquad Q_p^2 = -q_p^2 = -(p - p')^2. \qquad (2.3)$$

The centre of mass energy $\sqrt{s}$ follows from

$$s = (p + k)^2. \tag{2.4}$$

The centre of mass energy $\sqrt{\hat{s}}$ in the two-photon system can be calculated from the four-momenta of the photons or from the four-momenta of the produced leptons $p_{\mu,1}$ and $p_{\mu,2}$:

$$\hat{s} = (q_e + q_p)^2 = (p_{\mu,1} + p_{\mu,2})^2. \tag{2.5}$$

The index P denotes always the 'proton side' and applies in the event of inelastic scattering for photons emitted from the quark. To characterise the central subprocess $\gamma\gamma \longrightarrow \mu^+\mu^-$ the Mandelstam variables $\hat{s}$, t and u are used.

Photon-Photon Collisions

In a convenient way the cross section is expressed as product of the cross section of the central subprocess and photon fluxes:

- $\Gamma_e(Q_e^2, z_e)$ the photon flux from the electron side;

- $d\sigma(Q_e^2, Q_p^2, \hat{s}, t)$ the cross section of the central $\gamma\gamma$ subprocess;

- $\Gamma_p(Q_p^2, z_p)$ the photon flux from the proton side.

The variable z_e gives the relative energy loss of the electron and determines thus the photon energy $E_\gamma = z_e \cdot E$, while z_p is the corresponding variable at the proton side.

Exchanged photons are virtual particles and may be longitudinal or transversal polarised. Real photons give the dominant contribution to the cross section. In the Photoproduction limit, $Q_e, Q_p \longrightarrow 0$, the cross section contribution of longitudinal polarised photons vanishes:

$$\frac{d\sigma(ep \longrightarrow ep\mu^+\mu^-)}{dQ_e^2 dQ_p^2 dz_e dz_p dt} = \Gamma_e^t \cdot \Gamma_p^t \cdot \frac{d\sigma(\gamma\gamma \longrightarrow \mu^+\mu^-)}{dt} + ... \tag{2.6}$$

Experimentally $Q_e \longrightarrow 0$ can be guaranteed by untagging the scattered electron, i.e. selecting events in which the scattered electron vanishes in the beam pipe.

The flux factor Γ_e^t gives the probability that a transversal polarised photon is radiated from the electron, i.e. the number of photons dN of the energy fraction between z_e and $z_e + dz_e$ and of the virtuality dQ_e^2:

$$\Gamma_e^t = \frac{dN}{dQ_e^2 dz_e} = \frac{\alpha}{2\pi z_e Q_e^2} \left(\left(1 + (1 - z_e)^2\right) - \frac{2m^2 z_e^2}{Q_e^2} \right). \tag{2.7}$$

Thus electrons emit predominantly low energetic photons collinear to their flight direction. The total number of emitted photons in the interval of $Q^2 > Q_{min}^2$ is derived by integrating Γ_e:

$$f_{\gamma/e}(z_e) = \int \Gamma_e^t dQ_e^2 = \frac{\alpha}{2\pi z_e} \left[\left(1 + (1 - z_e)^2\right) \ln \frac{Q_{max}^2}{Q_{min}^2} - 2(1 - z_e) \right], \tag{2.8}$$
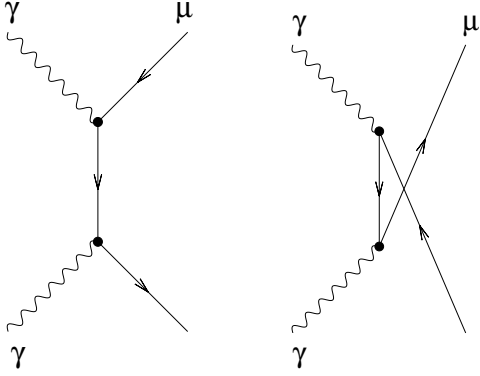
Figure 2.2: *Two-photon subprocess. Shown are the t-channel (right) and the u-channel (left) contribution.*

The term $2(1-z_e)$, which gives correction to the simplified Weizs"acker-Williams calculation, arises from the exact quantum mechanical calculations carried out by Kessler [Kes75]. The smallest possible momentum transfer is $Q^2_{min} = m^2 z_e^2/(1 - z_e)$.

In the event of electron-positron scattering the same calculation may be carried out for the other beam lepton. The product of the two photon fluxes yields to the luminosity function [Ber87], which can easily be evaluated [3]. The difference between e^+e^- and ep scattering arises from the different photon flux, whose description for the proton is much more complicated: elastic and inelastic scattering have to be distinguished. In the elastic case the electric and magnetic form factors G_E and G_M enter the description:

$$f_{\gamma/p}(z_p) = \frac{\alpha}{\pi z} \int \frac{1}{Q^2} \left((1 - z_p) \left(\frac{G_E^2}{Q^2} + \frac{G_M^2}{M_p^2} \right) (Q^2 - Q^2_{min}) + \frac{z_p^2}{2} G_M^2 \right) dQ^2, \qquad (2.9)$$

while in the deep inelastic case the photon flux can be expressed as a convolution of the photon flux from a quark $f_{\gamma/q}^{QPM}$ with the probability to find a quark in the proton $f_{q/p}(z_p)$:

$$f_{\gamma/p}(z_p) = \int f_{q/p}(x) \cdot f_{\gamma/q}^{QPM}(\frac{z_p}{x}) dx. \qquad (2.10)$$

The flux factor $f_{\gamma/q}^{QPM}$ can be derived from equation 2.8 considering the different charge quantum number of the quark by an additional factor e_q^2.

If the central subprocess is treated as collision of two real photons, it depends only on the centre of mass energy of the two-photon system and the angle between the final state leptons:

$$\frac{\sigma(Q_e^2, Q_p^2, \hat{s}, t)}{dt} = \frac{\sigma(\hat{s}, t)}{dt}. \qquad (2.11)$$

In figure 2.2 the lowest order Feynman diagrams of the central subprocess $\gamma\gamma \longrightarrow \mu^+\mu^-$ are shown. The two diagrams represent the t and the u-channel. Neglecting the lepton masses the cross section for the central subprocess can be derived from cross section for Compton scattering

---

[3]Observations of the two-photon process at LEP can be found in [OPA93].

via crossing, i.e. via the replacement $s \leftrightarrow t$ in the amplitudes and applying an additional factor (-1) for the fermion exchange [Ber02]:

$$\frac{d\sigma}{dt} = \frac{2\pi\alpha^2}{\hat{s}} \left(\frac{u}{t} + \frac{t}{u} \right) \tag{2.12}$$

The two poles of the scattering amplitude $(u, t \longrightarrow 0)$ correspond to a forward and a backward peak of the cross section. In the centre of mass system of this reaction the Mandelstam variables u and t are related to the transverse momentum P_T:

$$t = -\frac{\hat{s}}{2} \left(1 - \sqrt{1 - \frac{4P_T^2}{\hat{s}}} \right) \qquad u = -\frac{\hat{s}}{2} \left(1 + \sqrt{1 - \frac{4P_T^2}{\hat{s}}} \right) \tag{2.13}$$

The centre of mass energy $\hat{s}$ of this reaction is the invariant mass of the muon pair.

2.1.2   Bremsstrahlung and Photon Conversion

Bremsstrahlungs type processes, in which the radiated photon converts into a muon pair, form the other important source of muon pair production. Four types of Feynman diagrams are contributing to this process class corresponding to Bremsstrahlung from each incoming and outgoing scattering particle (figure 2.3). Here the term 'Bremsstrahlung' is assigned to processes in which the radiated photon decays into a muon pair. Diagrams a) and c) represent the Bremsstrahlung from the electron and Diagrams b) and d) show the Bremsstrahlung from the quark side. The Bremsstrahlung from the electron line gives the major contribution of these diagrams, which agrees with conclusion from the ratio of the electron to the quark mass: $m_q \gg m_e$. In diagrams a) and c) the γe kernel represents the Feynman diagram for Compton Scattering. Diagram a) contains the u-pole and is thus dominant. A similar argument holds true for the diagrams b) and d). Thus the contribution of Bremsstrahlung with subsequent photon conversion may be well approximated by evaluating the contribution of the diagrams a) and b) only. The process shown in diagram a) may also be interpreted as 'internal conversion' of the photon, which is emitted from the quark, into an electron pair and a subsequent electron-positron scattering: $e^+ e^- \longrightarrow \mu^+ \mu^-$. This process is also referred to as 'Cabbibo-Parisi' process. In diagram b) the photon radiated from the electron converts into a quark pair of which one quark interacts with the incoming quark: $q\bar{q} \longrightarrow \mu^+ \mu^-$. This process is known as Drell-Yan process.

Cabbibo-Parisi Process

The calculation of the Cabbibo-Parisi processes may be carried out in analogy to the two-photon process: the cross section results from convoluting the probability to find an (anti-) electron in the proton $f_{e/p}$ with the cross section of the central subprocess:

$$\frac{d\sigma(ep \longrightarrow ep\mu^+\mu^-)}{dtdz} = f_{e/p} \cdot \frac{d\sigma(e^+ e^- \longrightarrow \mu^+\mu^-)}{dt}. \tag{2.14}$$
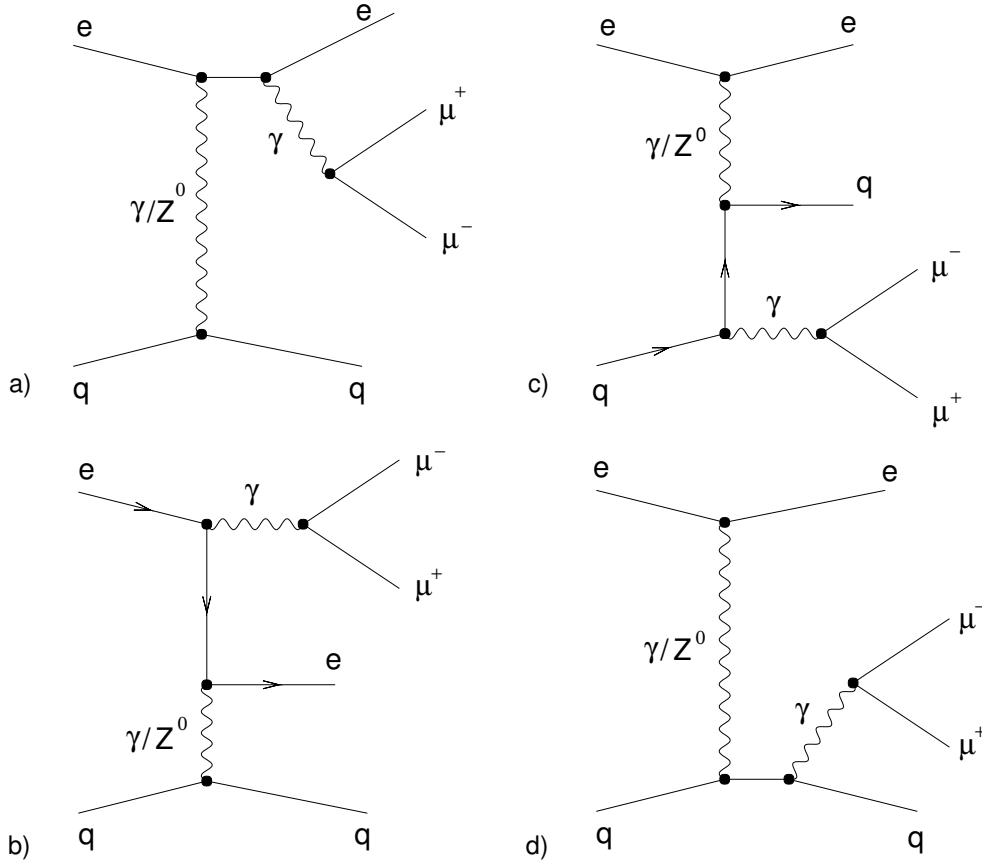
Figure 2.3: *Bremsstrahlungs processes (QED Compton). Diagrams a) and c) represent the Bremsstrahlung from the electron, b) and d) the Bremsstrahlung from the quark side. Diagram a) is referred to as Cabbibo-Parisi process. Diagram c) also assigned as Drell-Yan process.*

The electron flux from the proton is given by the convolution of the photon flux from the proton $f_{\gamma/p}$ and the probability to find an electron in the photon $f_{e/\gamma}$ [Art91]:

$$f_{e/p}(z) = \int_z^1 \frac{d\nu}{\nu} \int_{Q^2_{min}}^{Q^2_{max}} dQ^2 \Gamma_p(\nu) f_{e/\gamma}\left(\frac{z}{\nu}, Q^2\right). \tag{2.15}$$

The Cabbibo-Parisi process is the only electroweak muon pair production process, where the cross section for electron pair production is much larger than for muon production (figure 2.7). For muon pair production the cross section of the central subprocess $e^- e^+ \longrightarrow \mu\mu$ contains only the s-channel contribution [Ber02]:

$$\frac{d\sigma}{dt} = \frac{2\pi\alpha^2}{\hat{s}^2}\left(\frac{t^2 + u^2}{\hat{s}^2}\right).$$

Electron pairs are produced via Bhabha-scattering, which consist of a t- and a s-channel contribution [Ber02]:

$$\frac{d\sigma}{dt} = \frac{2\pi\alpha^2}{\hat{s}^2}\left(\frac{t^2 + u^2}{\hat{s}^2} + \frac{\hat{s}^2 + u^2}{t^2} + \frac{2u^2}{t\hat{s}}\right). \tag{2.16}$$

Due to the additional pole in the t-channel (2.16) the electron channel is enhanced drastically.
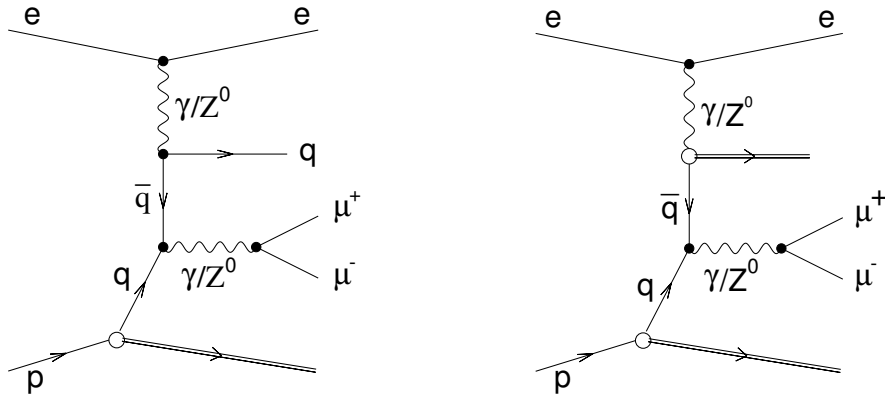
Figure 2.4: *Point-Like (left) and resolved (right) Drell-Yan process.*

Drell-Yan Process

The cross section of the Drell-Yan process may be approximated by the product of the quark flux $f_{q/e}$ from the electron and the cross section of the central subprocess $q\bar{q} \longrightarrow \mu^+\mu^-$:

$$\frac{d\sigma(ep \longrightarrow ep\mu^+\mu^-)}{dtdz} = f_{q/e} \cdot \frac{d\sigma(q\bar{q} \longrightarrow \mu^+\mu^-)}{dt}. \tag{2.17}$$

The cross section of the central subprocess has the same dependencies on the Mandelstam variables as equation (2.16). The quark flux $f_{q/e}$ is the convolution of the photon flux $f_{\gamma/e}$ with the probability that the photon converts into a quark pair $f_{q/\gamma}$ [Art91]. In the regime of Photoproduction ($Q_e^2 \longrightarrow 0$) the photon interaction cannot be described only as interaction of a point-like particle. The photon has to be interpreted as a particle with a partonic structure. In the Vector Meson Dominance Model [Sak69, Sch93] the photon $|\gamma>$ is interpreted as a superimposition of the bare photon $|\gamma_B>$ and hadronic components $|h>$:

$$|\gamma> = \sqrt{1-c^2}\,|\gamma_B> + c\,|h>, \tag{2.18}$$

where c is a normalisation factor. The state $|h>$ must have the same quantum number as the photon. For instance it can be a vector meson, eg. ρ^0, ω, ϕ. In a generalised model also heavier constituents are allowed.

Figure 2.4 shows a representation of the point-like process (left) and the resolved process (right), in which the resolved photon is symbolised by a small open circle. The photon is treated as point-like particle for high virtualities of the intermediate quark in the $\gamma q \longrightarrow \gamma q$ subprocess, while quasi-real quarks reveal the hadronic structure of the photon, which may be described by the Vector Meson Dominance Model. Events with a virtuality smaller than 25 GeV^2 are typically referred to as resolved. Generally the contribution of the resolved process to lepton pair production in ep physic is strongly suppressed. Since the Drell-Yan process gives access to the proton structure function, it has been investigated in detail whether it is not possible to observe
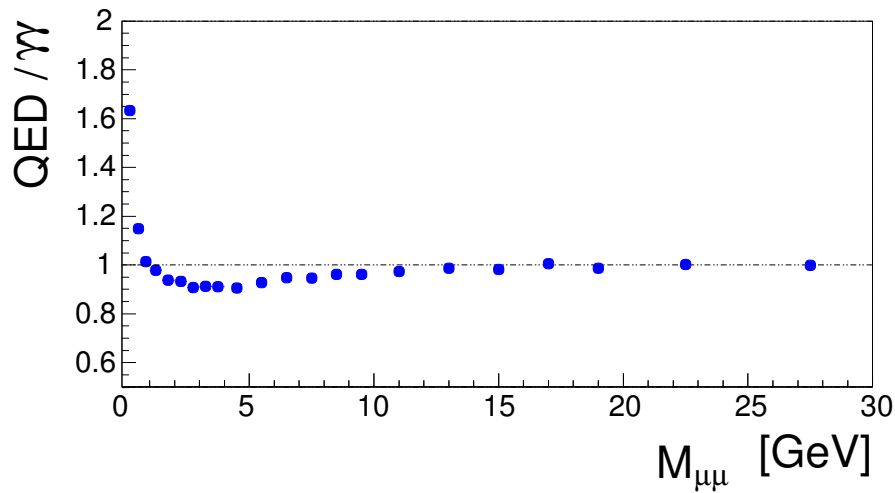
Figure 2.5: *Ratio of the cross sections between full QED calculation and two-photon process [Abepr]. At small masses the Bremsstrahlung (QED Compton) is enhancing the QED calculation, between 1 and 12 GeV a negative interference between the Bremsstrahlungs processes and the two-photon process is visible and at larger masses the influence of the Bremsstrahlungs contribution vanishes and thus the ratio of the full QED calculation and the two-photon process approaches one. The presented ratio is valid in the polar angle range $4° < \theta < 179°$.*

this process also in ep scattering [Baw93, Lev91]. Drell-Yan lepton pairs are extremely boosted into the proton direction. Therefore their θ-distribution is strongly peaking at small polar angles, but the prospects to separate it from the dominating two-photon process have found to be very small.

Bremsstrahlung and Two-Photon Process

The contribution of the Bremsstrahlungs processes become important at large transverse momenta and at low di-muon masses $M_{\mu,\mu}$. Therefore small opening angles are favoured. Figure 2.5 shows the ratio of the full QED calculation to the two-photon process as a function of the di-muon mass. A deviation from one results from the inclusion of the Bremsstrahlungs diagrams. At lowest masses the Bremsstrahlungs diagrams add significantly to the total cross section. In the mass region between 1 GeV and 12 GeV a negative interference is visible, while at large masses the effect of the QED Compton diagrams vanishes.

Effects of initial and final state radiation, in which the radiated photon does not convert into a muon pair, have to be distinguished from Bremsstrahlung with photon conversion. They will be exclusively referred to as 'radiative effects' or initial and final state radiation. These radiative effects are of lower order in α, since they do not contain a second vertex. Initial state radiation modifies the centre of mass energy and effects the cross section of lepton pair production mainly via the two-photon process.
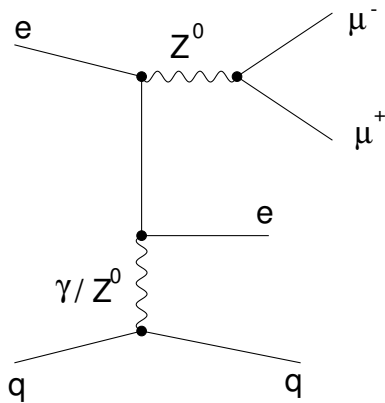
Figure 2.6: *Example of a Feynman diagram for Z^0-production. The omitted diagrams are in analogy to figure 2.3.*

2.1.3 Z^0-Production

Z^0-production can also be interpreted as a Bremsstrahlungs process, in which instead of the photon a Z^0-boson is radiated. The Feynman diagrams for Z^0-production can be derived from figure 2.6, if the the photon which is decaying into the muon pair is replaced by a Z^0-boson. Due to the large mass of the Z^0 the cross section for this process is very small. Theoretical calculations predict a total cross section of 0.34-0.43 pb for the inelastic Z-production and 0.117 pb for elastic Z^0-production [Bau92]. With a branching ratio of 3.367 % given by the Particle Data Group [PDG] a cross section of 0.012-0.014 pb for the inelastic process and 0.004 pb for the elastic process are expected.

2.1.4 P_T-Dependency of Electroweak Lepton Pair Production

All lepton pair production processes relevant at high transverse momenta ($P_T > 10$ GeV) have been introduced. Theoretical calculations [Art91] have been carried out to compare the different production mechanisms. Figure 2.7 shows the dependency of the transverse momenta P_T for the two-photon, the Cabbibo-Parisi and the Drell-Yan process. To cope with the strongly decreasing cross section, the y-axis shows the differential cross section $d\sigma/dP_T$ times P_T^3. The theoretical calculations extend only up to $P_T = 40$ GeV, which is just high enough to discuss effects relevant to this analysis.

The two-photon process is the dominating process almost over the entire phase space. The figure gives the contribution of elastic muon production ($\gamma\gamma_{ela}$), as well as the contribution of inelastic muon production ($\gamma\gamma_{ine}$) and the sum of the elastic and inelastic process ($\gamma\gamma_{tot}$). The elastic process exceeds the inelastic one at smaller transverse momenta P_T, while the inelastic process gives the major contribution at larger P_T. The figure indicates clearly that the dominance of the two-photon process gets weaker with increasing P_T. This behaviour may be explained with the Z^0-resonance which contributes to the Cabbibo-Parisi and to the Drell-Yan process. Due to the additional contribution of the annihilation diagram the cross section of the Cabbibo-Parisi
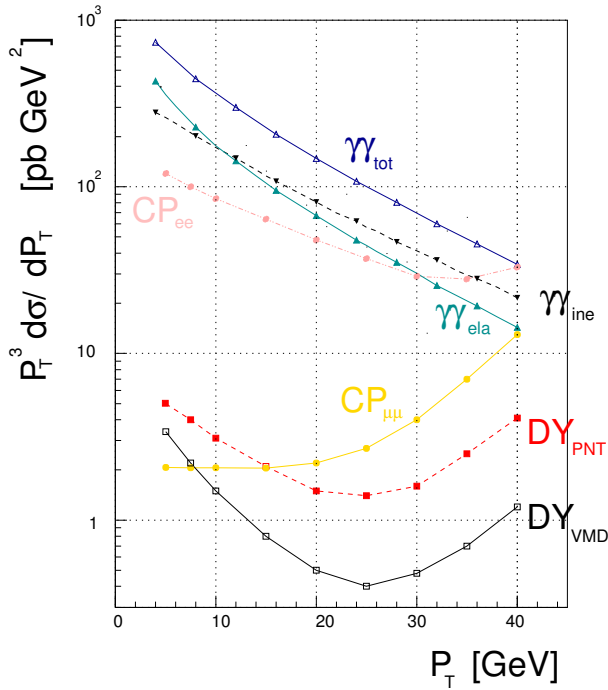
Figure 2.7: *High P_T lepton pair production [Art91]. All non resonant contributions to $P_T^3 \frac{d\sigma}{dP_T}$ are drawn as a function of the transverse momentum P_T of one of the two leptons. $\gamma\gamma_{tot}$ denotes the total two-photon process, $\gamma\gamma_{ela}$ the elastic two-photon process, $\gamma\gamma_{ine}$ the inelastic two-photon process, CP_{ee} gives the contribution of the Cabbibo-Parisi process in the electron channel and $CP_{\mu\mu}$ the one in the muon channel, DY_{PTN} and DY_{VMD} (multiplied by 10) refer to the point-like and resolved Drell-Yan process.*

process is much larger in the electron channel (CP_{ee}) than in the muon channel ($CP_{\mu\mu}$) 2.1.2. The contribution of the Drell-Yan process is always more than one order of magnitude smaller than the $\gamma\gamma$ contribution. The curve labelled DY_{PNT} shows the contribution of the Drell-Yan process in which the proton is assumed to be point-like and DY_{VMD} gives the contribution of the resolved Drell-Yan process.

2.2   Vector Meson Resonances

Resonant lepton pair production at HERA energies takes place via the decay of vector meson resonances, J/Ψ ($M_{J/\Psi} = 3.10$ GeV) and Υ. The vector mesons may be produced by means of diffraction or by photon-gluon fusion. The diffractive vector meson production is described in terms of the Regge phenomenology and the Vector Meson Dominance Model. The left Feynman diagram of figure 2.8 shows the diffractive Υ production. The exchanged photon fluctuates into an Υ-meson, which interacts with the proton under the exchange of a colourless object depicted

Resonance	Mass [GeV]	$BR_{\Upsilon \longrightarrow \mu\mu}$ [%]
$\Upsilon(1s)$	9.460	2.5
$\Upsilon(2s)$	10.023	1.3
$\Upsilon(3s)$	10.355	1.8

Table 2.2: *Υ-resonances. The mass and the branching ratio into muons are given for the first three Υ-resonances [PDG].*
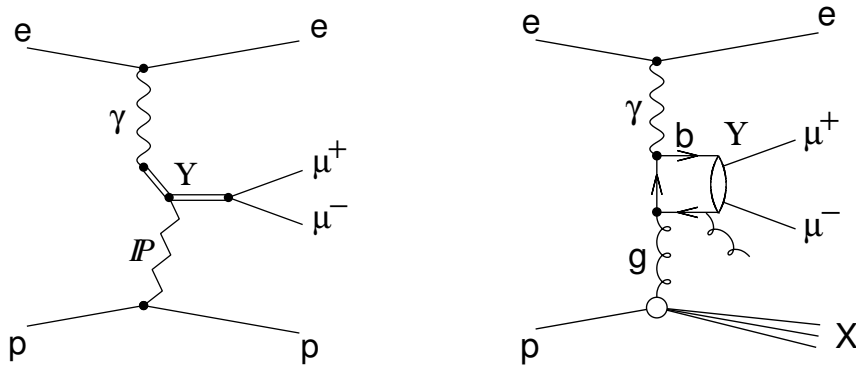
Figure 2.8: *Production of vector mesons. The left diagram shows the elastic Υ-production in the 'pomeron-model', the right one shows the inelastic process.*

as 'pomeron'. In QCD this colourless object may be realized by a two gluon exchange. The right Feynman diagram represents the Υ-production in photon-gluon fusion. The production of the colourless vector mesons occurs only in inelastic photon-gluon fusion reactions under the emission of a second gluon. Since the analysis is focused on high di-muon masses, only the Υ-contribution has to be considered. The Υ meson is interpreted as a bound $b\bar{b}$ system which occurs in different excited states. The most important ones are the $\Upsilon(1s)$, $\Upsilon(2s)$ and $\Upsilon(3s)$. The masses and the branching ratios into muons can be found in table 2.2. The ratio of the cross section for muon production of these three resonances is about 1:0.09:0.06 [Fra98]. Further information on this topic can be found in [Smi02], which presents a dedicated analysis of Υ production.

2.3   Single Muon Production

Boson-Gluon Fusion

Heavy quarks which are produced in boson-gluon fusion may decay semileptonically. Figure 2.9 shows such a boson-gluon fusion process with a subsequent decay of the produced quark into a lighter quark and a virtual W-boson, which decays into a muon and a muon neutrino. Dominant are the decay processes $b \longrightarrow cW^- \longrightarrow c\mu^-\bar{\nu}_\mu$ and $c \longrightarrow sW^+ \longrightarrow s\mu^+\nu_\mu$, while the decay $b \longrightarrow uW^-$ is suppressed due to the corresponding small matrix element of the 'CKM' Matrix. Contributing are also cascading decays which are initiated by the decay of a b-quark into a c-quark: $b \longrightarrow cW^-$. The products of this reaction may convert further. The resulting c-quark is allowed to decay semileptonically and produce a muon: $c \longrightarrow sW^+ \longrightarrow s\mu^+\nu_\mu$. Even the W^- boson contributes to the cascade by a conversion to light quarks: $W^- \longrightarrow \bar{c}s$, which can be the origin of a further semileptonic decay: $\bar{c} \longrightarrow \bar{s}W^- \longrightarrow \bar{s}\mu^-\bar{\nu}_\mu$. If both of the produced quarks decay semileptonically two muons may be found in the final state.
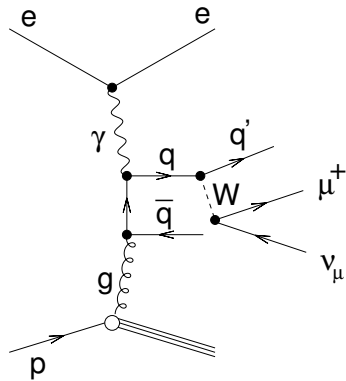
Figure 2.9: *Boson-gluon fusion process with semileptonic decay.*

τ Decays

τ leptons, which are produced in two-photon collisions, decay to 17.4 % into muons and two neutrinos. Via this process also two muons may be produced in the final state if both leptons of the τ pair decay into a muon. Mainly low momenta muons are produced via the τ decay.

W-Production

W production at HERA can take place via neutral and charged current interactions:

- $e^{\pm}p \longrightarrow e^{\pm}W^{\pm}X$

- $e^{+}p \longrightarrow \bar{\nu}W^{+}X$, $e^{-}p \longrightarrow \bar{\nu}W^{-}X$

Dominating are the neutral current type interactions, with a predicted cross section of 1.0-1.3 pb [Bau92]. The branching ratio of the W into muons is about 10 %. The dominating contribution to the cross section arises from the diagrams which are depicted in figure 2.10. A real W-boson is emitted from the incoming or outgoing quark line. These diagrams have the same topology as the Z^{0}-production in the Drell-Yan mode. Other processes are largely suppressed due to heavy boson masses in the propagator.

Figure 2.10: *Dominating Feynman diagrams for W-production.*

Figure 2.11: *Feynman diagrams for doubly charged Higgs production at HERA.*

2.4 Beyond the Standard Model

In extensions of the Standard Model equally charged lepton pair production appears as a promising discovery channel. Especially in the muon channel this topology offers an almost background free search channel, since the standard model contri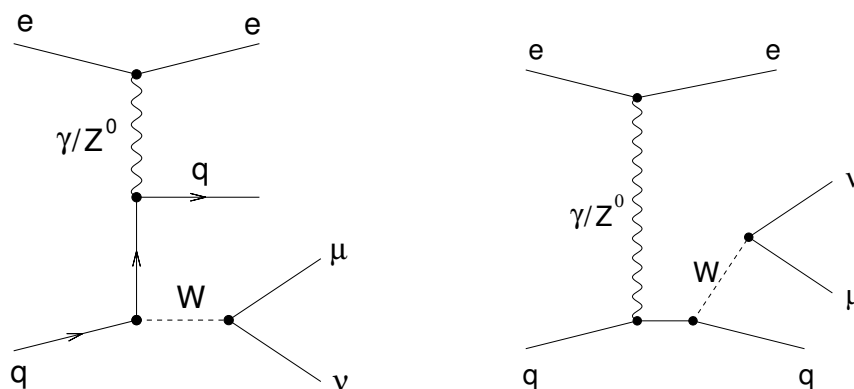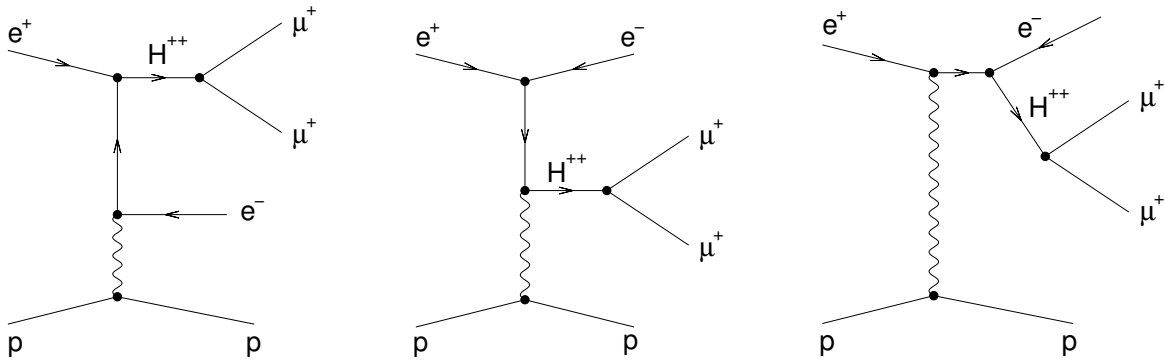bution maybe suppressed by selecting only equally charged muons. Due to the presence of the beam lepton this is not necessarily the case for electron pairs. En vogue are two different models which forecast equally charged lepton pair production: a lepton flavour violating grand unification theory using a SU-15 symmetry [Agr92, Fra92] and supersymmetric left-right models where the $SU(2)_R$ is broken by triplet Higgs fields. Within the SU-15 theory two different production processes may lead to this striking signature in the detector: $e^-p \longrightarrow e^+\mu^-\mu^- X$ [Agr92] or $e^-p \longrightarrow \bar{\nu}_\mu \mu^- \mu^- X$ [Kim01]. Stringent limits have been put on the mass of the heavy dilepton gauge boson $X^{\pm\pm}$ which is exchanged in the latter processes. Masses below 850 GeV are excluded by a muonium to antimuonium conversion experiment [Wil98].

Doubly Charged Higgs

Supersymmetric left-right models (SUSYLR) deserve attention since they solve many theoretical problems: they imply baryon and lepton number conservation, solve the CP problem of the Minimal Supersymmetric Standard Model (MSSM) and implement the see-saw mechanism by giving heavy mass to the right-handed Majorana neutrino [Dut98]. In these theories right or left handed Higgs triplets $H_{R,L} = \left(H^0_{R,L}, H^+_{R,L}, H^{++}_{R,L}\right)$ are introduced, which contain the doubly charged Higgs particle H^{++}. At HERA energies the doubly charged Higgs decays dominantly into lepton pairs. In figure 2.11 the Feynman diagrams for doubly charged Higgs production at HERA are depicted [Acc93, Acc95]. In principle there exist two leptonic decay modes: one which produces two leptons of the same flavour ($H^{++} \longrightarrow \mu\mu$) and one with two leptons of different flavour in the final state ($H^{++} \longrightarrow \mu e$ or $H^{++} \longrightarrow \mu\tau$). The muonium experiment also disfavours the latter decay mode [Wil98]. Limits for the same flavour decay mode stem from Opal, which has excluded doubly charged Higgs with masses below 98.5 GeV at the 95 % confidence level [OPA01]. Discovery potential is left for a doubly charged Higgs with a mass $M_{H^{++}} > 100$ GeV.

2.5   Monte Carlo Simulation

Monte Carlo programs have been established to determine the influence of the detector on the measurement, which is expressed by acceptances and efficiencies. The Monte Carlo generators deliver the four momenta of all particles involved in the physics process. A GEANT [GEA] based detector simulation tracks the generated particles through the H1 detector and simulates the detector and trigger response. Finally the reconstruction software is applied to the Monte Carlo 'raw data'. Detector noise is taken into account using special runs with randomly triggered events.

For an inclusive measurement a number of different processes have to be considered and so many different generators have to be used. There are two different Monte Carlo generators available to simulate the dominant two-photon process, LPAIR and GRAPE. LPAIR is the program which has been used at H1 since a couple of years, while GRAPE is a modern program which simulates all electroweak lepton pair production processes (section 2.1). A short introduction to the programs is given in the following (section 2.5.1). Both programs cover the whole kinematical region. More details on their treatment of the proton representation can be found in section 2.5.2. Generators used to simulate other lepton production mechanisms are introduced in section 2.5.5.

2.5.1   GRAPE and LPAIR

LPAIR

LPAIR [Bar91, Due94] simulates the two-photon process [4]. It factories the cross section into three components: the central subprocess $\sigma(\gamma\gamma \longrightarrow l^- l^+)$, the photon flux from the electron, given by the Weiz"acker-Williams approximation, and the photon flux from the proton. The calculation of the central $\gamma\gamma \longrightarrow l^- l^+$ is based on a formula derived by Vermaseren [Ver83]. In principle arbitrary structure functions are allowed for the beam particles. To derive a complete hadronic final state the program is interfaced to JETSET [Sjo01].

GRAPE

GRAPE-DILEPTON [Abe01, Abe98] is an event generator for non resonant di-lepton production in ep collisions. The di-lepton production via $\gamma\gamma$, $\gamma Z^0, Z^0 Z^0$ or Z^0-production are considered as well as the effect of QED Compton type diagrams in which a radiated photon decays into a lepton pair. The cross section calculation is based on the exact matrix elements in the electroweak theory at tree level. Using the automatic calculation program 'GRACE' [Ish93] the corresponding Feynman amplitudes are calculated and via interfaces to the generators PYTHIA [Sjo01] and SOPHIA [Muc00] a complete hadronic final state is obtained. The resolved Drell-Yan process and Bremsstrahlung from the proton (elastic and quasi-elastic processes) are not included [5]. The

---

[4][Kae00] reports on extensions of LPAIR.

[5]The resolved Drell-Yan process can be simulated with help of the PYTHIA generator (section 2.5.5).
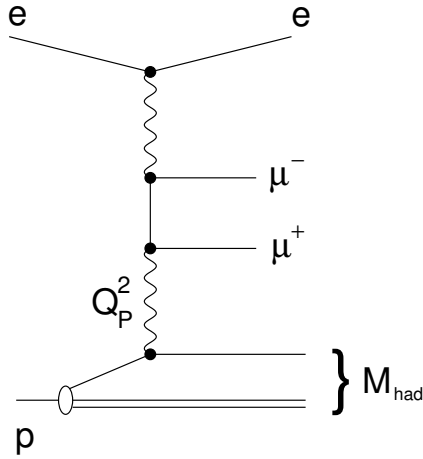
resolved and point-like processes are distinguished using the virtuality u of the intermediate quark. A minimal u-cut of 25 GeV^2 is always applied.

In case of electron pair production the interference effect of the final state electrons is taken into account. Furthermore initial state radiation (ISR) from the electron and final state radiation performed by PYTHIA can be simulated. Initial state radiation corrects for the photon self energy by modifying the photon propagator [Bur95].

2.5.2   Description of the Proton

Both generators, LPAIR as well as GRAPE, distinguish three different production processes according to the description of the proton. Two variables, the invariant mass of the hadronic system

$$M_{had} = \sqrt{(p_e + p_p - p_e - p_{l^+} - p_{l^-})^2} \qquad (2.19)$$

and the negative momentum transfer squared at the proton vertex

$$Q_P^2 = -(p_e - p_e - p_{l^+} - p_{l^-})^2 \qquad (2.20)$$

classify the following categories:

- elastic: $M_{had} = M_P$

- quasi-elastic: $Q_P^2 < Q_{min}^2$ or $M_P + M_{\pi^0} < M_{had} < M_{cut}$

- deep-inelastic (DIS): $Q_P^2 > Q_{min}^2$ and $M_{had} > M_{cut}$.

M_P denotes the proton mass and M_{π^0} the pion mass. The inelastic scattering process $ep \longrightarrow eX\mu\mu$ is divided into a quasi-elastic and a deep-inelastic region, in which different models are used to describe the proton.

Figure 2.13: *Division of the phase space. The Pictures shows the three different processes: elastic scattering (ELA), quasi-elastic (Q-ELA) and deep inelastic scattering (DIS). For the GRAPE the dotted line forms the border between the two different parametrisations of the structure function. At the left side the parametr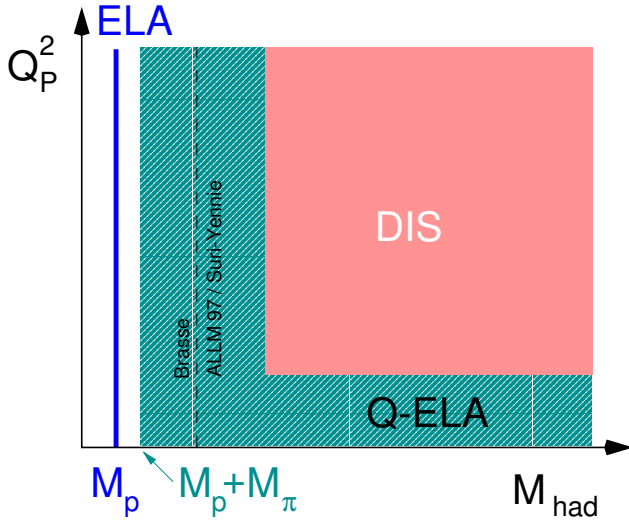isation according to Brasse et al. is used at the right side the ALLM 97 parametrisation is adapted. For LPAIR the Brasse parametrisation is only used up to $Q_p^2 = 5$ GeV^2.*

Division of the Phase Space

Following an advice from [www1] recommended for the GRAPE generation one has to generate four parts separately which are distinguished as introduced in section 2.5.1 by the invariant mass of the hadronic system M_{had} and the negative squared momentum transfer Q_p^2 at the proton side:

- elastic

- quasi-elastic for $M_{had} < 5$ GeV

- quasi-elastic for $M_{had} > 5$ GeV and $Q_p^2 < 1$ GeV^2

- deep-inelastic for $M_{had} > 5$ GeV and $Q_p^2 > 1$ GeV^2 .

The distinction between deep-inelastic scattering and quasi-elastic scattering corresponds to the two different models which are used to describe inelastic scattering: the Quark-Parton-Model (DIS) and the description of the proton by empirical structure functions (quasi-elastic). While the Quark-Parton-Model is not valid at small M_{had}, where nucleon resonances occur, latest parametrisations of the structure function provide a reasonable good description of the proton over almost the complete phase space and therefore principally allow to describe the inelastic part with these parametrisations solely [ALLM].

Elastic Process

The elastic part is a pure QED calculation. To calculate the Feynman amplitude the proton current J^μ, which is proportional to $\bar{u}\Gamma^\mu_{pp\gamma}u$, has to be to determined. In the usual convention $\bar{u}$ and u denote the wave functions of the outgoing and incoming proton. According to the Feynman rules a vertex with a lepton current is simply considered by $\Gamma^\mu = -iQe\gamma^\mu$, where Q is the charge

quantum number and γ^ν denotes a Dirac matrix. If one requires, that J^μ should have the most general form of a parity conserving Lorentz four vector, then the incorporation of the extended proton structure into the factor $\Gamma^\mu_{pp\gamma}$ for the proton vertex leads to:

$$\Gamma^\mu_{pp\gamma} = -ie\left(G_1\gamma^\mu + \frac{\kappa_p}{2M_p}G_2 i\sigma^{\mu\nu}q_\nu\right), \tag{2.21}$$

where κ_p is the anomalous magnetic momentum, the tensor $\sigma^{\mu\nu}$ is the anticommutator of the γ^μ matrices. The two coefficients G_1 and G_2 represent two independent form factors, which are related with the electric and magnetic from factor by the linear combination:

$$G_E = G_1 - \frac{\kappa_p Q_p^2}{4M_p^2}G_2 \tag{2.22}$$

$$G_M = G_1 + \kappa_p G_2. \tag{2.23}$$

Expressing the factor (2.21) with the electric and magnetic form factors G_E and G_M one derives using the Gorden decomposition:

$$\Gamma^\mu_{pp\gamma} = -ie\left(\mu_p G_E\gamma^\mu - \frac{(p_p^\mu(in) + p_p^\mu(out))}{2M_p}\frac{\kappa_p}{1+\tau}G_E\right), \tag{2.24}$$

where the magnetic momentum of the proton is expressed in units of the Bohr magneton μ_B via $\mu_p = (1 + \kappa_p)\mu_B$. Using the expression (2.24) GRAPE calculates the amplitudes of the corresponding feynman diagrams. A relation between the electric and the magnetic form factor is given by the empirical dipole formula, which has been confirmed by many measurements:

$$G_E(Q_p^2) = \frac{G_M(Q_p^2)}{\mu_p} = \frac{1}{(1 + Q_p^2/0.71\text{GeV}^2)^2} \tag{2.25}$$

where μ_p is the magnetic moment of the proton in nuclear magnetons. The predictions from GRAPE and LPAIR agree within the per mill level if the additional GRAPE features (section 2.5.3) are excluded.

Quasi-Elastic Process

In the quasi-elastic region the proton may fluctuate into a resonance state like the Δ-resonance [HM84]. The proton structure in the resonance region has to be described phenomenological. To describe the Δ-resonance (uuu) the form factors have to be redefined:

$$G_E \longrightarrow G_{E,p\Delta} \qquad \text{and} \qquad G_M \longrightarrow G_{M,p\Delta} \tag{2.26}$$

The general case covers all proton resonances and also more complex non resonant transition states of the proton. Substituting the form factors by two-dimensional structure functions $F_E(Q_p^2, M_{had})$ and $F_M(Q_p^2, M_{had})$, the complex proton structure can be parametrised. Suitable are also the linear combinations of the electromagnetic structure functions $F_1(Q_p^2, M_{had})$

Parametrisation	LPAIR	GRAPE
Brasse	$M_{had} < 2.01$ GeV and $Q_p^2 < 5$ GeV^2	$M_{had} < 2.0$ GeV and $Q_p^2 < 100$ GeV^2
Suri-Yennie	$M_{had} \geqslant 2.01$ GeV or $Q_p^2 > 5$ GeV^2	-
ALLM 97	$(M_{had} \geqslant 2.01$ GeV$)$	$M_{had} \geqslant 2.0$ GeV

Table 2.3: *Parametrisations of structure functions used for the LPAIR or GRAPE generation. The phase space division for the use of the structure functions differs slightly for the two generators. Both generators use the parametrisation by Brasse et al. to simulate the resonance region. LPAIR has been equipped with the Suri-Yennie parametrisation of the structure function which is also used for comparison with the data. To allow for further improvements and detailed comparisons on the generator level the GRAPE interface for the ALLM 97 parametrisation has been integrated into LPAIR which allows the use of ALLM 97 for $M_{had} > 2.0$ GeV.*

and $F_2(Q_p^2, M_{had})$. Both generators use two different parametrisations of the electromagnetic structure functions: the proton resonance region ($M_{had} < 2$ GeV) is parametrised by Brasse et al. [Bra76]. For the other part of the phase space LPAIR uses a structure function determined by [SY72], while GRAPE uses the parametrisation by ALLM 97 [ALLM]. The different parametrisations of the structure function, which are implemented in the generators, are listed in table 2.3. To allow further improvements and detailed comparisons on the generator level the GRAPE interface for the ALLM 97 parametrisation has been integrated into LPAIR. Since the full simulation could not be redone for all of the generated files, LPAIR is compared to the data using the Suri-Yennie parametrisation.

To get a clue of the quality of the parametrisation of the structure functions one can compare the Suri-Yennie and the ALLM 97 parametrisation to the predictions derived using the Quark-Parton-Model at the deep inelastic regime. While the ALLM 97 parametrisation is in agreement with the predictions from the Quark-Parton-Model, the Suri-Yennie parametrisation delivers a 30 % lower cross section. For the comparison with the data this difference is irrelevant since structure functions will not be applied in the regime of deep inelastic scattering ($M_{had} > 5$ GeV and $Q_p^2 > 1$ GeV^2). The difference between the two parametrisations of the structure function is caused by the inclusion of the HERA data in the fit procedure for the parametrisation. Since the HERA data enriches the phase space mainly at the deep inelastic regime these differences are expected.

Deep-Inelastic-Scattering Process

Deep Inelastic Scattering can be described within the so called Quark-Parton-Model. The Quark-Parton-Model treats the proton as a stream of free quarks. One of the quarks interacts with the electron while the other quarks, the proton remnant, are not taking part in the scattering process. This simplifies the description of the scattering process. The two structure functions F_1 and F_2 are not anymore two dimensional functions, but depend only on the Bjorken scaling parameter x.
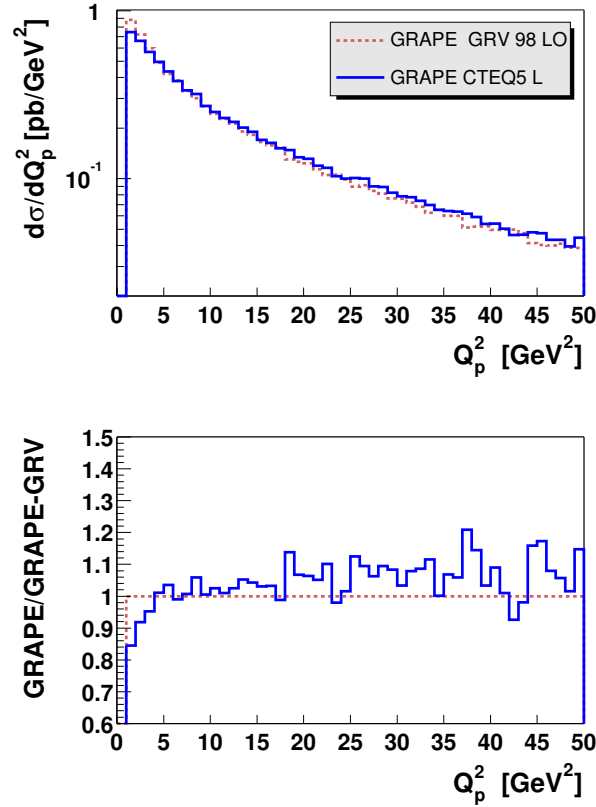
Figure 2.14: *Comparison between GRV 98 and CTEQ5.*

The structure function F_2 is determined by the quark densities $q(x)$ and $\bar{q}(x)$:

$$F_2(x) = \Sigma Q_q^2 \cdot (q(x) + \bar{q}(x)), \qquad (2.27)$$

where Q_q^2 is the charge quantum number of the quark type q. The two structure functions are related to each other by the Callan-Gross relation:

$$F_1(x) = 2xF_2 \qquad (2.28)$$

The x-dependence of the different quark flavours is parametrised by parton density functions. Different parametrisations of the parton density function performed by several groups are collected in the the PDFLIB [Plo93]. Each parametrisations is valid from a minimum Q_{min}^2 onward, which determines the lowest possible Q_p^2 for the generation of the DIS-part. CTEQ5 L [CTEQ] and GRV 98 LO [GRV] are the most recent parametrisation which extends to small Q_p^2 ($Q_{min}^2 = 1$ GeV^2 respectively $Q_{min}^2 = 0.8$ GeV^2). The validity of the Quark-Parton-Model is guaranteed requiring a minimal hadronic mass M_{had} of 5 GeV. The effect of the different parametrisation is quite small. A comparison of the dependency on Q_P^2 between CTEQ5 L and GRV 98 LO shows a difference of roughly 3 % (figure 2.14).

Quark flavour	u	$\bar{u}$	d	$\bar{d}$	s	$\bar{s}$	c	$\bar{c}$
Cross section [pb]	25.2	7.4	4.4	2.1	1.1	1.1	1.3	1.3

Table 2.4: *Contribution of the light quark flavours to the total cross section (GRAPE with $4° < \theta_\mu < 170°$).*

For the generation of the inelastic part the contribution of the different quark flavours has to be taken into account. It is interesting to note their contribution to the total cross section. In table 2.4 the contribution of the light quark flavours u, $\bar{u}$, d, $\bar{d}$,c, $\bar{c}$, s, $\bar{s}$ are listed.

2.5.3   GRAPE vs. LPAIR

Comparison between LPAIR and GRAPE, which have been published earlier, showed that LPAIR and GRAPE in two-photon mode agree well with each other [Abe98, Hof99]. Differences between this two programs are due to the additional GRAPE features:

- radiative effects: initial state and final state radiation;

- additional diagrams: QED-Compton process and electroweak processes.

The effect of these advantageous features can be estimated from the GRAPE generator itself since it allows to deactivate each of these features. For the comparison with the data the full GRAPE description is exploited.

Radiative Effects

The effect of initial state radiation on the total cross section ranges from 2 % for the elastic channel to 10 % for the inelastic channel. Figure 2.15 shows the influence of initial state radiation on the mass spectrum and table 2.5 gives the effect on the total cross section for different phase space regions. Final state radiation is carried out with PYTHIA using the parton shower method, which effects mainly the composition of the hadronic final state. The chosen observables are not sensitive to final state radiation.

Elastic	Quasi-elastic	Inelastic
2.2 %	5.5 %	7.3 %

Table 2.5: *Relative cross section increase due to initial state radiation in different phase space regions.*

Additional Processes

GRAPE contains additional processes which are simulated, QED Compton processes and electroweak processes like $\gamma Z^0 \longrightarrow \mu\mu$ and Z^0-production. The QED Compton processes influence
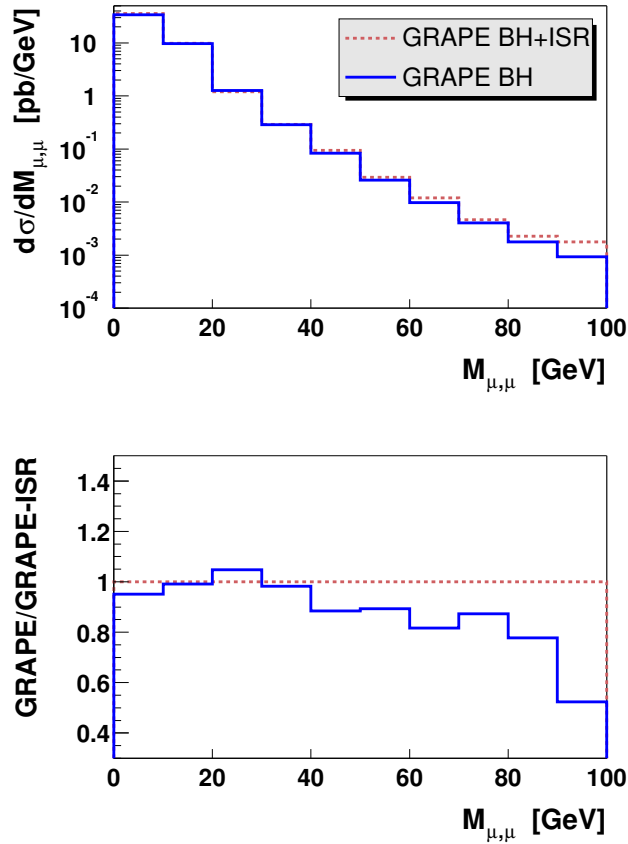
Figure 2.15: *Two-photon process generated with GRAPE with and without initial state radiation.*

the cross section in the low mass region (figure 2.5), while as influence of the electroweak processes only the Z^0-resonance is important. Due to the negative interference of the QED Compton processes with the two-photon process the the total cross section in the analysed phase space lowers about 5 %.

To observe the Z^0-resonance the given luminosity is too small. Within the Standard Model only about 0.2 Z^0 events would be expected in the muon channel. The GRAPE generator does not consider the resolved contribution to Z^0-production. Resolved and point-like Z^0-production are distinguished using a cut on the virtuality u of the incoming quark ($u > 25$ GeV)[6] like in the theoretical calculations of Baur, Vermaseren and Zeppenfeld [Bau92]. They predict the cross section of the omitted resolved part to be 25 % - 30 % of the total cross section of the Z^0-resonance.

---

[6]Meanwhile GRAPE allows also a regularisation of the u-pole using the virtuality of the emitted photon, i.e. a cut on Q_e^2.

Figure 2.16: *Comparison of the lepton masses for the electron and the muon channel. ee and $\mu\mu$ show the invariant mass of the lepton pair, while ee/e assigns the mass of the two leptons with the highest transverse momentum (i.e. including the scattered electron if it has a higher transverse momentum than one of the pair leptons.) Clearly visible is the Z^0-resonance. Due to the presence of the beam lepton the expectation in the electron channel is significantly higher.*

2.5.4 Muons and Electrons

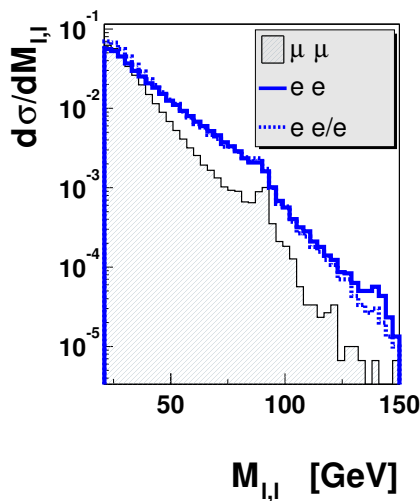It is aimed to compare the results of this analysis with an electron analysis which is being carried out within H1 [Val02]. Therefore it is interesting to compare the expectation of the two different lepton types with each other. The comparison is carried out for the high invariant mass region, since in the electron analysis $P_t^{l1} > 10$ GeV for the first lepton and $P_t^{l2} > 5$ GeV for the second lepton are required. In the electron analysis it is not possible to identify the electron pair due to the presence of the scattered electron. If three electrons are found within the detector the mass of the two with the highest transverse momentum $M_{1,2}$ is calculated.

In figure 2.16 the Monte Carlo expectation for this mass $M_{1,2}$, the invariant masses of the electron pair $M_{e^+e^-}$ and the invariant mass of the muon pair $M_{\mu^+\mu^-}$ are compared to each other. The masses determined in the electron channel are very similar, while the expectation of the invariant mass in the muon channel is much lower. In the last bin from 100 GeV to 150 GeV the cross section of electron pair production is about four times higher than for muon pair production. The consistency of the masses determined in the electron channel proofs that the 'interferference' due to the beam electron is correctly considered in the Monte Carlo Simulation. A di-lepton mass which includes the beam electron in the muon channel should give roughly the same contribution as the $M_{1,2}$ in the electron channel. At small masses differences are expected due to the Cabbibo-Parisi effect which enhances the cross section in the electron channel (section 2.1.2). Table 2.6 summarises the resulting total cross section for a slightly extended polar angle range and the harsher requirements of the muon transverse momenta mentioned above. The main difference between muons and electrons is caused by the interference with the scattered electron [7] [8].

---

[7]An electron analysis where this problem is addressed can be find in [Hof00].

[8]Rare processes may cause a non negligible contribution due to this effect, for instant estimations of the resolved Drell-Yan process with PYTHIA predict an increase of the electron pair cross section by at least 10 %, though this process contributes to muon pair production only at the per mille level.

Process	Electrons	Muons
Two-photon	1.11 pb	1.11 pb
Two-photon (with Interference)	1.54 pb	—
QED	1.60 pb	1.15 pb
Electroweak	1.61 pb	1.16 pb

Table 2.6: *Comparison of the expectation derived from GRAPE for electrons and muons ($10° < \theta_{lepton} < 160°$, $P_t^{l1} > 10$ GeV and $P_t^{l2} > 5$ GeV). 'Two-photon (with Interference)' considers the interference effect in the electron channel, 'QED' includes the Bremsstrahlungs processes and 'Electroweak' considers also Z^0-production. The prediction for the muonic channel is about 30 % lower than the one for electrons.*

2.5.5 Other Monte Carlo Programs

DIFFVM

To simulate the Υ production the generator DIFFVM [Lis93] is used. This generator simulates diffractive vector meson production in ep scattering using the Vector Meson Dominance Model (VDM) [Fra98].

AROMA

The AROMA Monte Carlo program [Ing97] simulates the production of heavy quarks in boson-gluon fusion. Charm ($c\bar{c}$) and beauty ($b\bar{b}$) production with a subsequent semileptonic decay of one of the produced quarks result in single muons in the final state which are normally close to a jet. In case both of the produced quarks decay semileptonically also two muons may be produced which may fake a lepton pair. By the number of equally charged leptons these contribution can be checked if the charge measurement is reliable.

The cross section prediction derived by AROMA for beauty production is known to be to low. H1 measured [H199] a cross section which was 4.6 times higher in Photoproduction and 4.3 times higher in DIS than predicted. Measurements by other experiments confirm the H1 results. Since the Photoproduction regime is dominating, the AROMA prediction will be corrected by 4.6.

EPVEC

The event generator EPVEC [Bau92], is used to simulated heavy boson decays. The generator is interfaced to PYTHIA to perform the generation of the hadronic final state. EPVEC is mainly used to simulate W-production, because Z-production can also be carried out by GRAPE (section 5). New next to leading order calculations [Die02] predict a correction of 10 % - 15 % to the cross section predicted by EPVEC.

PYTHIA

The event generator PYTHIA [Sjo01] allows the simulation of a large variety of processes. It can be used instead of AROMA for beauty or charm production, for the simulation of processes in the Photoproduction regime and also for W-production. The simulation of W-production with PYTHIA is useful though it is based on some older calculations than the one of EPVEC. The main difference to EPVEC is that some minor contributing diagrams are missing. But an advantage is the possibility to include initial and final state radiation.

PYTHIA is also able to generate lepton pairs. Using the matrix element $f_j f_K \longrightarrow \gamma/Z$, where $f_{j,k}$ represents a fermion, the resolved Drell-Yan process can be simulated.

COMPHEP

The simulation of the doubly charged Higgs signal relies on a Monte Carlo program using the COMPHEP package [Puk99] to evaluate the lowest order squared amplitudes of the corresponding Feynman diagrams. The differential cross sections are integrated with the VEGAS package [Lep80].

The H1 Detector at HERA

3.1 HERA

The 'Hadron Elektron Ring Anlage' (HERA) situated to the west of the city of Hamburg consists of two storage rings, one for positrons or electrons with an energy of 27.5 GeV and one for protons with an energy of 920 GeV. Collisions at a centre of mass energy of roughly 320 GeV take place at two interactions points, one in the south where the 'Zeus-detector' [Zeu93] is located and another one in the north, where 'H1' [H197a, H197b] is placed. Until 1998 the centre of mass energy was 300 GeV due to a lower proton beam energy of 820 GeV.

The HERA rings have a circumference of 6.3 km and are located approximately 30 m below ground level. Up to 220 particle bunches each separated by 96 ns circulate. A small number of the bunches are non-colliding and provide the experiments with background studies. With 10^{10} - 10^{11} particles per bunch beam currents of 50 mA (for the electron beam) and 110 mA (for the proton beam) are achieved.

3.2 The H1 Detector

The H1 detector, shown in figure 3.1, measures approximately 12 m × 10 m × 15 m and weighs roughly 2800 tonnes. To allow the study of a wide range of ep physics processes it was designed as a 4π detector with almost hermetic coverage and an asymmetric design to allow for the different beam energies. It is constructed as a typical universal detector for a collider experiment with tracking chambers enclosing the interaction point. For an impulse and charge measurement the tracking detectors are situated in a strong magnetic field of 1.15 T. Calorimeters surrounding the tracking detectors absorb almost all of the energy of incident particles. This core of the detector is surrounded by a superconducting coil which provides the magnetic field for the track measurement. The iron yoke returning the magnetic flux is interlayered with muon chambers which form the 'Central Muon Detector'. Descriptions in this section will be almost entirely restricted to the detector systems which are essential to this analysis.

HERA Experiment H1
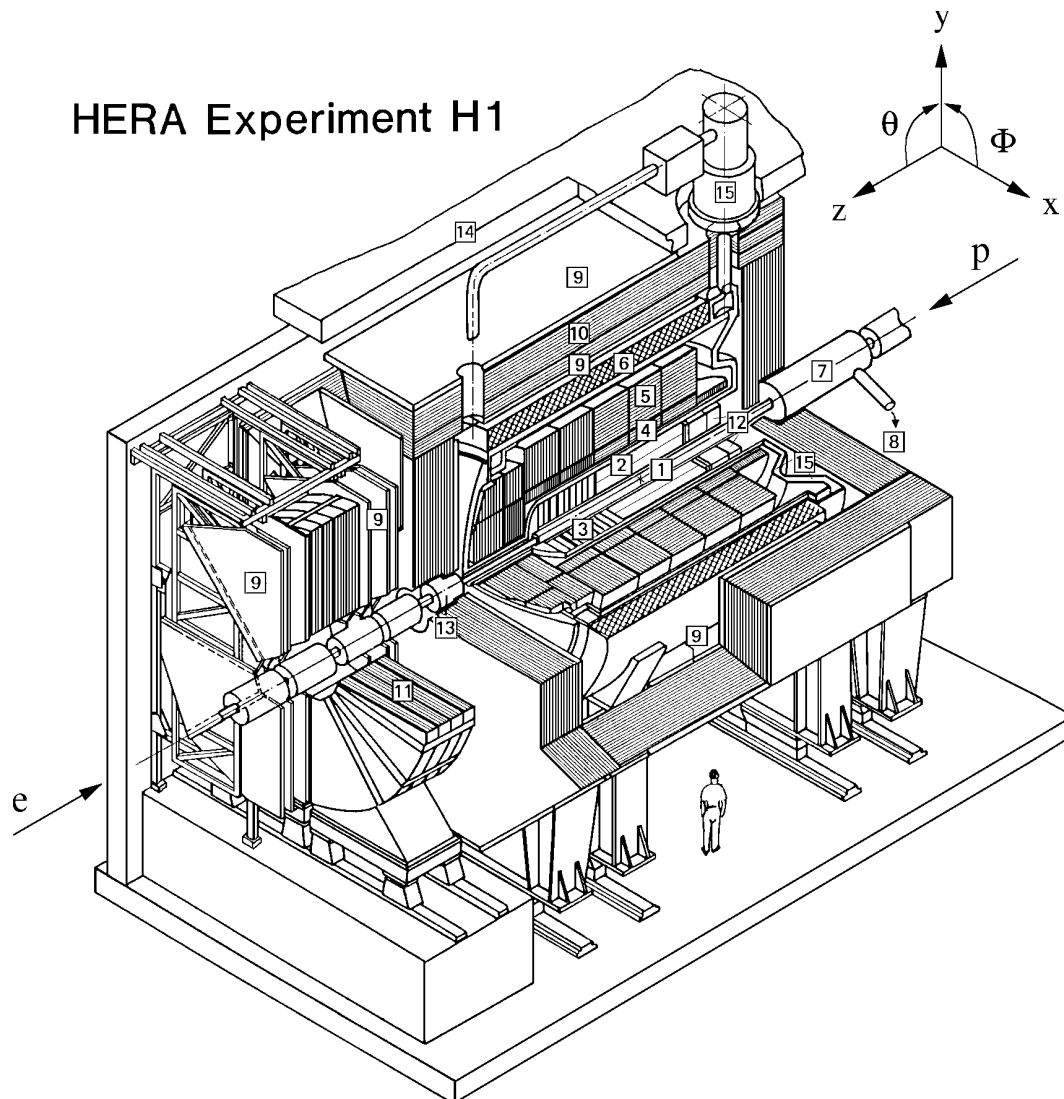
1	Beam pipe and magnets	9	Muon chambers
2	Central tracking detectors	10	Instrumented Iron yoke
3	Forward tracking detectors	11	Forward muon toroid
4	Electromagnetic LAr calorimeter	12	SpaCal and BDC
5	Hadronic LAr calorimeter	13	PLUG calorimeter
6	Super-conducting coil	14	Concrete shielding
7	Compensating magnet	15	LAr cryostat
8	Liquid Helium supply		

Figure 3.1: *3d view of the H1 detector.*

3.2.1 The Coordinate System

Points within the detector are defined using the Cartesian coordinates (x,y,z) with respect to the origin, taken to be the nominal interaction point. The z-axis follows the proton beam direction through the detector. The y direction is vertically upwards, while x points horizontally to the centre of the storage rings. Angles are described with a spherical coordinate system (r,θ,ϕ), such that the polar angle $\theta = 0°$ is along the +z-axis and the azimuthal angle ϕ is an angle in the x-y plane. The 'forward' region refers to the region of low θ.

3.2.2 Luminosity

The luminosity system is essential for accurate cross section measurements. The luminosity is calculated using the Bethe-Heitler process (ep $\rightarrow$ epγ), for which the cross section is precisely known from QED. This process is measured with special detectors situated in the backward direction: the Electron Tagger at $z = -33.4$ m adjacent to the electron beam pipe and the Photon detector at $z = -102.9$ m adjacent to the proton beam pipe. The measured luminosities yield a precision of better than 2 %.

3.2.3 Calorimetry

The H1 detector contains four separate calorimetric units with different angular acceptances. They are the Liquid Argon Calorimeter (LAr), the Spaghetti Calorimeter (SpaCal), the Tail Catcher and the Plug Calorimeter. Important for this analysis are the Liquid Argon and the Spaghetti Calorimeter, which serve the energy measurement of the hadronic final state.

The Liquid Argon Calorimeter

The Liquid Argon Calorimeter has a particle detection acceptance over the range of $4° < \theta < 154°$ and consist of two sections, both contained in a single liquid argon cryostat: the inner layer which detects electromagnetic (EM) showering and the outer which detects hadronic (HAD) showering.

The Liquid Argon Calorimeter is an example of a non-compensating calorimeter. Non compensating means that its response to electrons and hadrons is not equal: hadrons on average deposit ≈ 30 % less energy than electrons of the same initial energy. This reflects the energy lost by hadrons due to nuclear excitations or breakup in the absorber material. Compensation in the Liquid Argon Calorimeter is achieved through software weighting techniques. After calibration, carried out using test beam and cross checked in-situ, the calorimeter has been found to have an energy resolution of $\frac{\sigma_{EM}(E)}{E} \approx \frac{0.15}{\sqrt{E}} \oplus 0.01$ for electrons and $\frac{\sigma_{HAD}(E)}{E} \approx \frac{0.15}{\sqrt{E}} \oplus 0.01$ for charged pions. The absolute energy scale is known to between 0.7 % and 3 % for the electromagnetic and 2 % for the hadronic part.
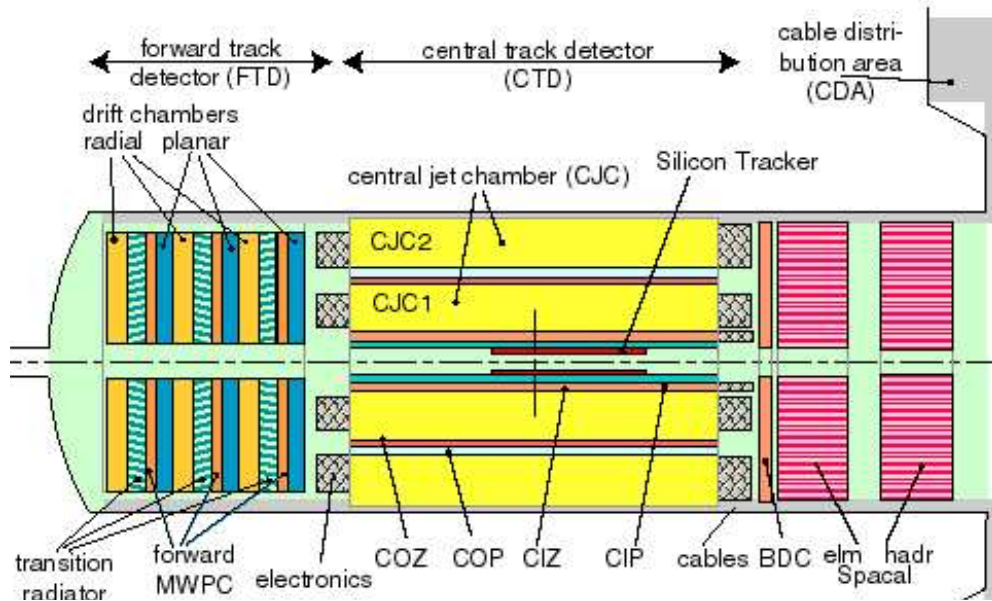
Figure 3.2: *Cross section through the Inner Tracker. The Inner Tracker is about 4 m long and extends radially about 1 m.*

The Spaghetti Calorimeter

The Spaghetti Calorimeter (SpaCal) is a cylindrical detector which sits in the x-y plane in the backward region of the detector, approximately 1.5 m behind the interaction point. It extends over the polar range $153° < \theta < 178°$ and has both electromagnetic and hadronic components. The electromagnetic section of this calorimeter has an energy resolution of $\frac{\sigma_{EM}(E)}{E} \approx \frac{0.08}{\sqrt{E}} \oplus 0.01$ and the hadronic part has an energy resolution of $\frac{\sigma_{EM}(E)}{E} \approx \frac{0.30}{\sqrt{E}} \oplus 0.07$.

3.2.4   Tracking

The tracking detectors in H1 are a combination of drift chambers, multi wire proportional chambers and silicon trackers. They divide themselves into an 'Inner Tracker' (figure 3.2), built up by the 'Forward' and the 'Central Tracker', and the two muon detectors, the 'Forward Muon Detector' and the 'Central Muon Detector', forming the outer part. Other tracking detectors, which are mainly located in the backward region, are not used in this analysis.

Central Tracker

The Central Tracker, covering an angular range of $20° < \theta < 160°$, consist of four drift chambers, which are the central jet chambers CJC 1 and CJC 2 and the inner and outer Z Chambers CIZ and COZ, and of two multi wire proportional chambers, called the inner and outer proportional chambers CIP and COP.
 The most important information for the track reconstruction of the Central Tracker is derived
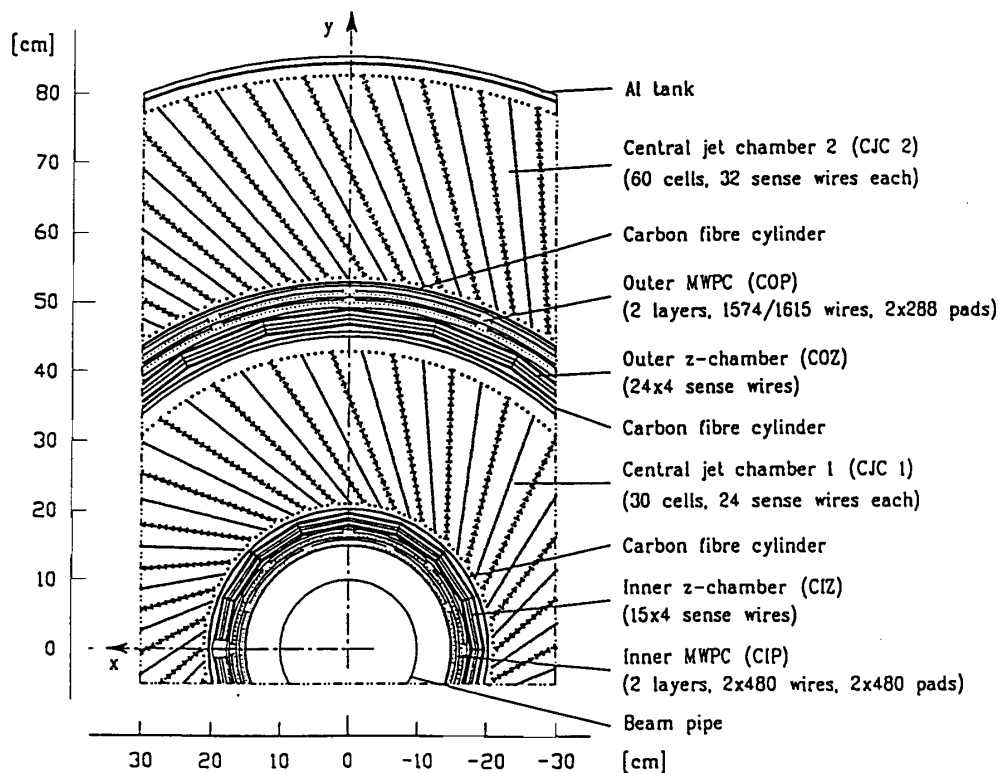
Figure 3.3: *Central Tracker. R-z view.*

from the Central Jet Chambers, CJC 1 and CJC 2. These chambers have planes of sense anode wires running in parallel to the beam axis, forming cells which are tilted by approximately $30°$ with respect to the radial direction to improve the resolution and to avoid track ambiguities. The spatial resolution of the CJC in the $r\phi$ plane is $\sigma_{r\phi} = 170 \ \mu$m and the momentum resolution is $\frac{\sigma_{Pt}}{p_t^2} = \frac{0.01}{\text{GeV}}$. For the measurement of the z-coordinate charge division techniques achieves a resolution of $\sigma_z = 22$ mm.

The measurement of the z-coordinate is improved with the Z chambers CIZ and COZ which consist of rings of sense wires strung perpendicular to the beam axis. This orientation of the wires (reversed w.r.t CJC 1and CJC2) allows a resolution of $\sigma_z = 300 \ \mu$m to be obtained.

The Central Proportional Chambers, CIP and COP, serve the fast triggering (section 4.4). They are equipped with pad cathodes which are segmented in z and ϕ: 60×8 for the inner chamber and 18×16 for the outer chamber. Since 1997 H1 is also equipped with a Central Silicon Tracker, 'CST', which was still being tested and not fully integrated into the event reconstruction while the analysis was performed.

Forward Tracker

The Forward Tracker covers the polar angular range $5° < \theta < 30°$. It is made up of three 'super-modules', each containing a planar wire drift chamber, a forward multi-wire proportional chamber, a transition radiator (designed for the separation of electrons and pions) and a radial wire drift chamber. The super-modules are positioned around the z-axis with the wires strung perpendicular to the z-axis in the planar chamber. The planar chambers are rotated by $60°$ with respect to each other to enable resolution of hodoscope ambiguities. The primary purpose of the forward multi wire proportional chambers and the two multi wire proportional chambers of the Central Tracker is to provide space points for the z-vertex trigger.

Central Muon Detector

The Central Muon Detector (CMD) is the outermost hermetic detector of H1, enclosing the inner part like a barrel. It is divided geometrically into 4 sectors, the two endcaps and the forward and backward barrel (figure 3.4). Each of them is divided into 16 modules numbered from 0 to 63, which differ greatly in size depending on their location.

Each module (figure 3.5) is built up by 10 layers of streamer tubes, which are incorporated in the iron return yoke for the flux of the superconducting magnet. Therefore this largest and heaviest of the sub-detectors is also referred to as the 'instrumented iron'. To either side of the iron yoke three additionally layers may be fixed which are contained in aluminium boxes, the so called inner and outer muon boxes. These muon boxes improve the track measurement and cover the edges of the detector. The resolution of the position measurement perpendicular to the streamer tubes varies from 3 to 4 mm. To measure the coordinate along the wires contained in the streamer tubes five of the layers are equipped with strip electrodes, which achieve a resolution of 10 mm to 15 mm. Some of the layers have additionally 'pad electrodes' which allow the measurement of the deposited energy. This 'Tail Catcher' calorimeter may be used to detect the energy leaking from the inner calorimeters. The other function of the pad electrodes is to improve the track reconstruction.

In total 103.000 wires are contained in the Central Muon Detector, which extends in polar angular of $5°$ to $175°$. In the barrel region the wires are oriented along the z-axis allowing a good ϕ measurement and an impulse resolution of roughly 30 %. In the endcaps the wire orientation is along the x-axis. The different wire orientation in the barrel and in the endcaps results in reconstruction problems for tracks reaching from the endcaps to the barrel or vice versa. Resulting track segments in the two parts of the detector are not linked to each other. From the 10 layers within the iron the inner first three layers and the layers 8 and 12 serve as trigger layers.

Forward Muon Detector

The Forward Muon Detector is located outside the main detector, covering a polar angular range of $3° < \theta < 17°$. It consist of six double layers of drift chambers, three either side of a toroidal
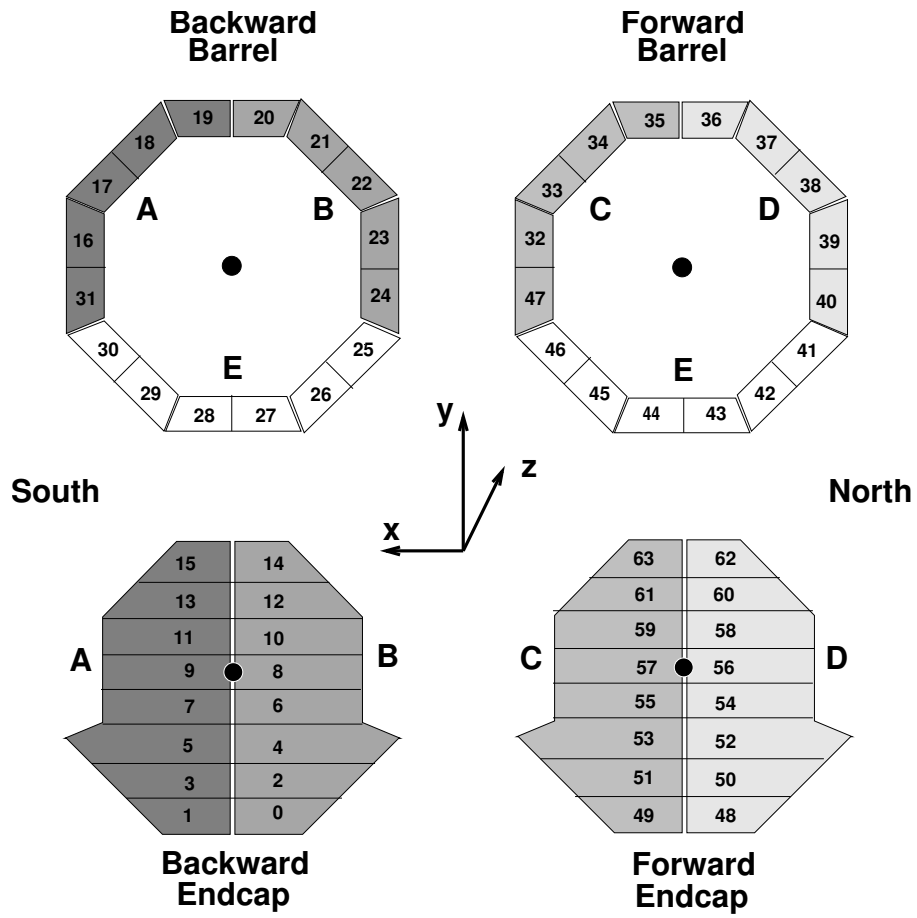
Figure 3.4: *Layout of the 64 modules of the Central Muon Detector.*
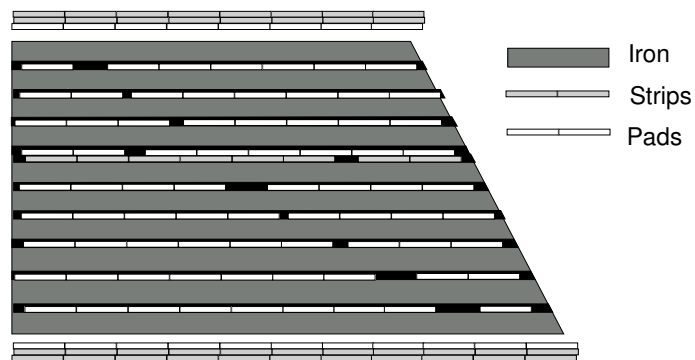
Figure 3.5: *A module of the Central Muon Detector.*
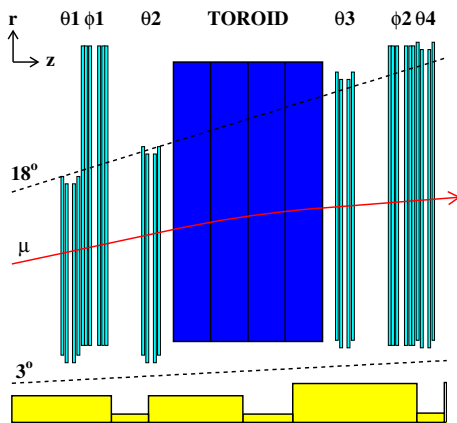
Figure 3.6: *Schematic view of the Forward Muon Detector. The drift chambers are labelled $\theta1 - \theta4$ and $\phi1 - \phi2$.*

magnet providing a magnetic field of 1.5 T. Due to energy losses in the inner detectors and in the toroid, muons having an impulse $p > 5$ GeV may be identified with this detector. Four of the six layers have their sense wires strung tangential to the beam pipe to measure most accurately in θ and two layers have their sense wires strung azimuthally, to measure accurately in ϕ. Each drift cell, 120 mm wide and 20 mm deep, contains one sense wire in the middle.

3.2.5   Forward Detectors

The forward detectors allow to detect parts of a dissolved proton. In addition to the forward part of the Liquid Argon Calorimeter and the pretoroid layers of the Forward Muon Detector a Proton Remnant Tagger is installed at $z = +24$ m in the forward direction inside the HERA tunnel. It consists of seven scintillators arranged around the beam pipe and covers a polar angle range of $0.06° < \theta < 0.3°$.

3.2.6   Time of Flight Counters

The Time of Flight (ToF) systems are effective means of rejecting events which arrive 'out-of-time', generally from beam induced processes. They consist of plastic scintillators, which are located within the detector near the beam pipe in three places. Another double layer of scintillators called the 'Veto-Wall', which rejects events caused by the proton beam halo, is positioned in the backward direction behind the iron return yoke. Their timing measurement is accurate to 1 ns.

Trigger

The H1 trigger system comprises 5 different trigger levels. Level 1, 'L1', and Level 2, 'L2', are online hardware triggers. In addition the events have to pass an online software trigger, L4, the fourth level of the H1 trigger system. The installation of the third level is foreseen for future data taking periods. The fifth level, an off-line event classification, was only used until 1998. An exact knowledge of the trigger efficiency is crucial, because it directly enters the cross section measurement. The first trigger level is described in section 4.1. Its efficiency has the greatest influence on this analysis. Part of the L1 forms the trigger of the Central Muon Detector. It is reviewed in detail in section 4.2, before the function of the other contributing triggers (sections 4.4, 4.5 and 4.6) is described. The resulting efficiency for the trigger level 1 is presented in section 4.7. Then the second (section 4.8) and fourth (section 4.9) trigger level are explained.

4.1 Trigger Level 1

The level 1 trigger consists of about 192 'trigger elements' derived from the different sub-detectors. These trigger elements form 128 'subtriggers', which can cause the start of the detector readout.

4.1.1 Prescales

Depending on run and background conditions the L1 subtriggers are prescaled. A subtrigger prescaled with a factor d accepts only every d-th event fulfilling the trigger condition of this subtrigger. By weighting the data events with a factor

$$w_j = \frac{\sum_{k=1}^{Nruns} \mathcal{L}_k}{\sum_{k=1}^{Nruns} \mathcal{L}_k P_{jk}}$$

the effect of the prescaling is taken into consideration [Egl97]. $\mathcal{L}_k$ is the integrated luminosity of run k. The probability P_{jk} that at least one of the N_{Subtr} subtriggers has triggered the event is

given by

$$P_{jk} = 1 - \prod_{i=1}^{N_{Subtr}} \left(1 - \frac{r_{ij}}{d_{ik}} \right),$$

with

$$r_{ij} = \begin{cases} 1 & \text{if raw subtrigger is set in event j} \\ 0 & \text{otherwise} \end{cases}$$

$$d_{ik} = \text{ prescaling factor of subtrigger } i \text{ in run } k.$$

The weight w_j is calculated as a luminosity weighted factor over a larger period with unchanged trigger definitions to achieve small statistical errors.

4.1.2 Choice of Subtriggers

Muons in the H1-detector are identified by linking inner tracks to tracks in the muon detector. Subtriggers configured on this topology form the basis of a muon analysis. The following subtriggers are used in the analysis:

- **s18**: Muon Outer Endcaps
  A signal in the outer endcaps of the Central Muon Detector is combined with low track multiplicities.
  (Mu_ECQ & DCRPh_Ta & DCRPh_THig & zVtx_Cls)

- **s19**: Central Muon Trigger
  Central muons are triggered at high track multiplicities.
  (Mu_Bar & DCRPh_CNH & zVtx_sig_1)

- **s22**: Muon Outer Endcaps
  In contrast to s18 this trigger selects muon events with high track multiplicities.
  (Mu_ECQ & DCRPh_CNH & zVtx_sig_1)

- **s34**: Central Muon Trigger
  This trigger is used for muon events with low track multiplicities.
  (Mu_Bar & DCRPh_Ta & DCRPh_TNeg & DCRPh_THig & (zVtx_small‖zVtx_cls))

- **s56**: Muon and Electron Trigger
  A signal in one of the muon detectors is combined with a signal in the SpaCal, which is optimized for electron triggering.
  (Mu_Any & DCRPh_Ta & (SPCLe_IET > 1‖SPCLe_IET_Cen_2))

On the second trigger level special physics finders may be used as additional triggers on top of certain subtriggers (section 4.8). These subtriggers are not included in the analysis. The prescale factors are also considered in the choice of trigger. Subtriggers with high prescales are excluded. The chosen subtriggers are at most prescaled by 15.0 % (section 4.1). Of particular interest

	99e$^-$	99e$^+$	00
s18	1.15	1.11	1.13
s19	1.02	1.00	1.02
s22	1.01	1.00	1.01
s34	1.02	1.03	1.01
s56	1.01	1.00	1.00

Table 4.1: *Average prescale factors for different run periods for trigger phases 2-4.*

sector	module
BIEC	6−11
BOEC	0−5, 12−15
BAR	16−47
FEC	54−59
FOEC	48−53, 60−63

Table 4.2: *Relation between modules and trigger sectors.*

to this analysis is the region of high P_t^X, the region where the vectorial sum of the transverse momentum of the hadronic final state is large. To ensure a high trigger efficiency in this region a special set of 'NC/CC' trigger is used, which saves a couple of events in addition [Hei98]. The behaviour of these triggers is well known from various publications and needs no further investigation here. Different data taking runs are divided into four run phases with different conditions. Typically for phase 1 are very high prescales. Since these phase covers only a small part of the luminosity the analysis is restricted to the phases 2-4 in which the prescales for the subtriggers are usually small.

4.2   Muon Trigger

The function of the muon trigger will be described in as much detail as is appropriate for the presented analysis. A detailed description of the hardware can be found in [Itt98], and further information is given in [Olz00]. The muon trigger delivers eight 'trigger elements' to the central trigger. These trigger elements are combined with trigger elements of other sub-detectors into 'subtriggers' which can cause the readout of an event. The muon trigger elements are built up from trigger signals of the 64 modules of the Central Muon Detector. A trigger signal may derive from any module. The modules are divided into five trigger sectors according to their position within the detector: the 'Forward Inner Endcap' (FIEC), the 'Forward Outer Endcap' (FOEC), the 'Barrel' (Bar), the 'Backward Outer Endcap' (BIEC) the 'Backward Inner Endcap' (BIEC). The disjunction of the trigger signals of the modules within one of these sectors form one trigger element. The remaining three are the trigger elements 'Mu_2_FIoOEC', which requires at least two trigger signals of the modules in the forward inner or outer endcap , 'Mu_2_BIoOEC', which requires at least two trigger signals of the modules in the backward outer or inner endcap, and Mu_3_Bar, which requires three trigger signals in the barrel [1]. In table 4.2 the relation between the modules and the trigger sectors is listed. The trigger elements of the Central Muon Detector are shown in table 4.3 together with the appropriate sector, a H1-internal number which is assigned to each trigger element and the name for the trigger element.

---

[1]For ep physics Mu_3_bar is useless - it is intended as cosmic trigger. Formerly, until 1998, this last trigger element was defined as a two muon trigger which could have been very useful for this analysis.

Sector	Nb.	Name	Definition
BIEC	56	Mu_BIEC	$n_{BIEC} > 0$
BOEC	57	Mu_BOEC	$n_{BOEC} > 0$
BEC	58	Mu_2_BIoOEC	$n_{BIEC} > 1$ or $n_{BOEC} > 1$
BAR	59	Mu_BAR	$n_{BAR} > 0$
BAR	60	Mu_3_BAR	$n_{BAR} > 2$
FIEC	61	Mu_FIEC	$n_{FIEC} > 0$
FOEC	62	Mu_FOEC	$n_{FOEC} > 0$
FEC	63	Mu_2_FIoOEC	$n_{FIEC} > 1$ or $n_{FOEC} > 1$

Table 4.3: *Definition of the eight muon trigger elements. The sectors are defined by the geometry of the Central Muon Detector. The Barrel (Bar) is distinguished from the Endcaps (EC). Both Endcaps, the Forward and Backward Endcap (FEC and BEC), are divided into 'inner' and 'outer' part (FIEC, FOEC and BIEC, BOEC). The definition gives the minimum number of trigger signals which must have occurred within the given sectors.*

4.2.1 Layer Coincidences

The trigger signal of each module is build up by a 'layer coincidence' and a 't_0-signal'. In the endcaps 5 out of the 16 wire layers are used as trigger layers, while in the barrel only 4 layers are used. A layer coincidence is given by a minimum number of trigger layers which have been hit within two neighbouring bunch crossings [2]. The exact numbers of layers which is required differs between the trigger sectors (table 4.4). Generally three layers are required in the endcaps while in the barrel only two layers are sufficient due to the smaller amount of background . The 't_0-signal' is determined by the earliest hit of the layer coincidence.

BEC		3 out of $3, 4, 5, 8, 12$
BEC	module 8, 9	3 out of $3, 4, 5$ 1 out of$, 8, 12$
BAR		2 out of $3, 4, 5, 8$
BAR	module 33 (Run > 251082)	3 out of $3, 4, 5, 12$
FOEC		3 out of $3, 4, 5, 8, 12$
FIEC		4 out of $3, 4, 5, 8, 12$

Table 4.4: *Definition of layer coincidences.*

---

[2]The technical realisation is beyond the scope of this document. It is achieved by evolved shifting techniques described in [Itt98].

4.3 Efficiency of the Muon Trigger

The Monte Carlo simulation is used to evaluate the trigger efficiency in regions of low statistic. Using the Monte Carlo simulation one has to model the timing. For the Central Muon Detector this is done by down scaling the identified layer coincidences with a modulewise trigger efficiency. This results in a correct description of the trigger for the bunch crossing 0. Other bunch crossings, which are of course not relevant for the readout of the detector, are not described.

There are two ways to determine this modulewise efficiency, either using special cosmic runs (section 4.3.1), or using ep data (section 4.3.2). The advantage of the cosmic-method is the availability of high statistics, while the luminosity-method is more close to the final analysed data. When using the Monte Carlo simulation to determine the trigger efficiency it has to be ensured that the simulation agrees with the data. This can be achieved by checking each of the used trigger elements or a combination of the trigger elements which are entering the final subtriggers (section 4.3.3). Finally a systematic error for the trigger efficiency must be derived. Either the difference between data and Monte Carlo or the difference between the cosmic-method and the luminosity-method can be used (section 4.3.4) .

4.3.1 Efficiency Determination with Cosmic Data

The particles contained in cosmic radiation, so called 'cosmics', offer a rich source for efficiency determinations and studies of the detector performance. The intensity of this radiation is proportional to the cosine of the angle of incidence, and sufficient statistics are not available in all regions of the muon detector, so that for the modules of the inner endcaps special beam halo runs are used instead. The determination of the trigger efficiency with cosmic data is complex and more details can be found in [Olz00]. It is Important to understand the trigger efficiency as a product of a timing efficiency and a verification efficiency:

$$\epsilon_{trigger} = \epsilon_{timing} \cdot \epsilon_{verification}.$$

The outline of this section is as follows:
first the verification efficiency is explained, then the timing efficiency is introduced. To understand the timing of the Central Muon Detector first an overview over the different timing factors is given. Following this is the explanation of the measurement of the relative timing distribution, from which an efficiency can be derived after normalisation. The final result is achieved by the combination of the verification and timing efficiency.

Verification Efficiency

The verification efficiency takes hardware failures into consideration. For a normally working module it should be 1. Negligible inefficiencies could also arise from the verification of layer coincidences using wrong or out of date information on the quality of the wires. In the event of a wire being noisy or switched off, this should be described with the help of the BOS bank IQWS
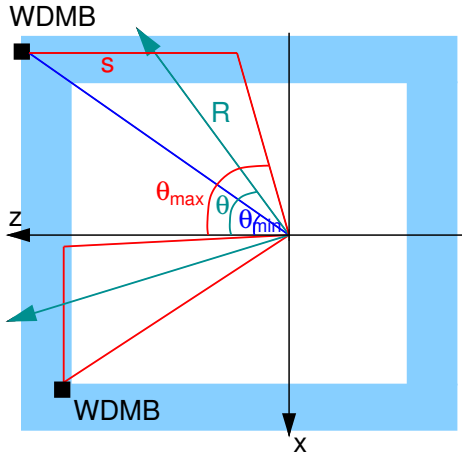
Figure 4.1: *Relation between time of flight and signal time. S denotes the length the signal has to travel to reach the electronics (WDMB)of the Central Muon Detector (shaded).*

(Iron Quality Wire and Strips) [Blo87]. The trigger simulation uses this bank to verify possible layer coincidences. Layers which are known to be dead in the 'readout' or in the 'trigger' [3] are not taken into account for layer coincidences.

Timing Efficiency - Overview

The timing efficiency depends on a variety of factors. The time t_{det} a particle coming from the interaction point in the middle of the detector needs to be detected as a trigger signal is the sum of the time of flight t_{flight} from the interaction point to the module, the drift time t_{drift} of the electrons in the streamer tubes and the signal time t_{signal} which is given by the time needed for the signal propagation along the wires in the muon chambers :

$$t_{det} = t_{flight} + t_{drift} + t_{signal}.$$

The time of flight can be calculated from the distance R of the hit in the trigger layers to the nominal interaction point:

$$t_{flight} = \frac{R}{c}.$$

Since the first electronic readout components are attached to the outer part of the wires in the muon chambers, the signal time and time of flight are not independent of each other: large times of flight correlate with small signal times and vice versa. Consulting figure 4.1 the relation between the sum of the time of flight and the signal time to the maximal time of flight may be derived:

$$\frac{t_{flight} + t_{signal}}{t_{flight,max}} = \frac{1}{c} \frac{\sin \vartheta_m}{\sin \vartheta} + \frac{1}{v_{signal}} (\cos \vartheta_m - \sin \vartheta_m \cot \vartheta).$$

---

[3]It should be mentioned that layers might be dead in the trigger, but still be 'alive' in the readout. This can happen in the event of a noisy wire, which would lead to high trigger rates. Since it is only possible to switch off a 'whole element', about 8 wires, the decision might be taken to leave the element active for the readout, but take it out of the trigger.

The velocity v_{signal} of the signal propagation in the wires is about 20 cm/ns. θ_m denotes the maximum polar angle in the forward part of the detector and the minimum polar angle in the backward region. The sum of the time of flight and the signal time ranges between 15 ns and 35 ns [ltt98]. Due to the enormous size of the muon detector the cable length of the various modules differ greatly. The possibility of adjustments is limited. The trigger and readout of the Central Muon Detector have common phases and only an adjustment in steps of whole bunch crossings (96 ns) could be applied for a single module. For the determination of the modulewise efficiency with cosmic and beam halo data, an additional correction time t_{cor} has to be taken into consideration.

Due to the different flight direction of comics in the upper half of the detector the correction time is given by

$$t_{cor} = 2 \cdot t_{flight}.$$

In the lower half of the detector the timing of the cosmics is similar to the one of ep physics events and thus the correction time is zero. For beam halos passing the detector from the backward to the forward direction the following correction time has to be applied:

$$t_{cor} = t_{flight} - \frac{z}{c},$$

where z is the z-coordinate of the hit at the trigger layers.

Timing Efficiency - Measurement of the Relative Timing Distribution

To derive the timing efficiency one measures the the timing distribution $t_{0,rel}$ of the trigger signals relative to the event t_0 which is registered by the inner tracker or in the case of beam halos by the Forward Muon Detector. To avoid ambiguities only events with exactly two measured muons are accepted. Furthermore a trigger verification from the readout is required. To express the relative timing distribution

$$t_{0,rel} = max(t_{C,TGPP}, t_{0,TGPP}) - t_{TGPP} - t_0 + t_{cor}$$

in terms of a formula, deeper technical knowledge of the triggering system is required:

- t_{cor} is the correction time explained above.

- t_{TGPP} is a fixed delay which has been adjusted so that the muon trigger coincides with the central trigger.

- t_0 is the event t_0 measured by the inner tracker or the Forward Muon Detector

- $t_{0,TGPP}$ gives the position of the t_0-signal from the Central Muon Detector in a certain 'TGPP'-pipeline.

- $t_{C,TGPP}$ gives the position of the layer coincidence signal from the Central Muon Detector in a certain 'TGPP'-pipeline.

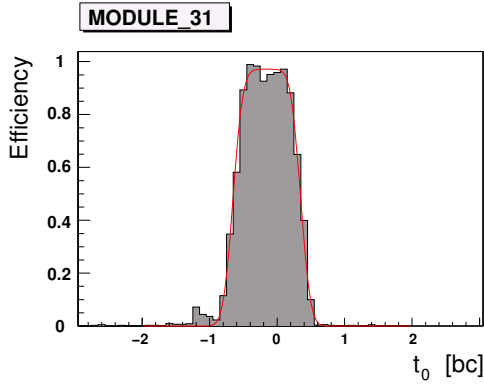- $max(t_{C,TGPP}, t_{0,TGPP}) - t_{TGPP}$ assigns basically the bunch crossing to the trigger signal.

MODULE_31

Figure 4.2: *Normalised $t_{0,rel}$ distribution.*

Timing Efficiency - Normalising the Relative Timing Distribution

To normalise the relative timing distribution a probability $p(t_{0,rel})$ is derived which gives the probability that the trigger fires in the corresponding bunch crossing for each time $t_{0,rel}$. Ideally this would result in a squared distribution with the height one centred around $t_{0,rel} = 0$.

An example of such a normalised distribution for module 33 is shown in 4.2. The distribution is fitted with a rectangular function which is at both sides modified by an error function. The x-axis shows the time in units of bunch crossings.

Timing Efficiency - Result

The timing efficiency ϵ_{timing} is evaluated by fitting the normalised timing distribution $t_{0,rel}$ with a squared distribution $\hat{\epsilon}_{timing}$ which is modified by two error functions Erfc:

$$\hat{\epsilon}_{timing} = \frac{1}{4} \cdot p_0 \cdot \text{Erfc}\left(\frac{t_{0,rel} - \hat{t}_N - 0.5}{\sigma_N}\right) \cdot \text{Erfc}\left(\frac{t_{0,rel} - \hat{t}_N - 0.5}{\sigma_N}\right).$$

The amplitude p_0, the width σ_N and the average delay $\hat{t}_N$ are the free parameters of the fit. The fit value at $t_{0,rel} = 0$ gives the resulting efficiency for this module:

$$\epsilon_{timing} = \hat{\epsilon}_{timing}(t_{0,rel} = 0).$$

Figure 4.3 comprises the values of the timing efficiency of all modules. A χ^2 value depicted as shaded histogram is minimal for good fits.

Trigger Efficiency from Special Runs

The total trigger efficiency results from the combination of the verification and the timing efficiency. The great advantage of the cosmic method is the availability of very high statistics, which leads to a small statistical error. A disadvantage is that cosmic runs are not taken very often, and therefore reflect the status of the detector only for a short time. Only if the timing is
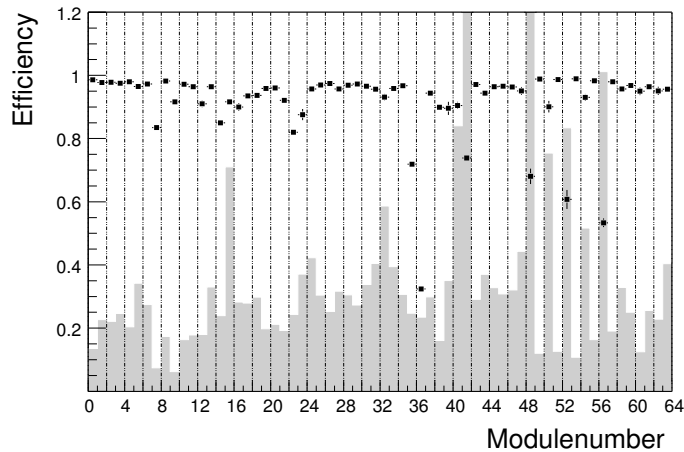
Figure 4.3: *Timing Efficiency for all modules. The shaded histogram shows the χ^2 of the fit used to determine the efficiency. For some modules mainly located in the forward outer endcap the χ^2 is large and the result of the fit thus not reliable.*

carefully monitored and many cosmic runs are taken this will result in a reliable efficiency. In the case of timing shifts the cosmic runs may also be weighted with the luminosity which has been registered between the different cosmic runs. Since in the last run periods the timing was stable there was no need to weight the cosmic runs accordingly.

4.3.2 Efficiency from ep Data

The ep data stored on 'data summary tapes' (DST's), which forms the bases for data analysis, also offers the possibility of determining a modulewise trigger efficiency. A distinction between timing and verification efficiency as in the case of cosmic data will not be made. After discussing the basic principles for the efficiency determination, which are also described in [Kru01], improvements are introduced which can be realised using reprocessed H1 data.

Basic Method

For the determination of the modulewise efficiency a 'single muon selection' is used. All events having exactly one 'linked' muon and no further tracks in the Central Muon Detector are selected. A linked muon is defined by a track in the Central Muon Detector which is successfully linked to an inner track measured by the Central or Forward Tracker. The restriction to single muons is done to avoid ambiguities. In the event of two muons in the barrel the identification of the module that fired is impossible. Harsh cosmic cuts are essential. Cosmics have a different timing behaviour to physics events in the upper detector half. There are two types of cosmics which should be distinguished here: 'overlaying events', a physics event with an additional cosmic muon, and simple measured cosmic events. For all selected events an independent 'monitor trigger' is required. Subtriggers not containing a trigger element of the Central Muon Detector are used. In addition a trigger verification from the readout is necessary. A trigger is verified
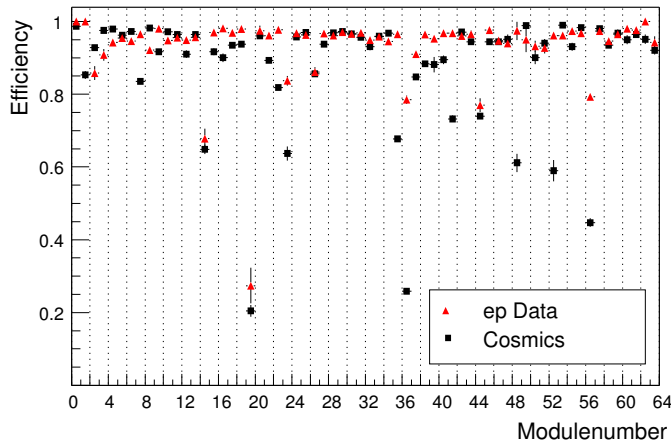
Figure 4.4: *Efficiency from cosmic runs compared to the efficiency derived from ep data.*

if a layer coincidence could be identified. Since this method uses data stored on 'DST', the trigger verification differs from the one used for the cosmic method. On 'DST-level' the readout is merged from all 4 bunch crossing which are stored as raw data. Since the bunch crossing -1,0,1,2 cannot be distinguished anymore, a real 'coincidence' cannot be identified. Simply the layer condition requiring a certain number of trigger layers which must have 'fired' is sufficient. For a barrel module a hit at layer 3 and a hit at layer 5 verifies a trigger signal. This simplification has negligible influences. In principle it could happen that hits in the bunch crossings -1 and 2 for instance could be misidentified as trigger signal. Having selected single muon events with an independent monitor trigger and a verified trigger the efficiency for each module is determined by dividing the number of events having a trigger signal by this total number:

$$\epsilon = \frac{\text{Events with trigger signal in bc 0}}{\text{All events}}.$$

The problems of this method are the low statistics, the trigger verification and the correct determination of the module number. As the module number is not directly accessible from 'DST-data' it has to be recalculated from the measured values. This could lead to some errors if the tracks in the Central Muon Detector cross the border of a module. For the calculation the coordinates of the first hit, ϕ and θ are used. 'Module-crossing' is also the reason why the trigger verification from the readout becomes a problem. Muon tracks extending over two modules fake trigger signals especially in the endcaps .

Improvements

To overcome the problems of the determination of the module number, the output of the iron trigger simulation has been written as BOS bank 'DISM' to the 'DST'. This bank contains six words of 32 bit length which contain the verified triggers for the Central Muon Detector for the bunch crossings -1, 0 and 1 for each module. The bunch crossing 2 is neglected. For the
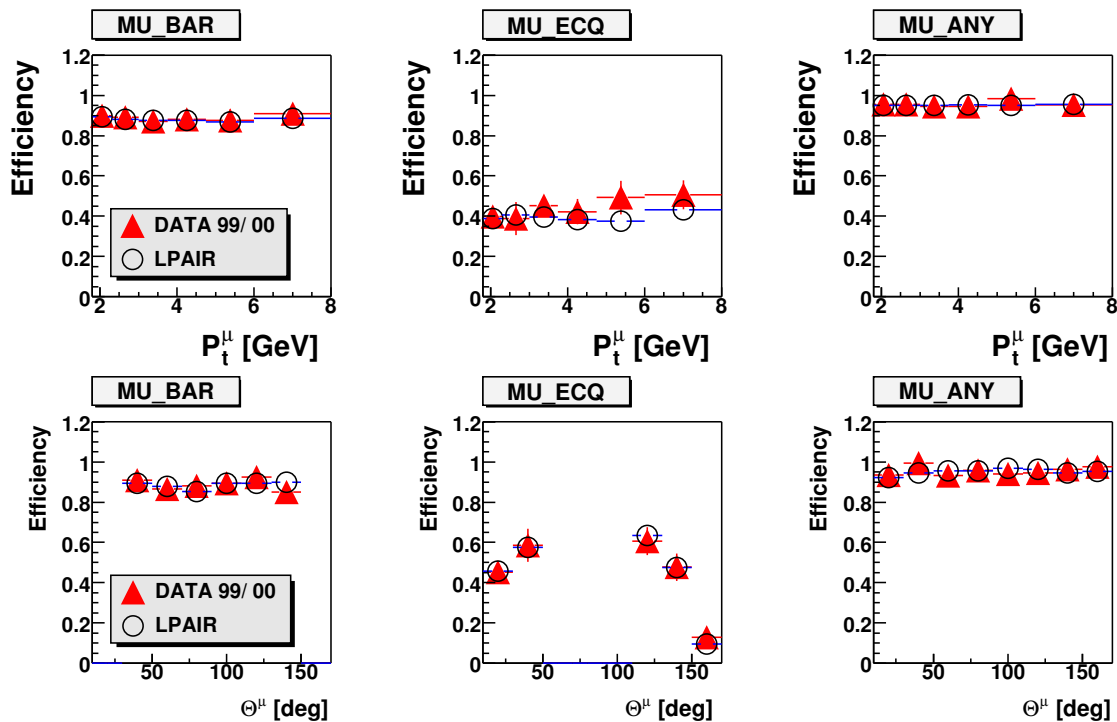
Figure 4.5: *Efficiency of muon trigger elements w.r.t. transverse momentum and θ.*

verification of the trigger signals 'raw data information' distinguishing the 4 bunch crossings in the readout is used. The derived module number is the correct module number. Using this information migrations from one trigger sector to another could be avoided. Fake trigger signals from 'module-crossers' can be completely excluded. From raw data the effect of fake signal ranges up to 8 %. Since there is no track reconstruction from the endcaps to the barrel, the neighbouring modules of the the outermost endcap modules show the highest effect. In the barrel region the effect of fake signals is negligible. Timing shifts over more than two bunch crossing occurred in the readout at the per mille level. For module two the effect was found to be 0.7 %. The trigger simulation also offers the possibility of enlarging the statistics. This is possible by also accepting 'multi-muon events' which might either have a second linked muon, or additional tracks in the Central Muon Detector. Of course there may not be more than one track in one trigger sector. It is important to have higher statistics, because for the run periods with small luminosity (like 1998) the statistics are too low to evaluate a reliable efficiency.

4.3.3 Comparison with the Monte Carlo

The efficiency of the trigger elements must be checked. The agreement of the data and the Monte Carlo and possible dependencies on the relevant kinematic variables has to be investigated. The muon barrel trigger (Mu_Bar) and the 'combined trigger elements' Mu_ECQ, which is a disjunction

| Mu_Any | Mu_BIEC \|\| Mu_BOEC \|\| Mu_Bar \|\| Mu_FIEC \|\| Mu_FOEC |
| Mu_ECQ | Mu_BOEC \|\| Mu_2_BIoOEC \|\| Mu_FOEC |

Table 4.5: *Combined muon trigger elements.*

of trigger signals from the endcaps, and Mu_Any, which is a disjunction of trigger signals from the endcaps and the barrel (see tables 4.5 and 4.1), are relevant to this analysis. The muon barrel trigger (Mu_Bar) and the 'combined trigger elements' Mu_ECQ and Mu_Any are relevant to this analysis. Mu_ECQ is a disjunction of trigger signals from the endcaps and Mu_Any is a disjunction of trigger signals from the endcaps and the barrel (see tables 4.5 and 4.1). Since the combined trigger elements enter the final subtrigger elements these will be used to verify the agreement of data and Monte Carlo. The study of the trigger elements is done with a selection slightly modified in comparison to the data analysis. In figure 4.5 the efficiency as function of the polar angle θ and the transverse momentum determined in ep data is compared to the efficiency simulated with the LPair Monte Carlo.

4.3.4   Systematic Error

After having verified the agreement of the data with the Monte Carlo simulation, the systematic error must still be determined. One way is to use the difference between data and Monte Carlo to estimate a systematic error, another method is to compare the cosmic-method with the luminosity-method and determine the systematic error from that difference. The trigger element of the muon barrel is the most important trigger element for the present analysis and therefore deserves special attention.

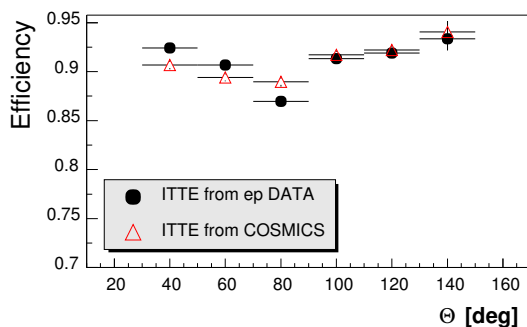**Error from the Comparison of Cosmic and Luminosity Method**

Figure 4.6: *Comparison of efficiency of the trigger element Mu_Bar for a modulewise efficiency 'ITTE' derived from cosmic data with one derived from the luminosity-method.*

For a di-muon sample the differences between the two methods which are compared to each other in figure 4.6 are tiny. An error determined by the average difference weighted with the

	Efficiency	Error
MU_BAR	89.7 %	2.2 %
MU_ECQ	53.2 %	1.7 %
MU_ANY	95.2 %	2.9 %

Table 4.6: *Efficiency of the muon trigger determined with ep data.*

	Efficiency	Error
DCRPH_Ta	92.9 %	2.4 %
DCRPH_Tneg	80.6 %	3.0 %
DCRPH_Thig	92.3 %	1.9 %
DCRPH_CNH	86.0 %	3.9 %

Table 4.7: *Efficiency of the DCRPHI trigger determined with ep data.*

number of events in each bin evaluates to 1.3 %. The excellent agreement of the two completely independent methods are reasoned not only by the stability of the muon barrel trigger, but also by the choice of a di-muon sample for the comparison. The comparison of the modulewise efficiency shows some discrepancies between the two methods. Due to fit problems in the cosmic method these discrepancies are expected. These problems would have to be avoided in a one-muon sample.

Error from the Comparison of Data and Monte Carlo

An error for the efficiency of a specific trigger element can also be determined by the comparison of data and Monte Carlo. The error is determined from the difference between the efficiencies determined in data and Monte Carlo in each bin. The final error results from the average of these differences weighted with the number of events in each bin. Using the efficiency distributed over θ the error for the efficiency of the muon barrel trigger element evaluates to 2.2 %, which is in good agreement with the error determined by the comparison of the two different methods for the determination of the modulewise efficiency.

Nb.	Name	Definition
16	DCRPh_T0	at least one validated t0 mask fired
17	DCRPh_Ta	at least one mask fired
18	DCRPh_Tb	at least b (=2) masks fired, (b programmable)
19	DCRPh_Tc	at least c (=3) masks fired, (c prog.)
20	DCRPh_TPos	at least x (=1) positive masks, (x prog.)
21	DCRPh_TNeg	at least x (=1) negative masks, (x prog.)
22	DCRPh_THig	at least x (=1) pt > 800 MeV masks, (x prog.)
23	DCRPh_TLow	at least x (=1) $400 < p_t < 800$ MeV, (x prog.)

Table 4.8: *Definition of DCRPHI trigger elements. The chosen subtriggers contain the elements 17,19,22,21.*

4.4 DCRPHI-Trigger

The DCRPHI-Trigger is based on information from the Central Tracker. 10 layers of the jet chambers, seven from the CJC 1 and three from the CJC 2, are compared with a predefined mask to count tracks of certain topologies. Low momentum tracks ($450 < p_t < 800$ MeV), high momentum tracks ($p_t > 800$ MeV) or positively or negatively charged tracks are triggered. The trigger elements which the DCRPHI-Trigger delivers to the central trigger are listed in table 4.8. The combined trigger element DCRPH_CNH, which is often used, requires that the elements 19,21,22 have fired. The efficiencies of the DCRPHI trigger elements entering the analysis are shown in figure 4.7. The efficiency is plotted against the number of good central tracks measured in the event. The data and MC simulation are in good agreement. Remaining discrepancies enter the systematic error. The largest differences to the simulation are observed at small track multiplicities for the trigger element DCRPH_CNH, which is designed for high track multiplicities. In table 4.7 the resulting efficiency for the DCRPH trigger elements are listed together with the corresponding error. The error is determined as in the case of the muon trigger from the discrepancies between data and Monte Carlo.
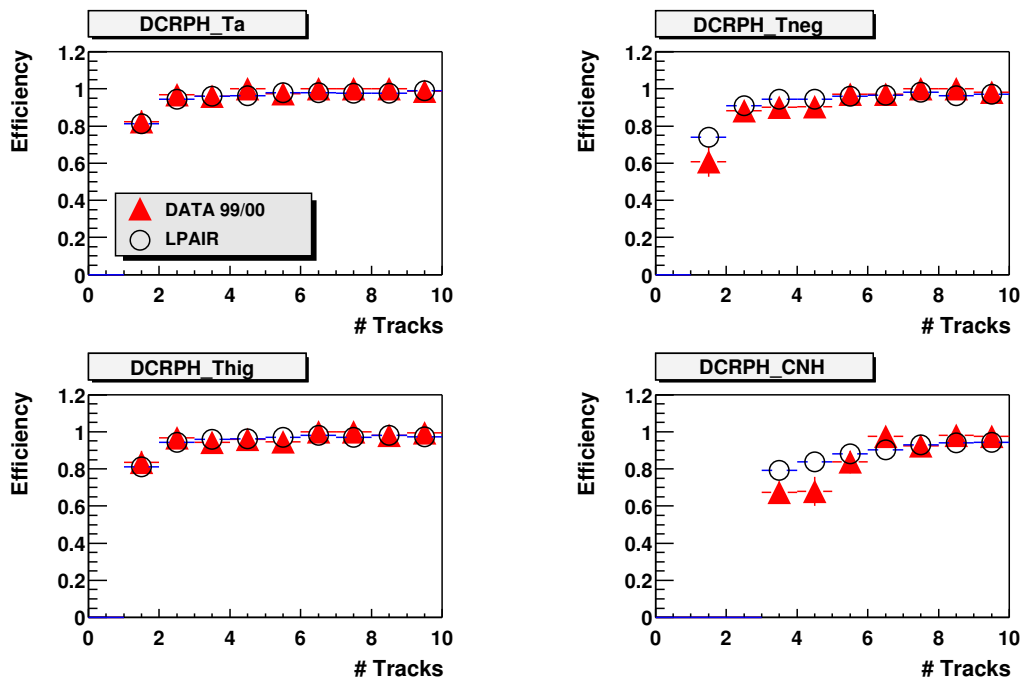

Figure 4.7: *Efficiency of the DCRPHI-trigger elements.*

Nb.	Name	Definition
24	zVtx_T0	at least one ray
25	zVtx_T0_nextbc	at least one ray in next BC
26	zVtx_mul	number of entries in zVtx histogram (bit coded)
27	zVtx_mul	number of entries in zVtx histogram (bit coded)
28	zVtx_mul	number of entries in zVtx histogram (bit coded)
29	zVtx_cls	all hist. entries within 4 neighbouring bins
30	zVtx_sig	histogram peak significance (bit coded)
31	zVtx_sig	histogram peak significance (bit coded)

Table 4.9: *Definition of the zVtx trigger elements. The trigger elements 26-28 and 30-31 contain bit coded information about the 'z-vertex-histogram'.*

4.5 ZVtx-Trigger

To roughly determine the position of the z-Vertex (zVtx) a trigger is built up from the information of the central and forward trackers proportional chambers. From straight line fits in the rz plane a 'z-vertex-histogram' with 16 bins ranging from -44 cm to 44 cm is fitted. Trigger elements are built up requiring a significant peak or a certain number of entries in this histogram. Table 4.9 shows the trigger elements of the zVtx-Trigger. Some of them contain bit coded information on the 'z-vertex-histogram' . The number of entries in the histogram is described by the trigger elements 26-28 which are referred to as zVtx_mul. The peak significance, zVtx_sig, is given by the elements 30 and 31. From these trigger elements combined trigger elements are derived. ZVtx_small for example requires that either none of the trigger elements 26-28 has fired (in bit coding this would be the value 0) or that trigger element 26 and 27 have fired, but 28 has not fired (this would be represented by the value 3). From zVtx_sig the combined trigger element zVtx_sig_1 is derived demanding that either one of the trigger elements 30 or 31 have fired. The efficiencies of the zVtx trigger elements relevant to this analysis are shown in figure 4.8. For all three trigger elements a good agreement with the Monte Carlo simulation is achieved. From the remaining differences between data and Monte Carlo an error for each trigger element is evaluated (table 4.10).

	Efficiency	Error
zVtx_sig	48.4 %	4.0 %
zVtx_T0	92.8 %	0.9 %
zVtx_small || zVtx_cls	87.6 %	3.7 %

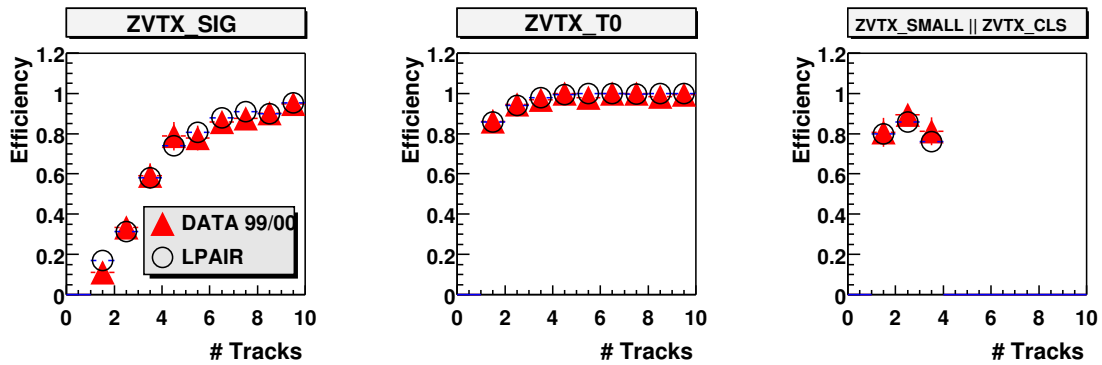**Table 4.10:** *Efficiency of the zVtx trigger elements.*

Figure 4.8: *Efficiency for zVtx trigger elements.*

4.6 SpaCal-Trigger

From the Spaghetti-Calorimeter a trigger is built up by summing up energies for two different cases: for ep physics (ToF) and for upstream background (AToF). The two cases can be distinguished by their arrival time. The physics triggers are used as 'inclusive electron triggers' (IET). By comparing the energy in the trigger towers of 16 electromagnetic SpaCal cells to three adjustable thresholds, trigger elements are formed in an inner ($R < 16$ cm) and an outer ($R > 16$ cm)region of the SpaCal. The disjunction of the trigger elements SPCLe_IET> 1 and SPCLe_IET_Cen_2 enters the subtrigger s56 and is therefore relevant to the analysis. The non-physics trigger is used as veto for non ep background. The SpaCal trigger is designed as an electron trigger. It will therefore be used when an electron is identified. Figure 4.9 compares the efficiency derived from data to the one determined in the Monte Carlo - both agree well within statistical errors. After averaging over all bins a total efficiency of 94 % is found and an systematical error of 3.6 % is estimated.
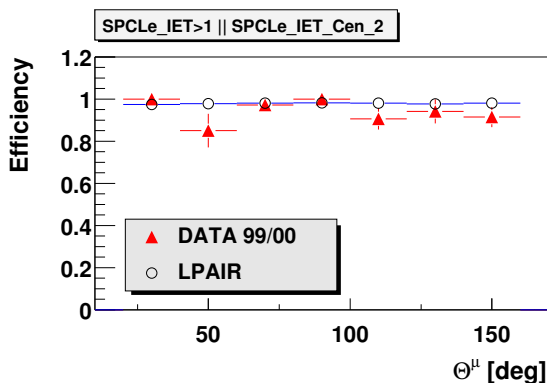

Figure 4.9: *Efficiency for the disjunction of the SpaCal trigger elements SPCLe_IET> 1 and SP-CLe_IET_Cen_2.*
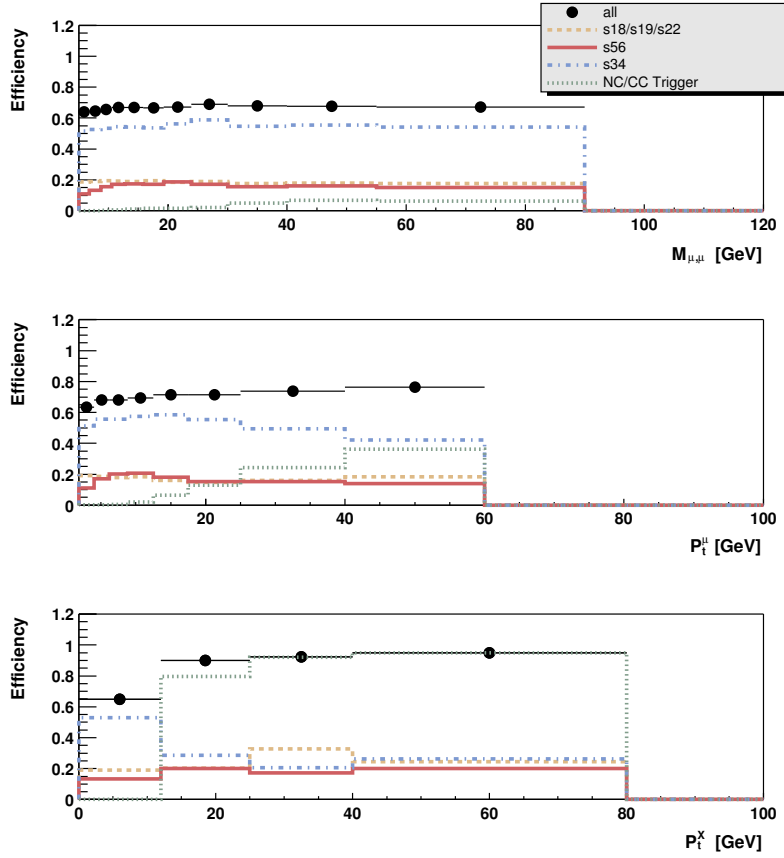
Figure 4.10: *Trigger efficiency for the combined subtriggers as a function of the invariant mass, the transverse momentum and the hadronic transverse momentum. The main contributing triggers are shown separately: s34, the other muon subtrigger (s18,s19,s22), s56 and the NC/CC triggers.*

4.7 Efficiency of the Trigger Level 1

The efficiency of the combination of the used subtriggers is derived from the Monte Carlo simulation. It is typically 70 % , but approaches 100 % for phase space regions with hadrons of high transverse momentum. The efficiency of the combined subtriggers is shown in figure 4.10 as function of the invariant mass, the transverse momentum and the hadronic transverse momentum (P_t^X). The different subtriggers are also compared with each other. Subtrigger s34 has mostly the largest contribution. Its efficiency decreases with P_t^X because the z-Vertex trigger element which is contained in this subtrigger is focused on low track multiplicities. This leads to a loss of efficiency at high P_t^{μ} and at high P_t^X.

Subtrigger	Error
s18	5 %
s19	6 %
s22	6 %
s34	5 %
s56	5 %

Table 4.11: *Systematic error of the used subtriggers.*

The subtriggers s18,s19 and s22 are shown combined. They are optimised for higher track multiplicities or for the endcaps and therefore contribute only to a smaller amount to the full sample. Subtrigger s56, which combines SpaCal and Muon trigger elements, has a similar contribution, though its efficiency decreases significantly towards lower masses or lower transverse momenta. The NC/CC triggers are highly efficient at high P_t^X and compensate the inefficiency of s34 in this region. This behaviour is also visible as a function of the transverse momentum of the muons. The systematic error of the subtriggers is derived from the quadratic sum of the error of the trigger elements which built the subtrigger. The total error of the trigger efficiency is derived by propagating the errors through the Monte Carlo simulation. The resulting error is 6 %.

4.8   Trigger Level 2

The second trigger level is used to reduce the rate of certain subtriggers. Topological correlations (L2TT) or neural networks (L2NN) are used to form up to 32 trigger elements for dedicated physics. Due to the longer time which is available to these triggers more complex decisions may be used to decrease the trigger rate to about 50 Hz. An example of a subtrigger which has to be verified by the decision of a neural net is s15. The trigger decision of the Central Muon Detector, the zVtx-trigger and the DCRPHI-trigger has to be confirmed by a net looking for inelastic J/Ψ candidates. Typically a background reduction of 80 % and an efficiency of 90 % is achieved. Since no subtriggers are chosen which need a L2 verification, this trigger level has no influence on this analysis.

4.9   Trigger Level 4

The fourth trigger level is a multi-processor farm which reduces the trigger rate to 10 Hz. The reduction of the rate is achieved by down scaling events which have not been found by 'hard scale finders' or do not match special final state conditions. Due to the decision of the finders the events are assigned to 16 different classes. Class 8 and 10 contain high-Q^2 physics and class 16 J/Ψ candidates. Isolated muons are almost completely contained in these classes. The efficiency of the fourth trigger level has been checked with methods described in [Moh00]. No inefficiencies have been found.

Selection

Muon candidates at hard scales are selected by requiring either a track link between the central trackers and the Central Muon Detector or an identified minimal ionising particle in the liquid argon calorimeter. To suppress backgrounds and reduce measurement uncertainties additional cuts are imposed. These criteria and their efficiencies are described in this chapter. To be able to handle the large amount of data a 'preselection' (section 5.1) is performed which is the base for the further analysis. To achieve a well defined event sample with correctly determined luminosity a run (section 5.2) and trigger selection is performed, which is explained in detail in chapter 4. Thereafter the muon identification and the track selection are investigated (section 5.3). Finally the multi muon selection is introduced (section 5.4).

5.1   Preselection

A preselection is performed from the large amount of data which H1 has collected. Events with either one muon candidate with high transverse momentum $P_t > 5$ GeV or with one muon pair with an high invariant mass $M_{\mu\mu} > 5$ GeV are selected. The analysis aims at the investigation of effects at high scales and consequently excludes the large muon contribution of J/Ψ decays. For the selection of tracks and the identification of muons standard H1-software packages are adapted to fit high energetic muons. During the time when the analysis was carried out, a major reprocessing of the H1 data from 1996 - 2000 has been initiated. Optimised calibration functions ameliorate the measurement precision. Lots of work has been done to improve the calibration of the inner trackers. The reconstruction program was changed to include the information of the central silicon tracker into the track fitting. The information on dead and noisy wires for the Central Muon Detector was updated. The analysis is based on data reconstructed with this reprocessing.

5.2 Run Selection

The data taking at HERA is divided into 'luminosity fills' which are defined by one filling of the proton and electron bunches into the HERA ring. Each luminosity fill is subdivided into several runs which generally last one or two hours. The detector conditions within a run are stable, but they may differ for different runs or luminosity fills.

To ensure a well understood detector response only runs are selected in which all essential subsystem for this analysis are operational. These are the luminosity system, the Central Muon Detector (CMD), the Central Jet Chambers (CJC 1 and CJC 2), the Central Proportional Chambers (CIP and COP), the Forward Proportional Chambers (FPC), the Liquid Argon Calorimeter (LAR) and the Time of Flight System (ToF).

The analysis is restricted to the data recorded in the years 1999-2000, in which HERA was running at a proton energy of 920 GeV. After a detector upgrade in 1998 in which the proton energy was increased from 820 to 920 GeV, HERA switched from positron-proton scattering to electron-proton scattering. The higher beam induced backgrounds caused several problems especially in the tracking detectors and resulted only in a small amount of luminosity. Also there were severe problems with the muon trigger in the forward endcap. Hence the data taking period of 1998 is omitted. From time to time H1 records runs with special trigger settings, the so called 'minimum bias runs', which are not considered for this analysis. In order to avoid data taking periods where the used subtriggers had high prescale factors, trigger phase 1 is excluded from the analysis.

5.2.1 Luminosity Determination

The calculation of the correct luminosity (section 3.2.2) is an important task for all cross section measurements. The final luminosity value is derived from the total recorded luminosity considering all necessary corrections whose impact can be derived from table 5.1. After restrictions to the run quality and the used trigger phases a correction for the functionality of the subsystems (HV correction) and for satellite bunches (zVtx correction) lead to an integrated luminosity of 70.9 pb^{-1}.

		1999 e$^-$	1999 e$^+$	2000 e$^+$
$\mathcal{L}$	total raw	15.73	19.27	59.62
$\mathcal{L}$	good and medium runs	14.81	18.28	56.78
$\mathcal{L}$	Phase 2-4	12.21	15.21	52.35
$\mathcal{L}$	HV corrected	10.43	14.40	49.52
$\mathcal{L}$	zVtx corrected	10.13	13.54	47.26

Table 5.1: *Integrated luminosities from 1999 to 2000 in pb^{-1}.*

5.2.2 Event Yield

After applying also the trigger selection the event yield, $\Delta N/\Delta\mathcal{L}$, could be checked. Proper functioning of the detector readout and the luminosity measurement should result in a constant event yield. Due to broken wires in the Central Jet Chamber a lower event yield is expected for the second part of the 1999 e^+ run. Figure 5.1 shows the event yield and the number of events which have passed the trigger selection. The period with the broken wires between 18 pb^{-1} and 25 pb^{-1} is clearly visible. Since this period of bad CJC efficiency is incorporated in the Monte Carlo simulation, it also enters the analysis. In all other regions the event yield is stable and no other plateaus are occurring in the events vs. luminosity plot.
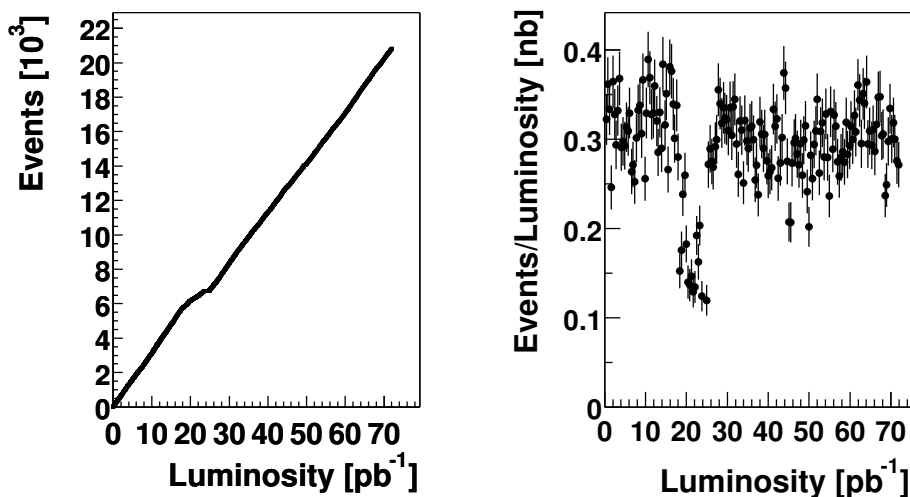
Figure 5.1: *Luminosity and event yield. The region of lower event yield between 18 pb^{-1} and 25 pb^{-1} is caused by broken wires in the CJC and is well described by the Monte Carlo simulation. In all over regions the event yield is stable.*

5.3 Measurement Techniques

5.3.1 Muon Identification

A muon candidate is defined by a track link of a track measured in the central or forward muon detector with an inner track or by an inner track extrapolated into the calorimeter and identified as minimal ionising particle. The inner tracks measured in the Central or the Forward tracker have to satisfy standard requirements listed in appendix A.1.

Track Reconstruction in the Central Muon Detector

Muons with an transverse momentum greater than 1.5 - 2.0 GeV are able to traverse the calorimeters and to reach the Central Muon Detector. The track reconstruction program of the Central Muon Detector [Kle92, Lan98] searches for muon track candidates in two steps. First a pattern recognition program groups wire and strip hits into 'associations' neglecting hits which are noisy and dead according to the Bos bank IQWS ('Iron Quality Wire and Stripes') [Blo87]. From these associations wire and strip track segments are derived via a two-dimensional mapping. After quality checks track segments may be linked together and finally the wire and strip information is combined. Essential for the quality of the strip track segment is the presence of at least one wire hit in the same module. Information from the calorimeter towers of the Tail Catcher is used to solve ambiguities of the strip information. In case of absent strip information the information from the calorimeter towers is combined with the wire track segments.

In the second step a track fit delivers the final kinematic values and imposes certain quality criteria. The resulting tracks in the muon system will not extend from the barrel into the endcaps or vice versa, since the pattern recognition program is run separately for the barrel and the endcaps. This leads to a significant decrease of the iron track efficiency in this transition region which is compensated by the use of calorimeter muons.

Muon Track Linking

The tracks reconstructed in the Central Muon Detector are only used to identify muon candidates. The H1 reconstruction program tries to link these tracks to the inner tracks measured by the Central or forward trackers. A successful link builds a hypothesis for a muon candidate. The momentum of the muon candidate is solely derived from the inner track.

Final Muon Candidates

Final muon candidates have to be selected from the above hypotheses. A program from the H1 Physics Analysis package (H1PHAN) performs this task when analysing the reconstructed data [H1SWa, Wes00]. First it selects inner tracks fulfilling standard quality criteria (appendix A.1). For each accepted inner track a possible muon identification, either a track in the muon system or an identified minimal ionising particle, is searched. The desired quality of the track measured in the muon system is described in appendix A.2. Basically a minimal number of layers which have been hit and maximal distance of the track extrapolation from the vertex are required.

Also the linking of the track measured in the Central Muon Detector to the inner track can be specified. For tracks with a high transverse momentum ($P_t > 3.5$ GeV) the linking routine might run into trouble resulting in a very low χ^2 of the fit. The H1 reconstruction code saves this events by adding 2 to the resulting χ^2. The muon selection code of the H1PHAN software package is focused on low energetic muons and rejects all of these muon candidates. To avoid

this drawback a simple geometrical matching in θ and ϕ is introduced as sufficient criteria for these high P_t muon candidates.

The H1PHAN program ignores completely the inner and outer muon boxes (section 3.2.4). The philosophy is that these layers do not qualify the muon since no material has to be traversed. However they are used by the H1 reconstruction routines and allow to improve slightly the efficiency. Provided that the total number of layers which have been hit is large enough, good muon candidates can be found using this information. The muon finder has been adapted to accept muons which have at least one hit in the inner part of the instrumented iron, either a wire hit, a strip hit or a signal in the calorimetric towers. The final quality of these muons may be chosen by defining a minimal total number of hits, which is the sum of all hits, i.e.: the hits in the inner muon boxes, the hits in the outer muon boxes, the inner wire layer hits, the strip hits and the tower hits. Events passing the standard criterion 'minimal number of inner iron wire layers' will not be affected by this requirement. A similar identification criterion has already been used by [Keu98].

The muon identification in the Liquid Argon evaluated by the H1 reconstruction program plays only a role for low energetic muons. The identification of a minimal ionising particle is in details described in [Smi94]. Efficiency studies can be found in one of the numerous works on J/Ψ-vector mesons [Kru01, Moh00, Smi01]. About 12 % of the selected muons are only identified with the Liquid Argon calorimeter.

The Invariant Mass

The invariant mass of the muon pair is calculated from the angles and the measured transverse momentum. The resolution of the invariant mass has been determined from the Monte Carlo simulation by comparing the reconstructed mass M_{Rec} to the generated mass M_{Gen}:

$$\bar{\sigma}_M = \frac{M_{Gen} - M_{Rec}}{M_{Gen}}.$$

Figure 5.2 shows the mean values of a Gaussian fit to the resolution. It is interesting to note the large degradation in resolution with increasing mass. Such a behaviour is expected from the theoretical resolution of a drift chamber since the resolution of the transverse momentum is proportional to the square of the transverse momentum [Blu93]:

$$\sigma_{P_t} \sim \frac{P_t^2}{L^2 B},$$

L denotes the radial length of the measured track and B the magnetic field.
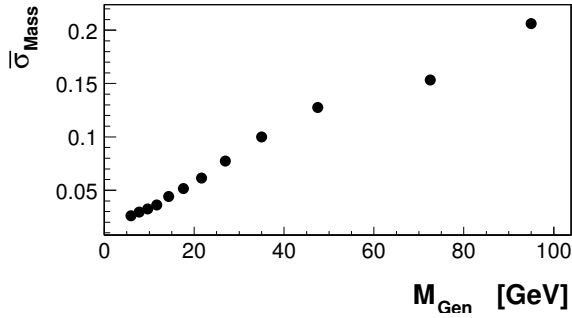
Figure 5.2: *Mass resolution derived from the Monte Carlo simulation using the GRAPE generator.*

5.3.2   Track Reconstruction Efficiency in the Central Muon Detector

Selecting elastic events with exact two tracks in the inner tracker and at least one identified muon the identification efficiency for muons is determined. Assuming that only elastic muon pair production can cause such a signature in the detector both muons should be measured in the Central Muon Detector. Inefficiencies arise from events in which the second track is not identified as a muon. To avoid a bias for the Central Muon Detector independent subtriggers are required for this special data sample. Cosmic muons are rejected with a cut on the opening angle $\alpha < 165°$. In Figure 5.3 the resulting efficiency from data is compared to an elastic LPAIR Monte Carlo. The θ, ϕ and P_t dependences of the reconstruction efficiency is clearly visible and rendered properly by the Monte Carlo. Due to lack of statistics this method, which
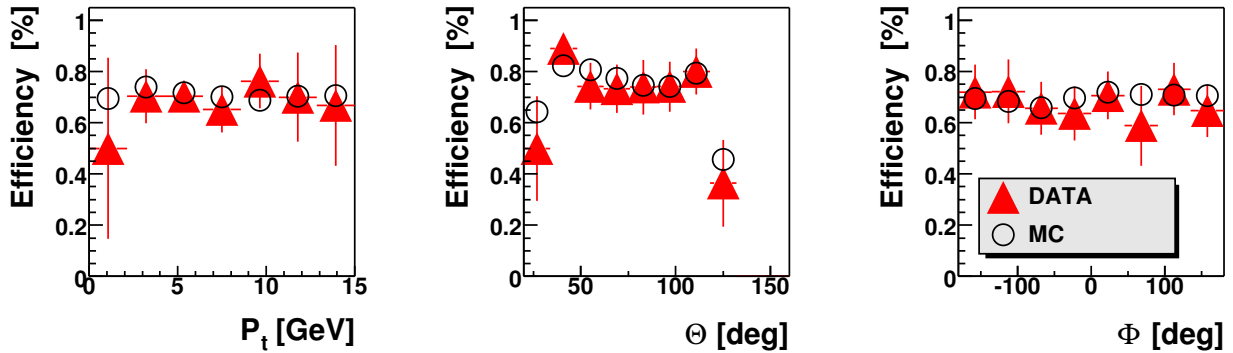
Figure 5.3: *Reconstruction Efficiency of tracks in the Central Muon Detector.*

uses ep data, determines the reconstruction efficiency mainly for low transverse momenta. In a dedicated analysis of cosmic muons [Swa98] the reconstruction efficiencies has been determined up to momenta of 80 GeV. It has been shown that the reconstruction efficiency is independent of the momentum of the muons (this analysis was carried out for muons with a momentum of at least 5.0 GeV). The reconstruction efficiency depends only for very low energetic muons ($P < 2.0$ - 3.0 GeV) on the momentum [Moh00], since these muons may not have enough energy to enter the Central Muon Detector.

5.3.3 Reconstruction of the Hadronic Final State

An event may consist of a leptonic and a hadronic part. The leptonic part consists of muons and possibly of electrons identified by the standard H1 electron finder (QESCAT). All hadronic particles measured in the calorimeters form the hadronic final state (HFS). The measurement of the hadronic final state serves to determine the kinematic variables of the event. To measure the energy deposit in the calorimeters neighbouring cells are grouped to 'clusters'. Energy deposits and tracks belonging to identified leptons are excluded from this procedure. The energy deposits behind identified muons are excluded within a cylinder of 35 cm radius for the electromagnetic, and 70 cm radius for the hadronic part. Since particles on their way to the calorimeter loose some energy in the drift chambers, the energy of the clusters is underestimated. To cope with this a special algorithm combines clusters and low momentum tracks ($P_t^{Track} < 2$ GeV). All low momentum tracks passing the track selection criteria are extrapolated into the calorimeters. The energy measurement of tracks and clusters is combined if clusters are found within a cylinder of certain radii. If the track energy is smaller than the cluster energy within this cylinder, the innermost clusters are discarded until the discarded energy equals the track energy. If the track energy exceeds the cluster energy, the track energy is attributed to the HFS-object. The radii of the cylinders differ for the electromagnetic and hadronic calorimeter part and are 30 cm or 70 cm respectively. The HFS-objects have been calibrated with an H1 low Q^2 calibration.

5.4 Multi Muon Selection

The analysis is not carried out in the full phase space of di-muon production. Though it is desirable to use the full phase space, technical and practical limits force restrictions (section 5.4.1). Unavoidable means to reject non physical background entail losses of data events, but result in a cleaner data sample (section 5.4.2). An inelastic subsample gives access to the proton structure (section 5.4.4) while the elastic counterpart offers the possibility to verify the luminosity measurement.

5.4.1 Phase Space

The analysis aims to investigate muon production mechanism at high scales. Suitable scales for this classification are the transverse momenta of the muons or the invariant mass. Requiring a minimal mass scale of 5 GeV allows all muons from J/Ψ - candidates to be rejected. To assure a high selection efficiency one muon must have a transverse momentum greater than 2 GeV, while for the second muon a minimal transverse momentum of 1.75 GeV is required. The analysis is restricted to the polar range $20° < \theta < 160°$ which is given mainly by the extent of the Central Trackers. The physical quantities determining the phase space for this analysis are summarised in table 5.2.

Number of muons	≥ 2
Polar angle	$20° \leq \theta \leq 160°$
Transverse momentum	$P_t^{\mu_1} \geq 2.00$ GeV
	$P_t^{\mu_2} \geq 1.75$ GeV
Invariant mass	$M_{\mu,\mu} \geq 5$ GeV

Table 5.2: *Chosen phase space.*

5.4.2 Background Rejection

Three different sources of background exist which are relevant to a muon analysis. Background from muons contained in the cosmic radiation, background from particles of the beam halo and background from misidentified kaons or pions.

Z-Vertex	$|\Delta zvtx| \leq 40$ cm
Isolation	$D_{TRACK,JET} > 1$
Opening angle	$\alpha_{DTRA} < 165°$
	$\alpha_{DTNV} < 165°$
$\theta_{DMUO}^{\mu 1} + \theta_{DMUO}^{\mu 2}$	for $\alpha_{DTNV,DTRA} > 150°$:
	$170° > \theta_{DMUO}^{\mu 1} + \theta_{DMUO}^{\mu 2} > 190°$
Event timing	$\Delta t_0 < 25$
Track timing	$t_{upper,\mu} - t_{lower,\mu} < 20$

Table 5.3: *Background rejection. The isolation requirement allows to exclude fake muons. The collinear cosmic events are suppressed by the cuts on the opening angle and the sum $\theta_{DMUO}^{\mu 1} + \theta_{DMUO}^{\mu 2}$. The three listed conditions use information from the inner tracker (vertex fitted tracks (DTRA) and non vertex fitted tracks(DTNV)) and the Central Muon Detector (DMUO) To improve the cosmic rejection additional timing cuts are applied.*

Cosmic Background

The main background results from cosmic radiation. 'Cosmic muons' crossing the vertex region of the H1-detector can be distinguished from ep physics events due to their distance from the interaction point, their timing behaviour and their collinearity.

To reject all collinear muon pairs the opening angle between the two muons is required to be smaller than $165°$. The opening angle can be calculated from the vertex fitted tracks, α_{DTRA}, or from non-vertex fitted tracks, α_{DTNV}. Events are rejected if they fulfil either condition $\alpha_{DTRA} > 165°$ or $\alpha_{DTNV} > 165°$. Since the vertex fit of cosmic muon may cause a false θ-measurement, the usage of the non-vertex fitted tracks helps to reject these cosmic events. Figure 5.4 shows the impact of the condition $\alpha_{DTRA} > 165°$. The majority of the cosmic events is already rejected by this cut alone. The necessity of using not only the vertex fitted tracks (DTRA)
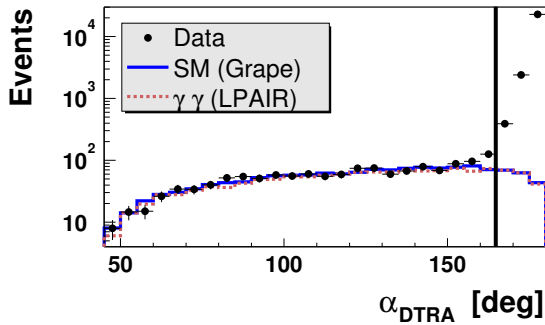
Figure 5.4: *Rejection of cosmic background. All events with $\alpha_{DTRA} > 165°$ are rejected for the analysis.*

but also the non vertex fitted tracks (DTNV) is illustrated in figure 5.5. At $\alpha_{DTRA} > 150°$ still a data excess is seen (figure 5.5, left plot). The right plot shows the α_{DTNV}-distribution which reveals an significant data excess at $\alpha_{DTNV} > 165°$. By rejecting these events almost all the remaining cosmics can be excluded from the sample. An example of an event which is rejected using the measurement of the non vertex fitted tracks gives figure 5.6. One can see two tracks drawn in the lower part of the inner tracker, the one matching the calorimeter spots is the non vertex fitted track, while the vertex fitted track appears at a lower θ angle and thus provokes a distortion of this event.

Still some cosmic events remain in the data sample. Especially at high transverse momenta or at high invariant masses cosmic events appear in the measured spectra. A typical event still passing the opening angle cuts is shown in figure 5.7. It can be seen that the inner tracks do not match very well the tracks in the Central Muon Detector and the energy deposition in the calorimeter. A simple cut on the opening angle of the inner tracks therefore would not be able to reject events of this type.
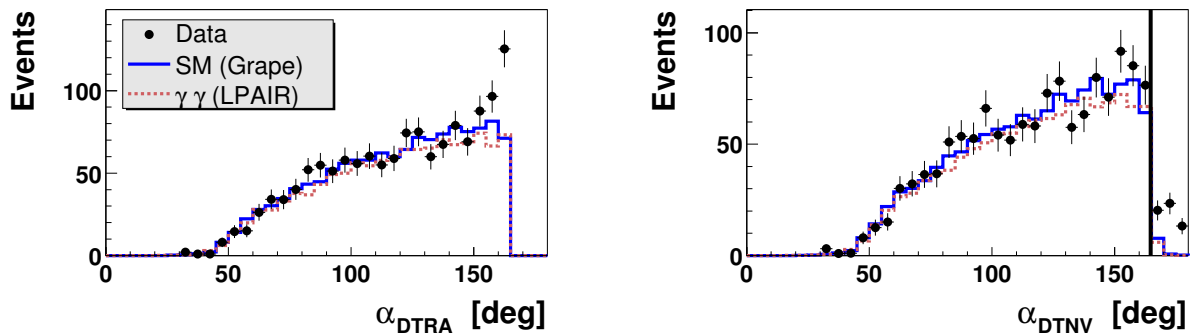
Figure 5.5: *Refinement of the cosmic rejection. After the cut on α_{DTRA} is applied still some cosmic events are remaining in the sample. The left plot shows an excess at $\alpha_{DTRA} > 150°$ which corresponds mainly to the events with $\alpha_{DTNV} > 165°$. The right plot shows the opening angle calculated with non vertex fitted tracks for the same event sample. For $\alpha_{DTNV} > 165°$ no events at all are expected.*
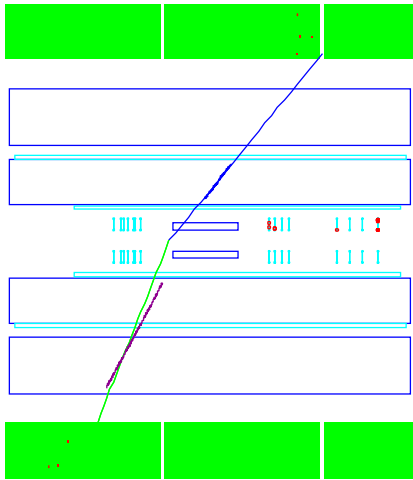
Figure 5.6: *Event rejected by $\alpha_{DTNV} > 165°$. Two track fits are visible in the lower part of the detector: the DTRA fit to the nominal event vertex and the fit considering only the wire hits (DTNV). It is obvious that the inclusion of the nominal vertex leads to a worse result in this special case.*

To improve the cosmic rejection the track measurement of the Central Muon Detector can also be used. Cosmic candidates with an opening angle greater than $150°$ must fulfil the additional condition $170° < \theta_{\mu 1} + \theta_{\mu 2} < 190°$. With the third condition for the opening angle some few events with a very twisted linking are rejected.
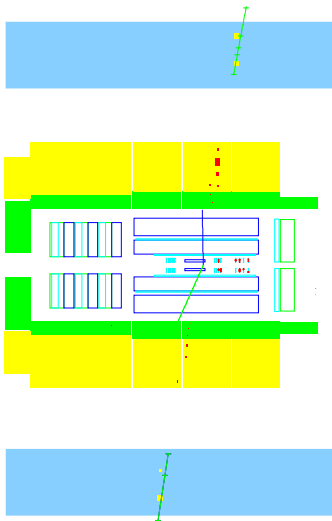
Figure 5.7: *Event rejected by a cut on the polar angle measured in the Central Muon Detector.*

Another powerful distinction between ep physics and cosmic events is the different timing behaviour. ep physics events are in coincidence with the HERA Clock while cosmic events are independent from this clock. The general event timing which is measured by the Central Jet Chamber and the timing of each track attributed to a muon serve the cosmic rejection: the difference of the event timing to the mean t_0 of the corresponding run period is restricted to values below 25 'ticks' (4.8 ns) and the difference between the timing of the two muons ordered according to their polar angle may not exceed 20 (3.8 ns). Figure 5.8 clearly shows that almost only cosmic events which appear at large opening angles are rejected. The cut on the timing difference is demonstrated in figure 5.9 by comparing events with large opening angles to events

Figure 5.8: *Event rejection with the general event timing. Shown are all events which passed the preselection. Cosmic muons appear at large values of the opening angle and are largely suppressed by the cut indicated by the horizontal line. A cut imposed during the reconstruction rejects events with an event $t_0 \gtrsim 60$. The y-axis shows the time measured in 'ticks' (1 tick $= 0.192$ ns).*
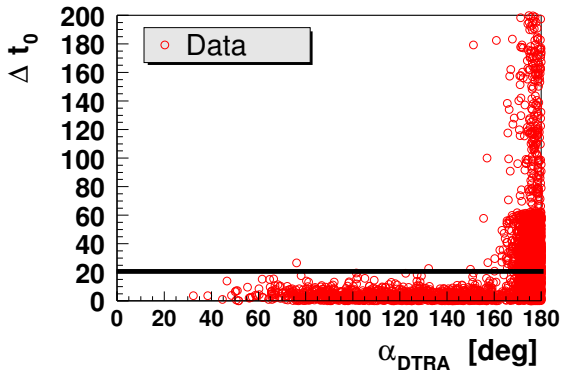
with small opening angles, thus by comparing mainly cosmic events to mainly ep physics events. The latter ones are centred around zero, while the timing difference of the cosmic dominated sample strongly peaks around 18. Since the timing difference is defined as $t_{lower\mu} - t_{upper\mu}$ a positive value is expected for cosmic events which enter first the upper part of the detector and then arrive at the lower part. Since of course also ep physics event are contained in the sample with large opening angles, this distribution is not symmetrical, but has a long tail extending to negative values of the timing difference. Cosmic events are of course also rejected by the
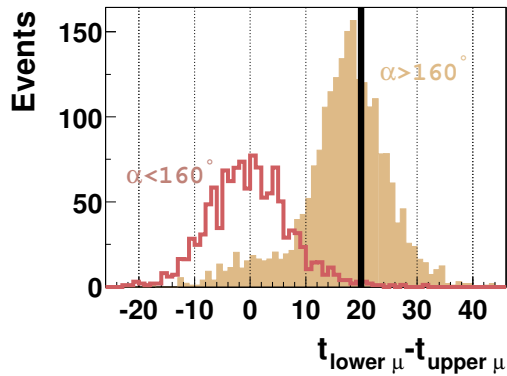
Figure 5.9: *Cut on the difference of the track timing. The plot shows all preselected events. The y-axis shows the time measured in 'ticks' (1 tick $= 0.192$ ns).*

z-vertex restriction and by selecting only tracks with a maximal 'distance of closest approach' to the vertex. A possible improvement may be obtained by the information of a special 'cosmic fit' which tries to link two tracks to one common track. The distance from the vertex of this common fit may allow some optimisation of the cuts. However, at high transverse momentum the cuts have to be tighter and an optimisation of the cosmic rejection will gain only in the region of low transverse momenta.
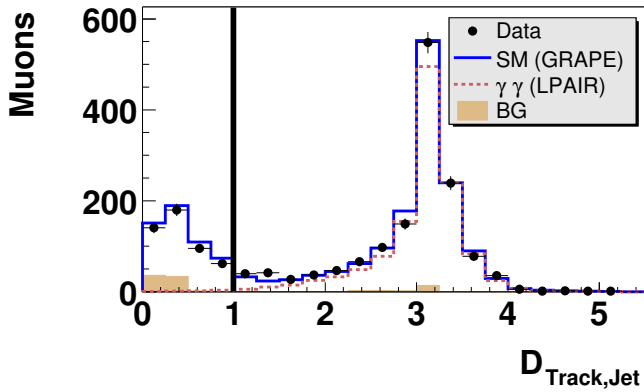
Figure 5.10: *Isolation requirement. Shown is the minimal distances of each muon to the next track or jet $D_{Track,Jet}$. The black line shows the cut for low momentum muons, which is relaxed to 0.5 for muons with $P_t > 10$ GeV. The total standard model expectation SM (GRAPE) is dominated by the GRAPE expectation for events passing the indicated cut and by muons stemming from heavy quark decays for events failing the isolation requirement.*

Beam Halos

Beam halos typically traverse the detector parallel to the z-axis. They are suppressed by searching only for muons coming from the vertex. The possible background stemming from beam halos are overlaid events, an incidental coincidence of an ep physics event and a beam halo. Standard beam halo finders reject one event from the final data sample.

Misidentification

Hadrons may fake muons by several mechanisms. Especially pions and kaons may reach the Central Muon Detector and may be either misidentified as muons ('sail through') or they may decay collinear into a muon before having reached the Liquid Argon calorimeter which leads to the identification of one muon candidate ('in-flight decay'). Hadronic energy leaking out of the Liquid Argon calorimeter can evoke showers in the Central Muon Detector which may cause the reconstruction of a track (see also [Lan98]). These hadronic background sources are almost completely suppressed by an isolation criterion. The minimal distance of the identified muon in the η-ϕ plane to the next measured track or to the next identified jet $D^{\mu}_{Track,Jet}$ has to be larger than one. For muons with high transverse momenta ($P_t > 10$ GeV), the isolation requirement is relaxed to $D_{Track,Jet} > 0.5$. The impact of the isolation requirement can be estimated from figure 5.10. The two-photon process ('$\gamma\gamma$ (LPAIR)') is hardly affected by this cut. This cut reduces the background ('BG') of misidentified muons stemming mainly from neutral current Monte Carlos completely. The tiny background contribution at larger values of $D_{Track,Jet}$ consist of events where one muon has a large value of $D_{Track,Jet}$ and the other fails the distance requirement. In addition also muons stemming from heavy quark decays in boson-gluon fusion are largely suppressed by this cut. These muons give the dominant contribution at small distances ($D_{Track,Jet} < 1.0$). The requirement of at least two well identified muons minimises background from pions and kaons further.
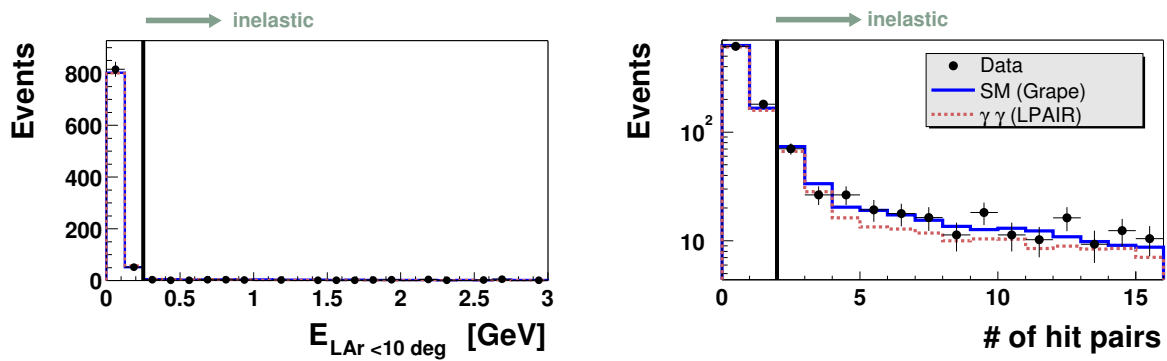
Figure 5.11: *Separation between elastic and inelastic muon production. The left plot shows the energy deposited in the forward part of the Liquid Argon Calorimeter and the right plot the number of hit pairs detected in the Forward Muon System.*

5.4.3   Inelastic and Elastic Events Samples

Elastic and inelastic muon production are separated from each other by tagging the remnants of the dissociated proton. This method has been developed for diffractive (eg. [Sch01]) and heavy flavour analysis (eg. [Smi01, Smi02, H102a]) and can also be adapted here. A dissociated proton may be tagged either in the forward part of the Liquid Argon, in the pre-toroid layers of the Forward Muon Detector or with the Proton Remnant Tagger 3.2.5. An event is classified as inelastic if a signal in one of these subdetectors is found, i.e.:

- the energy deposited in the forward region of the liquid Argon ($\theta < 10°$) is greater than 0.5 GeV;

- more than one hit pair is found in the pre-toroid layers of the Forward Muon Detector (section 3.2.4);

- one of the first three scintillators of the Proton Remnant Tagger has been hit.

92 % of the inelastic (quasi-elastic and deep inelastic) events of the GRAPE simulation have an inelastic proton tag, while about 10 % of the elastic events are misidentified as inelastic events.

As explained in [Smi01] noise in the Forward Muon System (~ 5.5 %) as well as inefficiencies of the Proton Remnant Tagger have to be considered to achieve a good agreement with the Monte Carlo. Figure 5.11 explains the separation with the energy in the forward region of the Liquid Argon calorimeter (left) and with the number of hit pairs of the Forward Muon Detector (right). Distributions for the two data samples are shown in figure 5.12. Both data samples agree reasonably well with the Monte Carlo prediction.
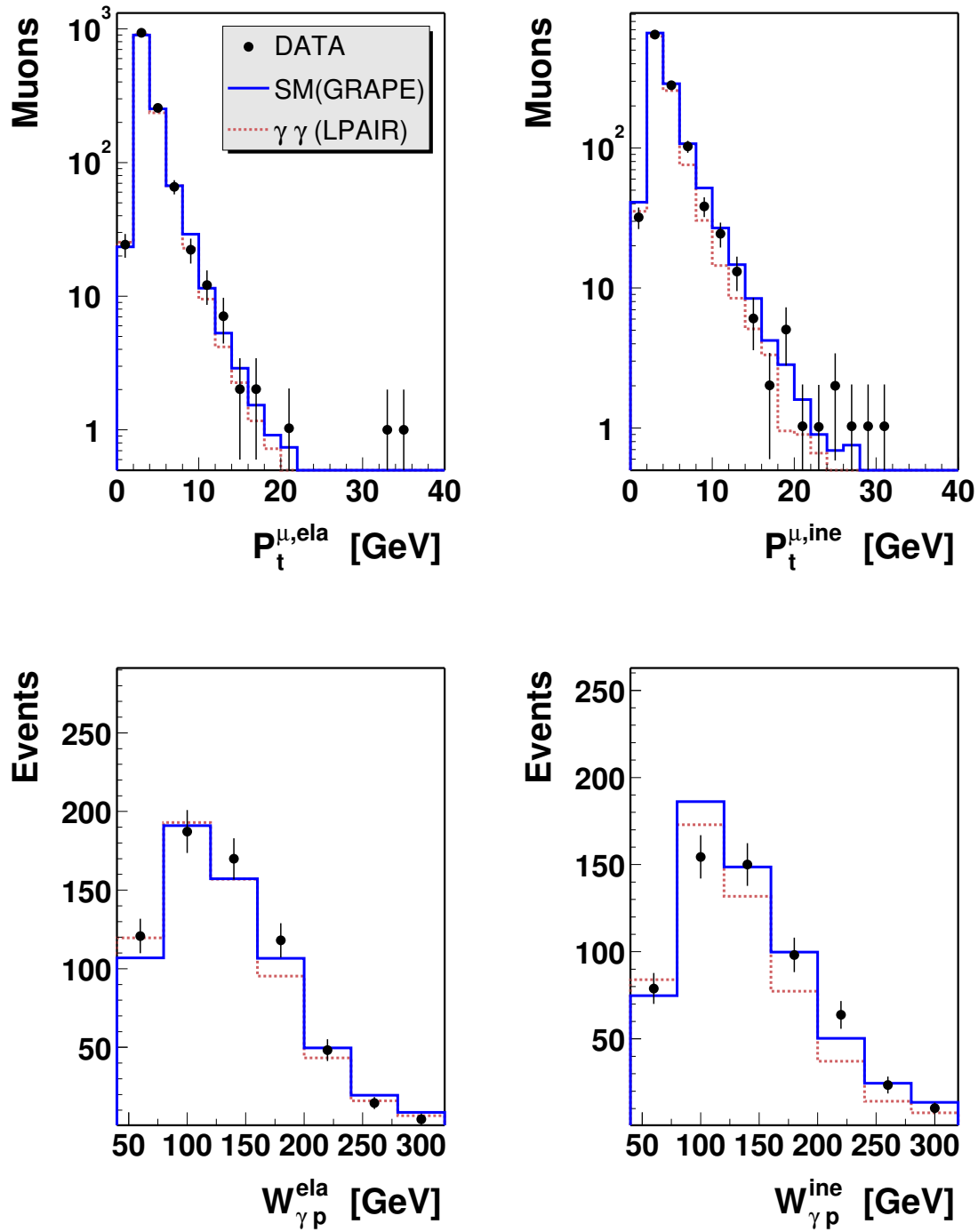
Figure 5.12: *Event distributions for the elastic (left) and inelastic (right) sample. The upper plots show the transverse momenta of both muons and the lower plots show the invariant mass of the photon-proton system.*

	inclusive	elastic	inelastic
Data	1243	664	579
SM (GRAPE)	1253	647	606
$\gamma\gamma$ (LPAIR)	1189	651	550

Table 5.4: *Final data sample. The number of selected events are compared to the Standard Model prediction (SM). The contribution of the dominating two-photon process ($\gamma\gamma$ (LPAIR)) is also listed.*

5.4.4 Final Data Sample and Subsamples

With the selection described above 1202 events are found within a luminosity of 70.9 pb^{-1}. All events are di-muon events. No event with more than two muons has been found. Since the data events have to be weighted with the prescale of the L1 subtrigger (section 4.1), the sum of these weights have to be compared to the Monte Carlo expectation. The 1202 events correspond to a sum of weights of 1243.05. Whenever data is compared to Monte Carlo these weights are applied. Numbers, which are given, are rounded to full integers and events have to be understood as weighted events. In table 5.4 this sum of weights is compared to the expectation from the Standard Model prediction ('SM (GRAPE)'). The predication is dominated by the two photon process $\gamma\gamma \longrightarrow \mu\mu$. The full Standard Model prediction (SM (GRAPE)) is the sum of all electroweak processes simulated with GRAPE and all other contributions (table 5.5). Table 5.4 also compares the contribution of the dominating two-photon process without contributions from other processes to the data and to the Standard Model prediction 'SM (GRAPE)'. The simulation of this process alone has been performed with the generator LPAIR (section 2.5.1). To indicate that this prediction contains only the two-photon process it is labelled '$\gamma\gamma$ (LPAIR)'. Neglecting negative interference effects between the Bremsstrahlungs processes and the two-photon process one would expect from 'SM (GRAPE)' a larger prediction than from '$\gamma\gamma$ (LPAIR)'. But this must not always be the case, because of the small contribution from the other processes. In phase space regions with negligible contribution from other processes two different generators are compared to each other and thus the expectation of '$\gamma\gamma$ (LPAIR)' may exceed the one from 'SM (GRAPE)'. Table 5.4 shows that data and expectation 'SM (GRAPE)' match within one per cent for the inclusive data. It is possible to explain the data only with the two-photon process.

Process	Generator	Expectation
$\Upsilon \longrightarrow \mu\mu$	DIFFVM	12.9
$\gamma\gamma \longrightarrow \tau\tau \longrightarrow \mu\mu$	LPAIR	3.7
$c\bar{c}, b\bar{b} \longrightarrow \mu\mu$	AROMA	8.8
$Z^0 \longrightarrow \mu\mu$	GRAPE	0.16

Table 5.5: *Contribution of the other processes with two isolated muons in the final state.*
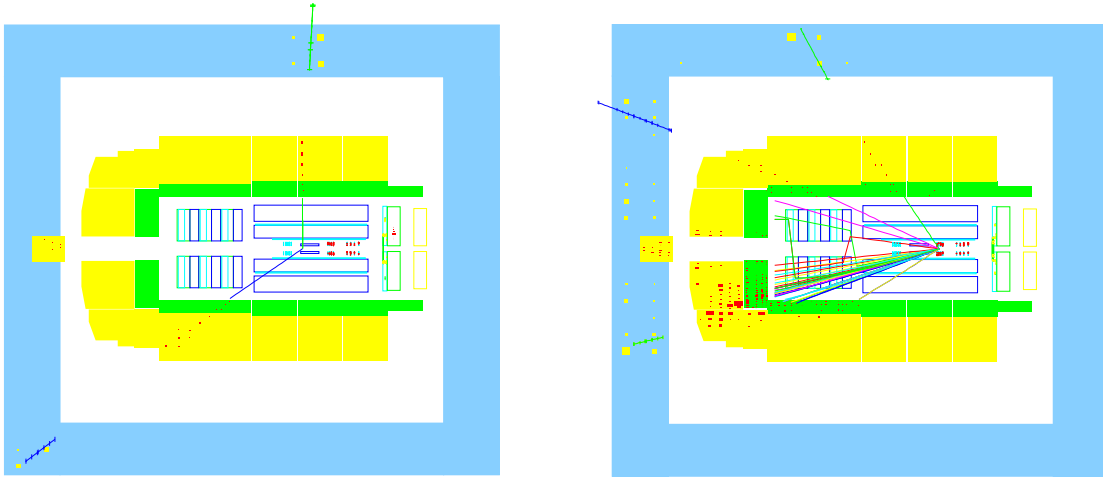
Figure 5.13: *The event with the highest di-muon mass ($M_{\mu,\mu} = 80$ GeV) (left) and event with the highest transverse momentum of the hadronic final state ($P_t^X = 47$ GeV) (right).*

The expectation from '$\gamma\gamma$ (LPAIR)' is only 5 % smaller than the data. Considering the statistical error of roughly 3 % '$\gamma\gamma$ (LPAIR)' is in nice agreement with the measurement. The contribution of other processes is almost negligible.

As interesting subsamples inelastic and elastic muon production are contained in this selection. After the separation of these two processes, which is described in section 5.4.3, 664 events are classified as elastic and 579 events are assigned to inelastic muon production. The expectation for these subsamples is also listed in the table 5.4. The difference between the prediction of 'SM (GRAPE)' and '$\gamma\gamma$ (LPAIR)' is larger for the inelastic muon production than for elastic muon production. The contribution $c\bar{c}, b\bar{b} \longrightarrow \mu\mu$ (table 5.5), which occurs only in the inelastic channel explains a small part of the difference. The other processes, which are listed in table 5.5, contribute more or less equally to both elastic and inelastic muon production. The remaining difference of 8 % is explained mainly by the different structure functions which are used to simulate the quasi-elastic part (section 2.5.2). The simulation of the other part of inelastic muon production, the DIS part, can only explain smaller differences, since the chosen parton densities are the same for both generators (chapter 5).

Two of the most exciting events merit special attention. The event with the highest di-muon mass is shown in the left event display of figure 5.13. This elastic event has an invariant mass of 80 GeV. Due to the large mass resolution of roughly 14 GeV at M_Z the event may be interpreted as a Z^0-candidate. In the SpaCal an electron candidate is visible which has an energy of 8 GeV. The event shown in the right event display is the event with the highest transverse hadronic momentum ($P_t^X = 47$ GeV). More properties of these two events are given in table 5.6.

$M_{\mu,\mu}$	$P_t^{\mu 1}$	$P_t^{\mu 2}$	P_t^{miss}	P_t^X	E_e
80 GeV	$35^{+4.1}_{-3.3}$ GeV	$33^{+2.3}_{-1.9}$ GeV	3.7 GeV	0 GeV	8.2 GeV
13.6 GeV	$42^{+3.7}_{-3.2}$ GeV	$1.8^{+0.04}_{-0.04}$ GeV	3.6 GeV	47 GeV	10.2 GeV

Table 5.6: *Event properties of the two events shown in figure 5.13.*

The reliability of the selection is further supported by the distributions shown in figure 5.14. Both the angular distributions, the polar angle difference of the two muons and the longitudinal balance $E - P_z$ agree well with the Monte Carlo prediction. Figure 5.15 presents the transverse momenta of both muons P_T^μ, the invariant mass $M_{\mu,\mu}$, the virtuality of the photon emitted from the electron, which is determined with the Jaquet-Blondel method [JB79] and the sum of the polar angle of the muons measured by the Central Muon Detector. This quantity is used for the cosmic rejection (section 5.4.2). The small plots inserted in the lower figures allow to see the tail of the distributions.

Quantities describing the muon quality are shown in figure 5.16. The number of the first layer n_{first} which has been hit , the last layer of the track n_{last} , the total number of iron layers n_{lay}, which qualifies the track, and the layer density $(n_{last} - n_{first})/n_{lay}$ are well simulated. It should be noted that distributions always show only statistical error bars. The systematical uncertainties are omitted in the figures.
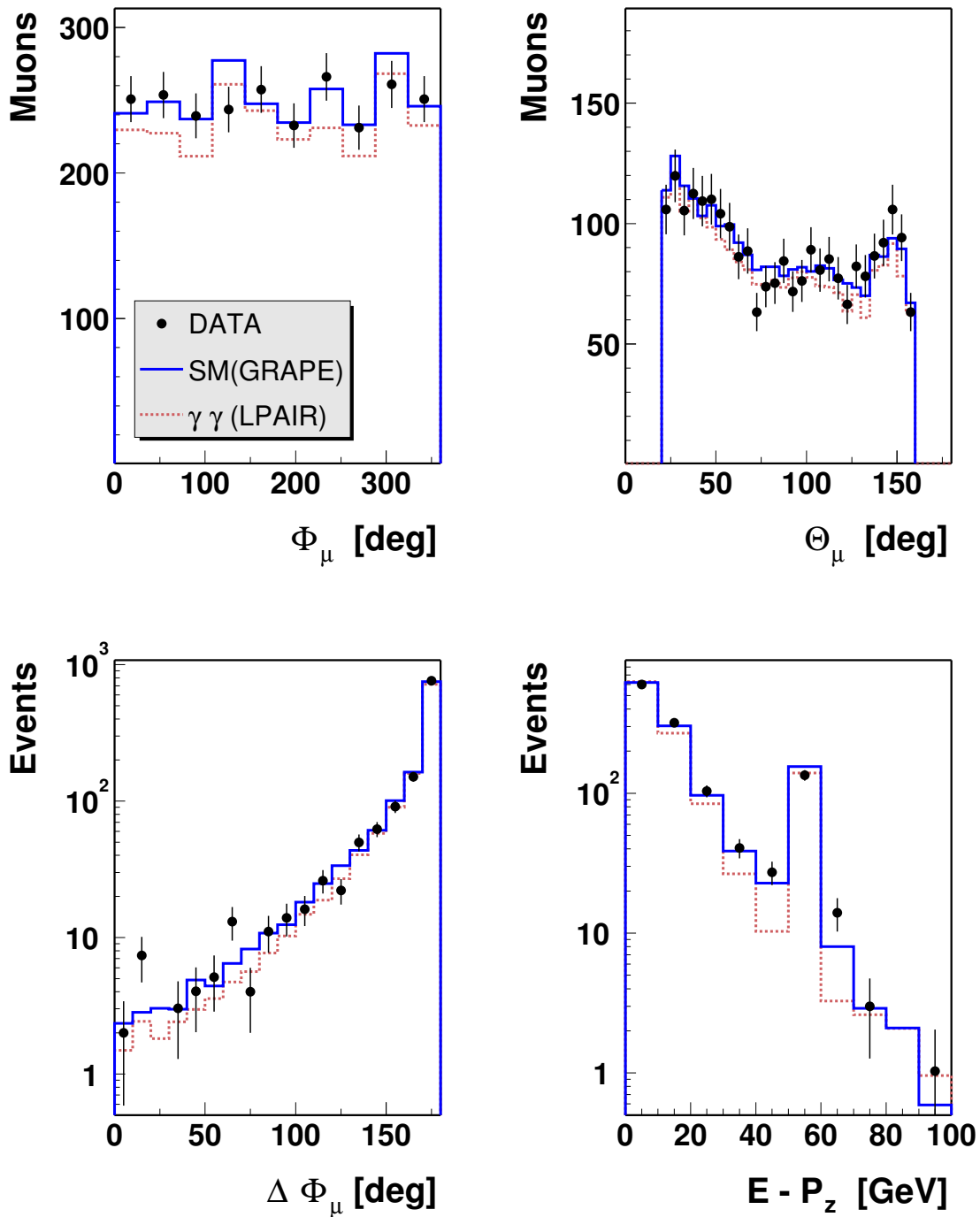
Figure 5.14: *Kinematical distributions. The angular distributions of both muons are shown in the upper plots, while the lower ones give the number of events as a function of the φ-difference and the longitudinal balance E-P$_z$ which contains a peak at 55 GeV stemming from events with identified electron. Higher values of E-P$_z$ are caused by measurement errors. Plots with the y-axis label 'Muons' contain two entries per events.*
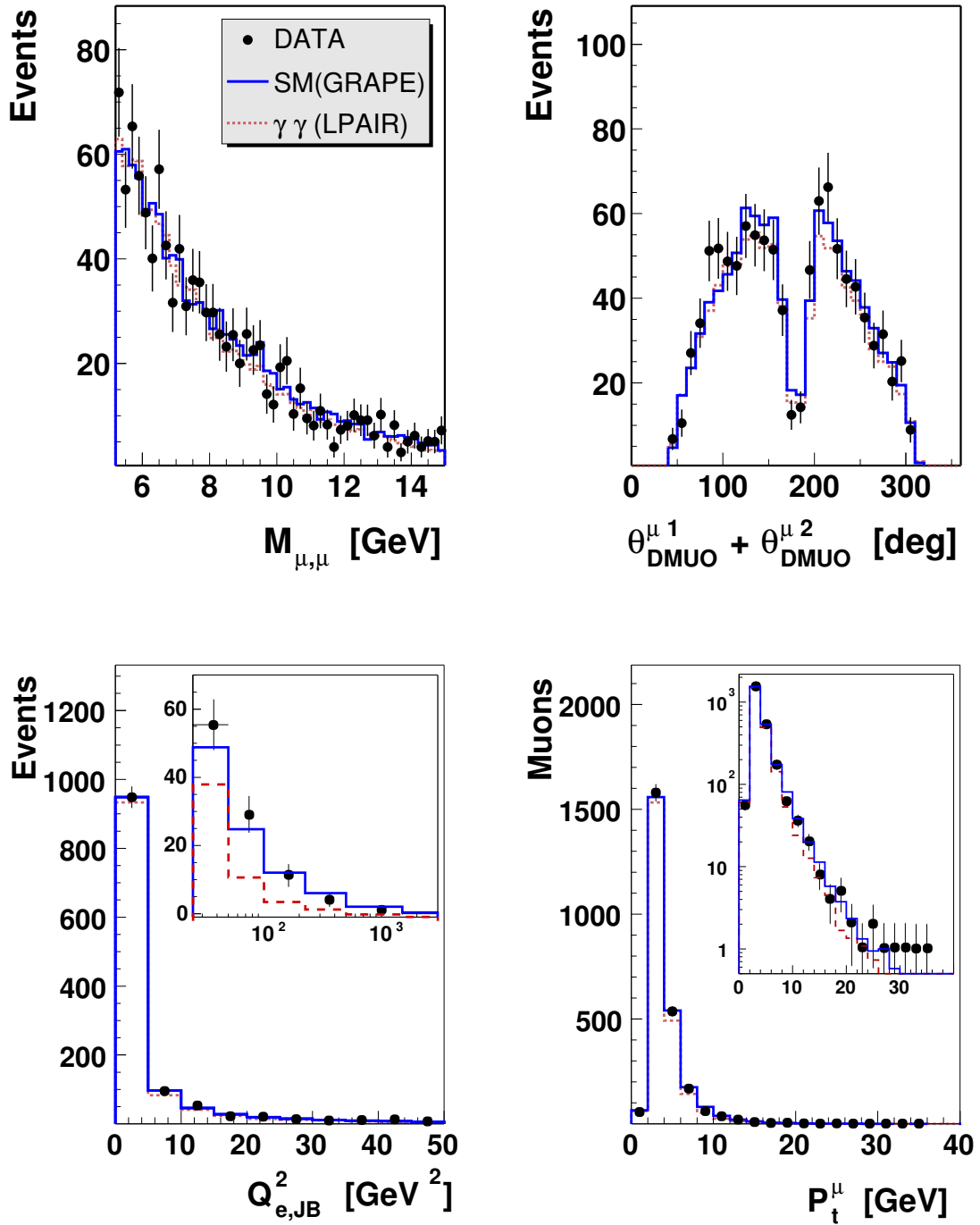
Figure 5.15: *The distributions show (clockwise from the upper left plot): the lower range of the di-muon mass, the sum of the polar angle measurement of the Central Muon Detector for events where both muons are detected in the Central Muon Detector, the transverse momentum with an insert plot in logarithmic scale, and the momentum transfer from the electron with an cutout of the tail of this distribution as inlet plot. All plots are well rendered by the simulation.*
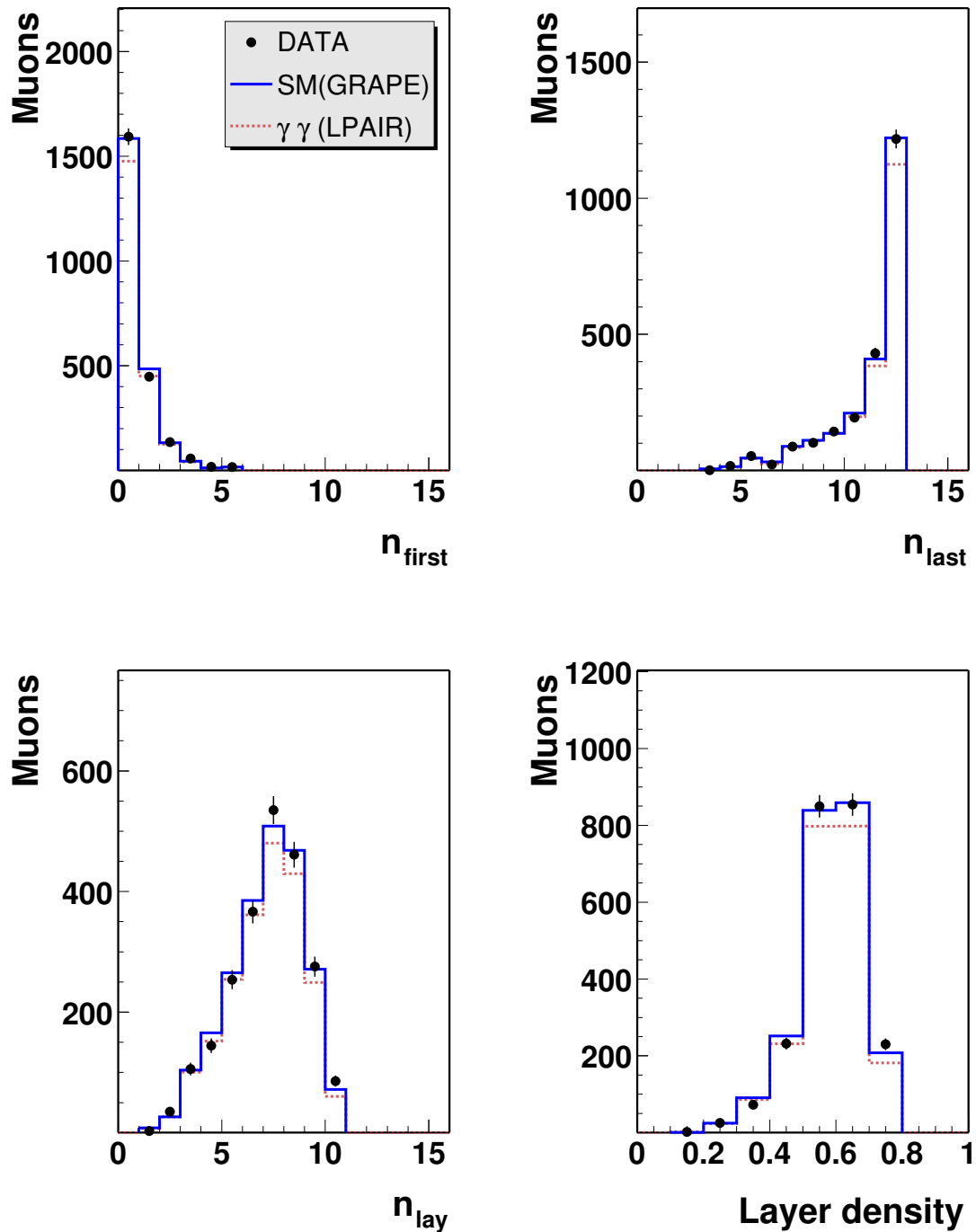
Figure 5.16: *Quantities determining the muon quality: the upper left plot gives the number of the first layer which has been hit, the upper right plot gives number of the last layer which has been hit, the lower left plot gives the number of layers within the iron which have been hit, and the lower right plot summarises the layer density.*

Cross Section Measurement

A cross section measurement of inclusive isolated multi-muon production is performed. In fact all multi-muon events turn out to be di-muon events, although in principle events with more than two muons could have entered the analysis. It is not explicitly required that the two muons have opposite charges. The measured cross section is therefore strictly speaking not a cross section of muon pair production, though only three like sign muons have been observed.

In addition the cross section of inelastic and elastic electroweak muon pair production is measured. Thus this measurement determines the cross section of all real muon pairs produced via the two-photon or Bremsstrahlungs process. The contribution of other muon production processes like the decay of vector mesons is treated as background. The procedure of the cross section determination, which is introduced in section 6.1, comprises the definition of the bin size, the evaluation of the correction factors which transform the 'raw' distribution into a cross section and the evaluation of the systematic uncertainties of the measurement. In section 6.2 differential cross sections are presented for the inclusive sample and for inelastic and elastic electroweak muon pair production. Finally the perspective of new physics is discussed (section 6.3) and total cross sections are derived (section 6.4).

6.1   Procedure of the Cross Section Determination

6.1.1   Unfolding the Data

To allow a meaningful comparison of the data with theoretical calculations the data has to be corrected for all detector effects. The influence of limited resolution, inefficiencies and mismeasurement on the data can be removed by a simple unfolding technique if the bin size matches the resolution, the data is well described by the Monte Carlo simulation and the correlation between the bins are small. To verify that the so called 'Bin-to-Bin Correction' is applicable the acceptance

($\mathcal{A}$), purity ($\mathcal{P}$) and stability ($\mathcal{S}$) are determined from the Monte Carlo simulation [1]:

$$\mathcal{A}(i) = \frac{N_{rec}(i)}{N_{gen}(i)}; \tag{6.1}$$

$$\mathcal{P}(i) = \frac{N_{gen+rec}(i)}{N_{rec}(i)}; \tag{6.2}$$

$$\mathcal{S}(i) = \frac{N_{gen+rec}(i)}{N_{gen+sel}(i)}; \tag{6.3}$$

- $N_{rec}(i)$ is number of events reconstructed in bin i;

- $N_{gen}(i)$ is number of events generated in bin i;

- $N_{gen+rec}(i)$ is the number of events generated and reconstructed in bin i;

- $N_{gen+sel}(i)$ is the number of events generated in bin i and reconstructed in any bin.

The Bin-to-Bin method consists in the application of a correction factor to each bin, which is inverse proportional to the acceptance and the trigger efficiency.

The acceptance, purity and stability for the cross section measurements are determined from the average values of GRAPE and LPAIR. The uncertainty of the acceptance correction is estimated from the difference between these two generators. Since the contribution from other processes than the two-photon process is very small in the given phase space this approach is sensible.

In the figures 6.1 - 6.3 the acceptance, purity and stability are presented as functions of different variables: the invariant mass of the muon pair $M_{\mu,\mu}$, the transverse momenta of the two muons P_t^μ, the invariant mass of the photon-proton subsystem $W_{\gamma,p}$ and the transverse hadronic momentum P_t^X. The acceptance, purity, and stability for inelastic and elastic produced muon pairs are shown in figure 6.3. The purity and the stability are required to be larger than ≈ 0.3, and the acceptance is almost always larger than 0.5, leading to a maximal correction factor of 2. The acceptance, stability and purity are well under control and show no unexpected behaviour. The purity and the stability approach one at small invariant masses (figure 6.1), because the bin size is large compared to the mass resolution in this mass range. A similar behaviour is observed for the transverse momentum (lower figure in 6.1).

Since the P_t-resolution is proportional to transverse momentum, very large bins are required for large momenta, while at small values the bin size may be tiny. This is true for the cross section as a function of the transverse momentum of course, but also for the cross section as function of the invariant mass. The bin size for these cross sections are optimised for large values, but may be larger than necessary at small values. For the invariant mass two binnings are chosen, one with larger bins at small masses and one with optimised bin sizes at small masses.

---

[1]The acceptance does not include the trigger efficiency.
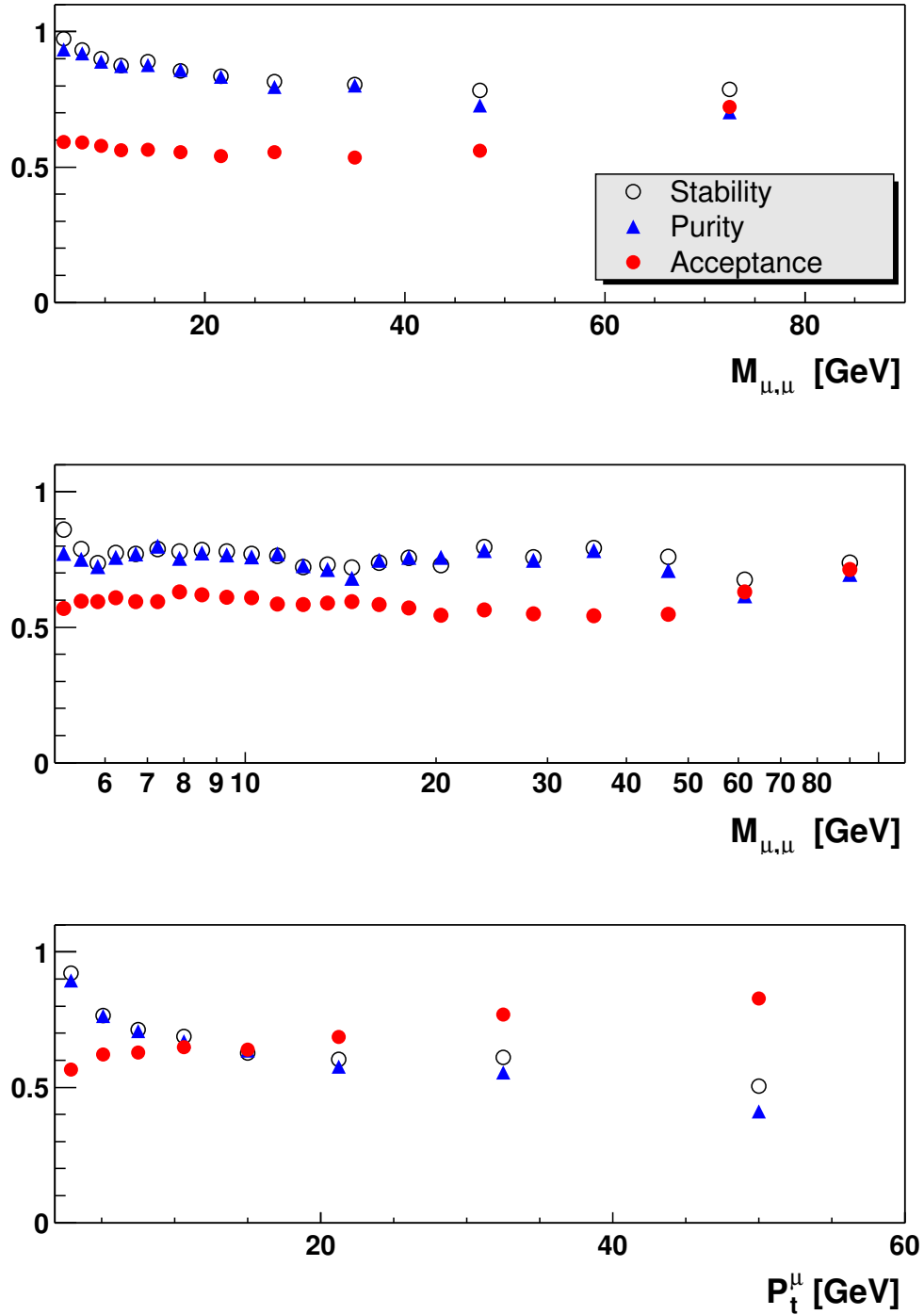
Figure 6.1: *Acceptance, purity and stability as function of the invariant mass $M_{\mu,\mu}$ and transverse momenta of the muons P_t^μ.*

Isolated Di-Muons

The differential cross section for inclusive di-muon production in a single bin of the variable $M_{\mu,\mu}$ is determined from

$$\frac{d\sigma}{dM_{\mu,\mu}} = \frac{1}{\delta_{bc}} \cdot \frac{N_{Data}}{\epsilon_t \cdot \mathcal{A} \cdot \mathcal{L}}, \tag{6.4}$$
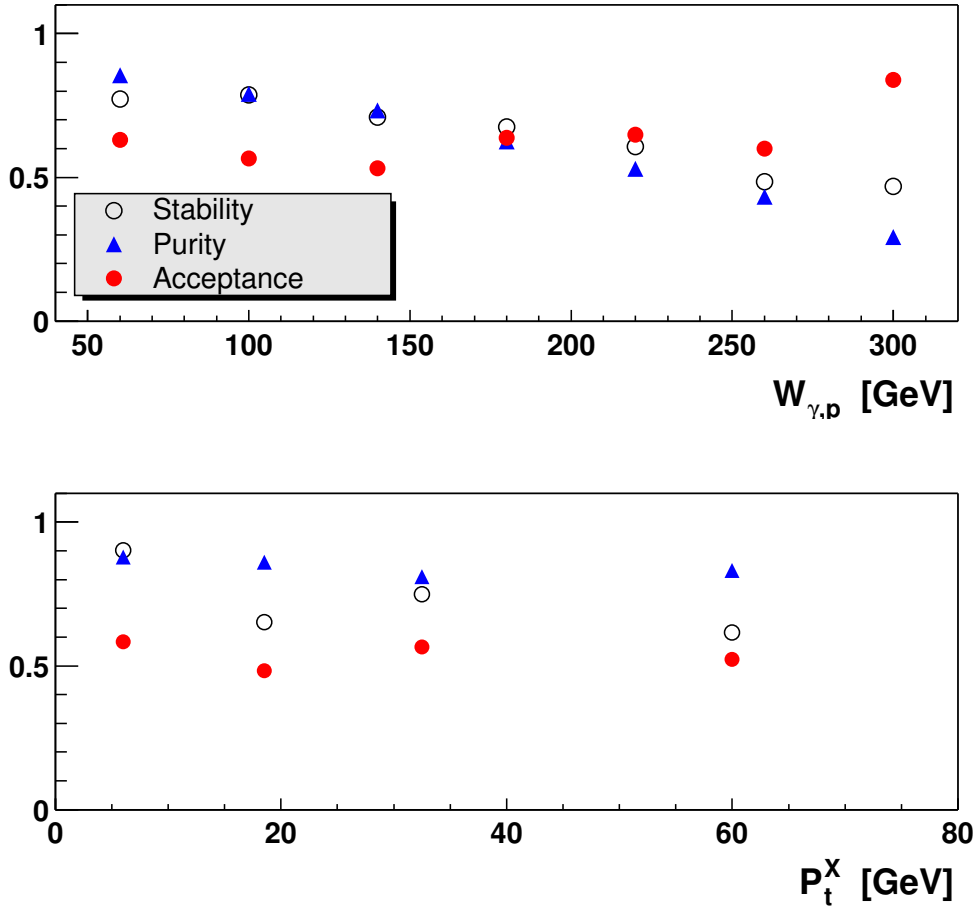
Figure 6.2: *Acceptance, purity and stability as function of the centre of mass energy in the photon-proton subsystem W_γ, p, the hadronic transverse momentum P_t^X .*

where

- N_{Data} is the number of measured events;

- ϵ_t is the trigger efficiency;

- $\mathcal{A}$ is the acceptance (equation 6.1);

- $\mathcal{L}$ is the total integrated luminosity (see 5.2.1);

- δ_{bc} corrects for the finite size of the bin i.

In analogy to equation 6.4 the cross section is also represented as a function of the transverse hadronic momentum $\frac{d\sigma}{dP_t^X}$ and the invariant mass of the photon-proton sub-system $\frac{d\sigma}{dW_{\gamma P}}$. To determine the cross section as a function of the transverse momenta of both of the muons $\frac{d\sigma}{dP_t^\mu}$ the number of measured events N_{Data} in equation 6.4 is replaced by the number of muons N_{Muon}. The resulting cross sections are presented in figures 6.4 - 6.6 (section 6.2).
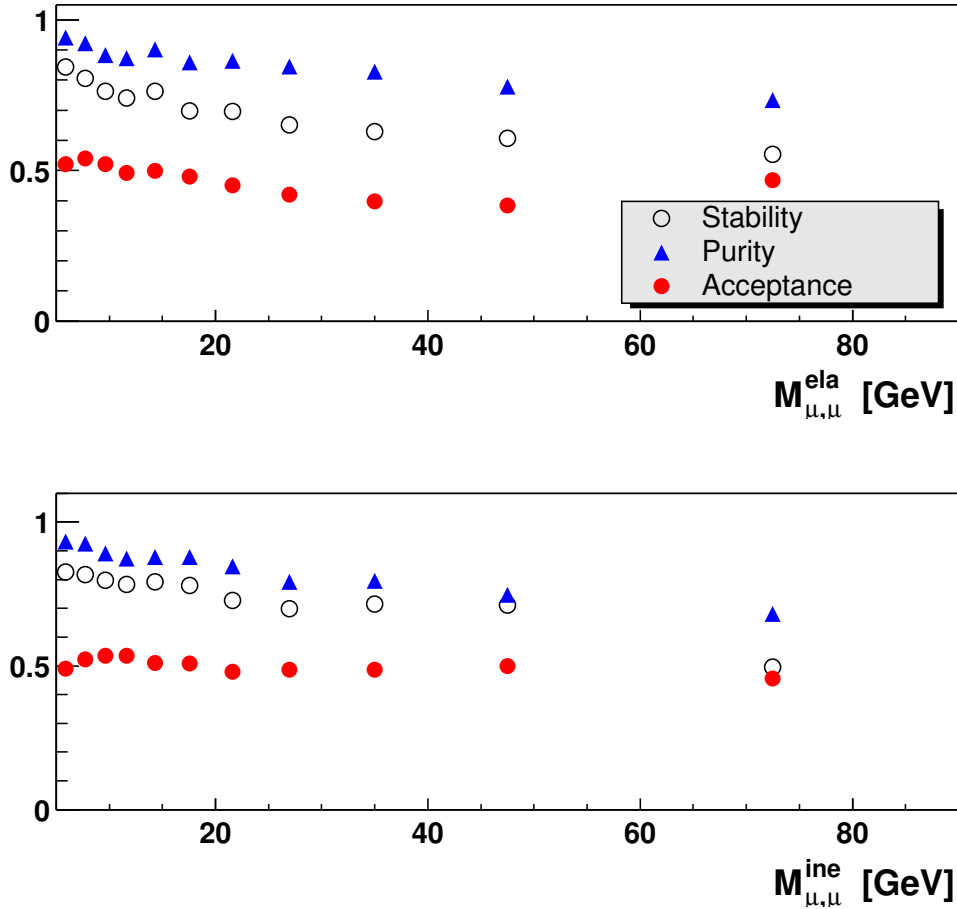
Figure 6.3: *Acceptance, purity and stability as function of the invariant mass $M_{\mu,\mu}^{ela}$ for elastic and $M_{\mu,\mu}^{ine}$ for inelastic muon production.*

Electroweak Muon Pair Production

After having determined the inclusive cross section for isolated multi-muons, the attention is now focused on the electroweak muon pair production processes, which are dominated by the two photon process. Though the difference to isolated multi-muons production is tiny since the contribution of other processes are small, the restriction to electroweak muon production processes is useful, because it allows the elastic and the inelastic production processes to be separated from each other. Technically the difference to the previous subsection occurs from the subtraction of background processes. To separate one production process from the other the background contribution from the other production process has to be taken into account by applying a correction factor. Consequently the other contributions to di-muon production, like the Υ-production or muons arising from open heavy flavour production or from τ-decays are subtracted as N_{BG} from the total number of measured events. The contribution of the resolved Drell-Yan process is neglected, since it is predicted to be extremely small.

The differential cross section for elastic or inelastic electroweak muon pair production is calculated from

$$\frac{d\sigma^{ela/ine}}{dM_{\mu,\mu}} = \frac{1}{\delta_{bc}} \cdot \frac{N_{Data}^{ela/ine} - N_{BG}}{\epsilon_t^{ela/ine} \cdot \mathcal{A}^{ela/ine} \cdot \mathcal{L}} \cdot \mathcal{C}_{FMD}^{ela/ine} \cdot \mathcal{C}_{SEP}^{ela/ine}, \tag{6.5}$$

where

- $N_{Data}^{ela/ine}$ gives the number of events which are classified as elastic or inelastic.

- $\mathcal{A}^{ela/ine}$ is the acceptance for the elastic or inelastic production processes. The acceptance $\mathcal{A}^{ela}$ differs from the acceptance for inelastic muon pair production $\mathcal{A}^{ine}$ and both cause slightly larger correction to the cross section than the acceptance $\mathcal{A}$ which is used for the inclusive measurement;

- $\epsilon_t^{ela/ine}$ denotes the trigger efficiency;

- N_{BG} denotes the number of background events from other processes;

- $\mathcal{C}_{FMD}^{ela/ine}$ corrects for the noise in the forward muon detector:
  for the cross section of elastic muon pair production $\mathcal{C}_{FMD}^{ela}$ is given by $\mathcal{C}_{FMD}^{ela} = 1 + \mathcal{F}_{\mathcal{FMD,NOISE}}$ with $\mathcal{F}_{\mathcal{FMD,NOISE}} = 5.5$ %; while for the cross section of inelastic muon pair production the correction factor is derived from: $\mathcal{C}_{FMD}^{ine} = 1 - \frac{N_{ela}^{meas}}{N_{ine}^{meas}} \cdot \mathcal{F}_{\mathcal{FMD,NOISE}}$;

- $\mathcal{C}_{SEP}^{ela/ine}$ corrects for the imperfect separation of the elastic and inelastic production process, i.e. the correction for migrations from the elastic to the inelastic sample and vice versa. The separation correction factor is determined from the relative amount of misidentified inelastic events: $\mathcal{C}_{SEP}^{ela/ine} = 1 - \frac{N_{ine,rek}^{misidentified}}{N_{ine,gen}}$. For the cross section of inelastic muon pair production the correction factor is determined in analogy.

6.1.2   Systematic Uncertainties

Several systematic uncertainties influence the measurement of muon production. Table 6.1 gives an overview of the most important sources of systematic uncertainties. The uncertainty of the luminosity determination has been derived by [Lev02], while the uncertainty of the track reconstruction is estimated with 2 % per track. Requiring two identified tracks this results in an error of 4 %. By comparing the reconstruction efficiency of the Central Muon Detector derived from data with the simulation an error for the muon identification is evaluated. The error of the trigger efficiency has been determined in chapter 4.7. The uncertainty of the measurement of the

Source	Amount
Luminosity	1.5 %
Track reconstruction	4.0 %
Muon identification	5.8 %
Trigger efficiency	5.5 %
Transverse momentum	1.7 %
Acceptance	4.0 %
Separation ela/inel	10.0 %

Table 6.1: *Sources of the systematic error of the cross section. The uncertainty of the hadronic final state plays only a role for the differential cross section as function of the hadronic transverse momentum P_t^X. The error for the separation of the elastic and the inelastic production mechanisms is only attributed to these cross sections.*

	inclusive	inelastic	elastic
Total	10 %	16 %	14 %

Table 6.2: *Total systematic uncertainties for the inclusive muon production and inelastic and elastic muon production. The uncertainty for inelastic and elastic muon production is larger because of the imperfect separation of these two different channels.*

transverse momentum is determined from the comparison of the track and cluster measurement of electrons in neutral current scattering [Meh02]. The uncertainty of the correction factor is estimated from the difference of the acceptance correction using LPAIR and GRAPE.

For the differential cross section $d\sigma/dP_t^X$ the the uncertainty of the measurement of the hadronic final state has to be considered in addition. The effect on the Standard Model prediction is evaluated by varying the hadronic energy scale by 4 % (LAr), respectively 8 % (SpaCal). This leads to an error of roughly 20 % in the highest bin, while in the other bins it ranges from 0 % to 9 %. The uncertainty of the separation of the two different production mechanisms is estimated with 10 %, which is slightly larger than in [Smi01].

6.2 Differential Cross Sections

6.2.1 Isolated Di-Muon Production

The cross section a function of the invariant mass is shown in figure 6.4. The event with the highest mass is measured at 80 GeV (see figure 5.13) . Due to the large resolution at high masses the highest mass event lies within the resolution of the Z^0-resonance. Even at this high mass range the process $\gamma\gamma \longrightarrow \mu\mu$ gives the dominating contribution to muon pair production.
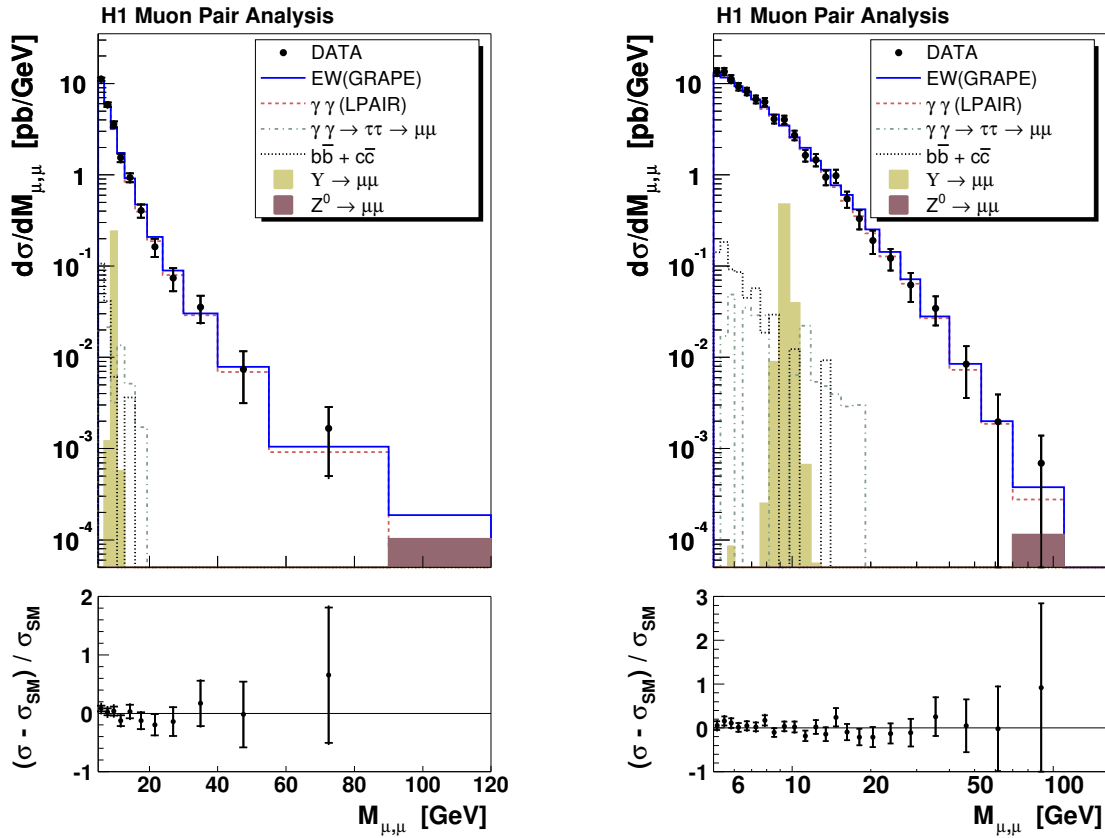
Figure 6.4: *Cross section as function of the di-muon mass in comparison to the electroweak (EW) prediction using GRAPE. The contribution of the most important electroweak muon pair production processes are also plotted individually, i.e. the contribution from the two photon process $\gamma\gamma \rightarrow \mu\mu$ (using LPAIR) and Z^0-resonance. The contribution of additional sources of muon pair production are $\gamma\gamma \longrightarrow \tau\tau$, boson-gluon fusion ($c\bar{c}$ and $b\bar{b}$) and the decay of the Υ resonances. Also shown is the relative difference between data and all Standard Model contributions (lower figures). The inner error bars represent the statistical errors. The outer error bars represent the statistical and systematical errors added in quadrature.*

The plot shows also the contributions of the other processes. As a light shaded histogram the Monte-Carlo expectation of the Υ-resonance at about 9.5 GeV is depicted. At low mass muons stemming from heavy quark ($b\bar{b} + c\bar{c}$) and τ decays give a minor contribution. The contribution of heavy quark decays is small due to the isolation requirement. In the lower figure the relative difference of the data to the Standard Model prediction is shown. The Prediction corresponds nicely to the data over the entire mass range . The cross section as a function of the transverse momentum is depicted in figure 6.5 (left). The momenta of both muons enter the cross section measurement and therefore the integral is twice the integral of the invariant mass spectrum. The highest transverse momentum is found at 50 GeV. The data slightly exceed the model between 25.0 and 40.0 GeV. The right plot of figure 6.5 presents the cross section as a function of the
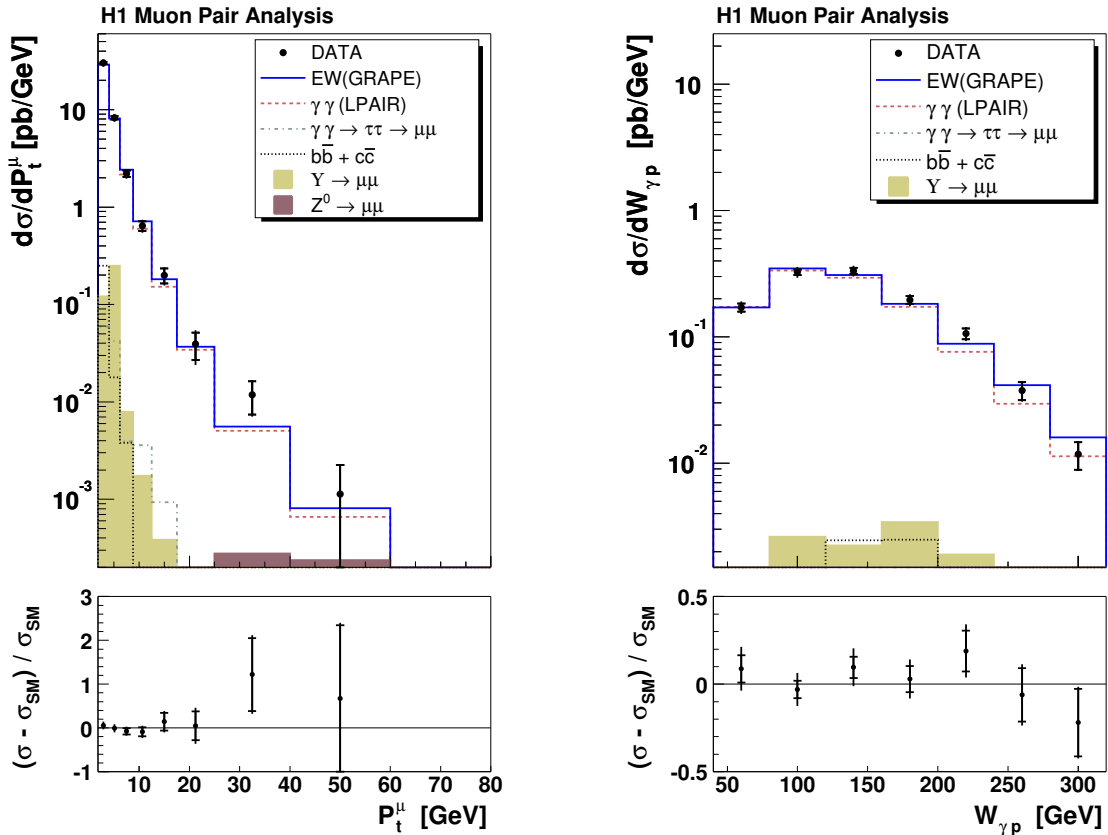
Figure 6.5: *Cross section as function of the transverse muon momenta (left) and invariant mass of the γ-proton system (right). For details see figure 6.4.*

invariant mass of the γ-proton system $W_{\gamma p}$. The shape of the distribution results from the phase space cuts applied to the data sample. The overall agreement with the Standard Model prediction is satisfactory.

The distribution of the hadronic transverse momentum shown in figure 6.6 is interesting, since in the analysis of isolated leptons with missing transverse momentum an excess at large hadronic momenta ($P_t^X > 40$ GeV) has been previously observed [H198, Mal00]. Elastic events appear at low hadronic transverse momenta in the first bin. The cross section is steeply falling. The highest hadronic transverse momentum is found at 50 GeV. At large values of the hadronic transverse momentum the Standard Model expectation is small. In the last bin one event is found and 0.16 are predicted, which corresponds to a two sigma excess. This encourages measurements with increased statistics. The bins with higher statistic do not differ from the prediction.

To draw conclusions from the di-muon sample which allow to judge on the isolated leptons the distribution of the missing transverse momentum is helpful (see figure 6.7). Also in an intrinsically
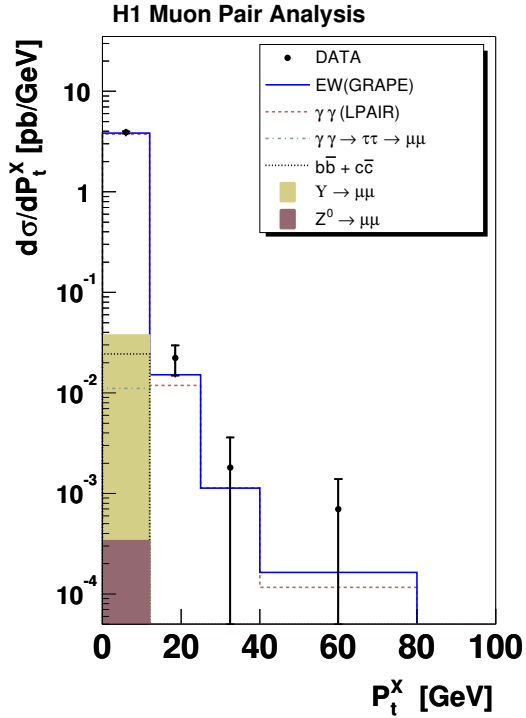
Figure 6.6: *Cross section as function of the hadronic transverse momentum. For details see figure 6.4.*
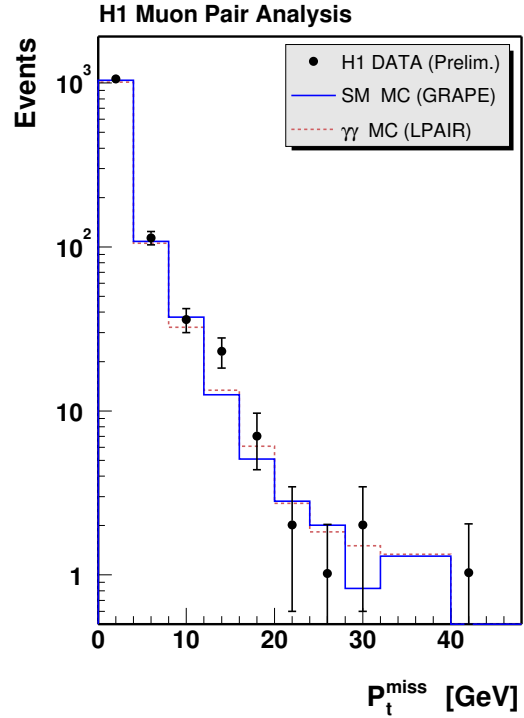
Figure 6.7: *Distribution of missing transverse momentum.*

P_t-balanced event sample a some events with missing transverse momentum are expected. The highest event in the P_t^{miss} distribution is found at more than 40 GeV. Events with large missing transverse momenta result from the poor resolution of the tracking devices, which is sufficiently well reproduced in the Monte Carlo simulation.

6.2.2   Electroweak Muon Pair Production

The cross sections as function of the invariant mass for inelastic and elastic produced muon pairs are shown in figure 6.8. Both cross sections match well with the prediction derived from GRAPE. Only the mass bin ranging from 40 to 55 GeV shows a deficit since it is not populated for the elastic channel. However, this is not significant regarding the expected statistics in this bin. To be able to compare better with the inclusive measurement (see figure 6.4) the binning is kept. Inelastic muon pair production gives access to the photon density in the proton [Art91, Lev91]. Tables listing the results of the measurement can be found in the appendix B.
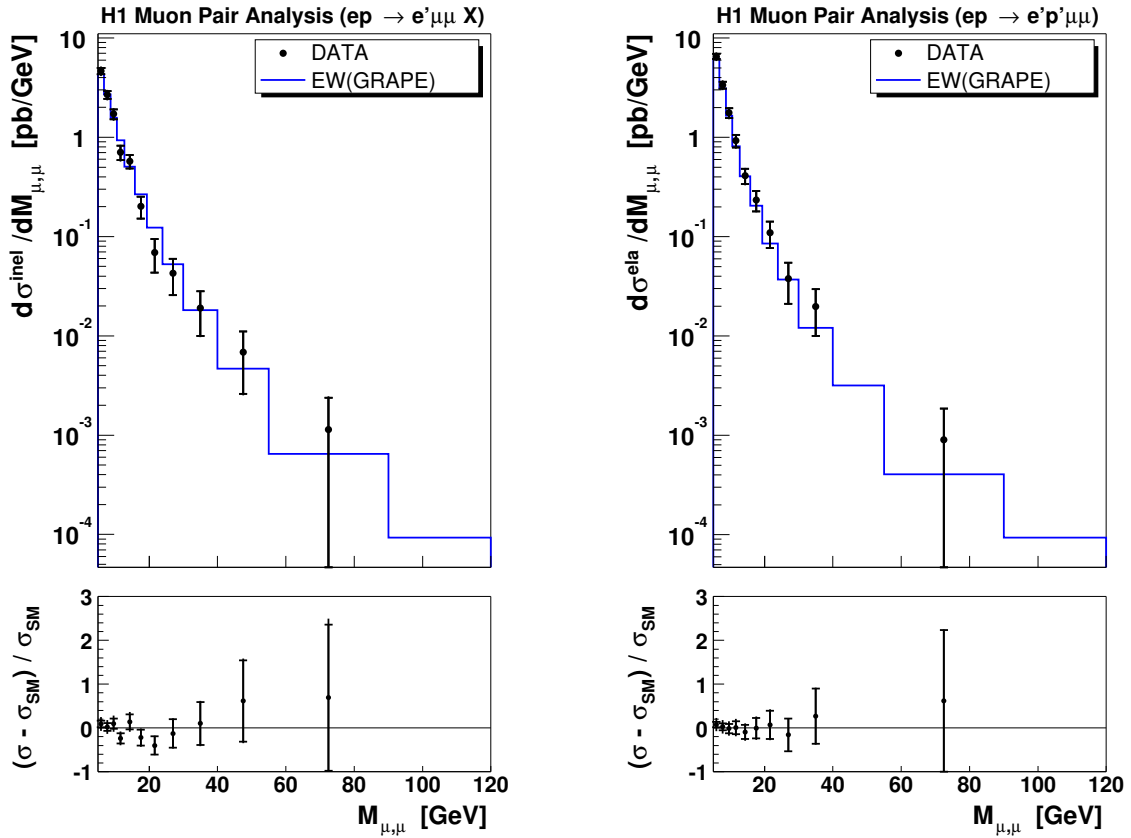
Figure 6.8: *Cross section as function of the invariant mass of inelastically (left) and elastically (right) produced muon pairs.*

6.3 Perspectives of New Physics

In neither the inclusive, nor the elastic, nor the inelastic channel was an evidence of a new resonance or new physics found. The absence of any signal allows to determine exclusion limits on physics beyond the Standard Model (section 2.4). Upper limits on the cross section and on the couplings of the doubly charged Higgs $H^{\pm\pm}$ to the leptons h_{ll} can be derived as a function of the doubly charged Higgs mass at 95 % confidence level following a Bayesian approach [PDG96], which takes both statistical and systematic uncertainties into account. The limits at 95 % confidence level on the product of the $H^{\pm\pm}$ production cross section and the decay branching ratio $\sigma(ep \longrightarrow eH^{\pm\pm}X) \times BR(H^{\pm\pm} \longrightarrow l^{\pm}l^{\pm})$ for the muonic decay $H^{\pm\pm} \longrightarrow \mu^{\pm}\mu^{\pm}$ as a function of the doubly charged Higgs mass are shown in the left plot of figure 6.9 and compared to the limits derived in a H1-electron analysis [Val02]. The limits in the electron channel are more restrictive due to a higher efficiency, different phase space and a larger amount of integrated luminosity ($\mathcal{L}_{ee} = 115.2$ pb). Remaining candidate events cause the difference between observed and expected limits.
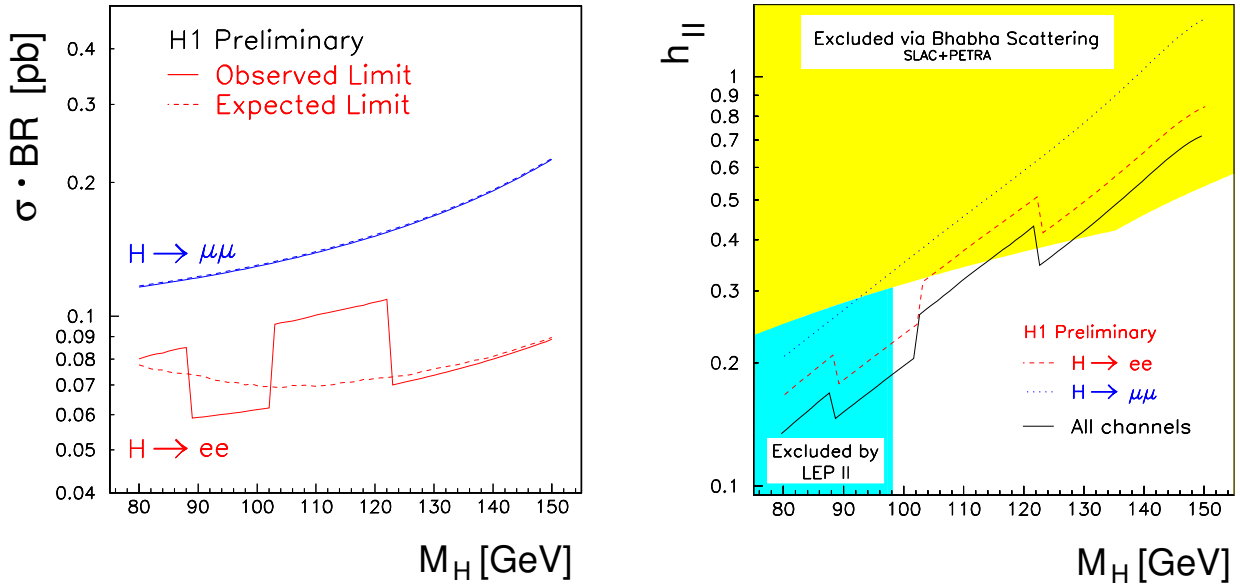
Figure 6.9: *Upper limits at 95 % confidence level on $\sigma(ep \longrightarrow eH^{\pm\pm}X) \times BR(H^{\pm\pm} \longrightarrow l^{\pm}l^{\pm})$ (left plot) and exclusion limits on the couplings h_{ll} at 95 % confidence level as function of the doubly charged Higgs mass (right plot). The upper dashed curve gives the limits in the muon channel assuming $BR(H^{\pm\pm} \longrightarrow l^{\pm}l^{\pm}) = 1/3$ [H102b].*

Exclusion limits on the coupling $h_{ll=\mu\mu,ee}$ as function of the doubly charged Higgs mass for the muonic and electronic decay channel and for the combination of these two channels are presented in the right plot of figure 6.9 assuming a branching ratio of 1/3 for each channel. The results are compared to indirect limits from Babha scattering [Swa89] and limits from direct search at OPAL [OPA01]. The combination of the H1 muon and electron channel [H102b] extends the excluded region to higher masses than reached in previous searches for pair production at LEP.

The charge of the muons is of special interest in models beyond the Standard Model. Due to the absence of any candidate events in the non-excluded mass range a further background
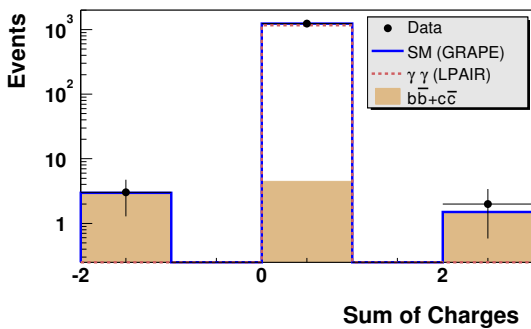
Figure 6.10: *Sum of the charges of the two muons. Events with two positively charged muons appear at 2 in the plot and events with two negatively charged muons at -2. SM (GRAPE) assigns the Standard Model prediction, i.e. the sum of the dominating electroweak contribution simulated with GRAPE and contributions from the decays of heavy particles (section 5.4.4).*
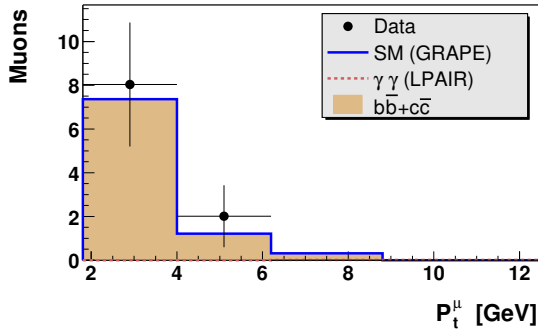
Figure 6.11: *Distribution of transverse momenta of like sign muons.*
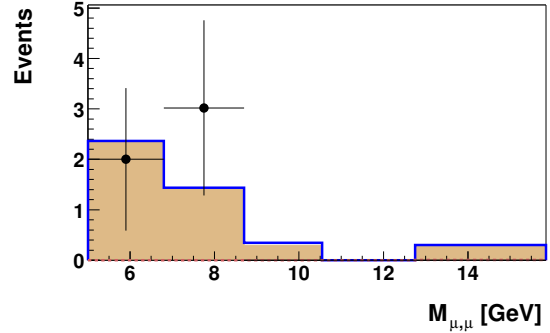
Figure 6.12: *Invariant mass distribution of like sign di-muon events.*

suppression by demanding like sign muons was obsolete. However an examination of like sign muon events is interesting. The distribution of the sum of the charges of the two muons is depicted in figure 6.10. Five events have been observed with an equal charge measurement in the inner tracker. Among them are two events whose charge measurement can be confirmed by the Central Muon Detector. The distributions of the transverse momenta and of the invariant mass of these events are shown in figure 6.11 and figure 6.12. The distributions of like sign muons are consistent with the expectation from heavy quark decays in boson-gluon fusion (shaded histogram). Events with like sign muons appear only at small di-muon masses and at low transverse momenta. The charge measurement is well described by the Monte Carlo simulation. The contribution of the two-photon process is completely suppressed by the charge requirement.

To complement the analysis of the main di-lepton channels still the μe channel is missing. In context of the multi-electron analysis the inspection of the high electron-muon mass range is of interest. On the base of this analysis, i.e. one muon in the polar angular range $20° < \theta < 160°$, $P_t^{\mu} > 5$ GeV and an H1 standard electron identification no high mass $(M_{e\mu} > 80$ GeV) event can be observed in the μe-channel.

6.4 Total Cross Sections

The total cross section for inclusive electroweak lepton pair production and for elastic and inelastic produced electroweak lepton pairs is listed in table 6.3. Due to the imperfect separation of the two production mechanisms the sum of the elastic and inelastic produced cross section is not exactly equal to the total cross section. The resulting cross sections are compatible with the GRAPE prediction as given in the table.

	inclusive	inelastic	elastic
σ [pb]	46.5 $\pm$1.3 $\pm$ 4.7	20.8 $\pm$0.9 $\pm$ 3.3	25.2 $\pm$ 1.0 $\pm$ 3.5
σ_{GRAPE} [pb]	46.2	21.5	24.6

Table 6.3: *Total cross sections compared to the Grape prediction.*

Cross Check of the Luminosity Determination

Since the elastic muon pair production is calculable in QED, this process could in principle be used to measure the integrated luminosity. The standard luminosity measurement at H1 uses the Bremsstrahlungs processes and achieves an error of 1.5 % which is dominated by systematic uncertainties. Although the available statistics are too small to be comparable, the luminosity can be calculated from the obtained results:

$$\frac{\mathcal{L}_{\mu\mu}}{\mathcal{L}_{H1}} = \frac{\sigma_{measured}}{\sigma_{theory}} \implies \mathcal{L}_{\mu\mu} = 70.9 \text{ pb}^{-1} \cdot \frac{\sigma_{measured}}{\sigma_{theory}} . \tag{6.6}$$

This yields $(72.6 \pm 2.8 \pm 10.2)$ pb^{-1} , which is consistent with the value measured by the H1 luminosity system. Due to the large errors this method cannot compete with the H1-standard luminosity determination.

Conclusions

Results

This analysis presents the first H1 measurements of isolated muon pair production $ep \longrightarrow e\mu\mu X$ at centre of mass energies of $\sqrt{s} \approx 318$ GeV using the $e^{\pm}p$ data from 1999-2000. More than 1200 di-muon events with invariant masses between 5 GeV and 80 GeV have been observed. Events with more than two muons have not been found. The measured events are dominantly produced by photon-photon collisions. As well as testing QED and the photon spectrum of the proton this analysis provides constraints on backgrounds to searches for processes beyond the Standard Model.

Emphasis has been placed on the selection of well identified and well measured muons isolated from other tracks or identified jets. Crucial is the muon trigger efficiency which has been determined from data after verification with muons stemming from cosmic radiation. The trigger efficiency has been maximised by combining triggers sensitive to muons with triggers specialised on the detection of the hadronic final state. This gives access to muon pairs at large hadronic transverse momenta. A trigger efficiency of more than 70 % and an acceptance of roughly 50 % have been obtained. It was possible to minimise the systematical errors to 10 %.

Cross sections have been presented as function of various variables. Inelastic $ep \longrightarrow e\mu\mu X$ and elastic $ep \longrightarrow e\mu\mu p$ electroweak muon pair production have been separated from each other by tagging the proton remnant. For both production processes differential cross section have been derived as function of the di-muon mass. Total cross sections for electroweak muon pair production have been measured in the chosen phase space for the inclusive data, as well as for the inelastic and the elastic data sample:

$$\sigma_{vis}^{incl} = (46.5 \pm 1.3 \pm 4.7) \text{ pb}$$
$$\sigma_{vis}^{ine} = (20.8 \pm 0.9 \pm 3.3) \text{ pb}$$
$$\sigma_{vis}^{ela} = (25.2 \pm 1.0 \pm 3.5) \text{ pb}.$$

Both the differential and the total cross sections agree well with the Standard Model prediction. The absence of any evidence of physics beyond the Standard Model allows to determine restrictive exclusion limits on speculative theories like doubly charged Higgs production. Five like sign muon events are observed in concordance with the expectation from heavy quark decays in boson-gluon fusion.

Muon Pairs vs. Other H1 Lepton Analyses

This analysis complements the analysis of multi electron pair production where deviations from the prediction have been observed at large di-electron masses [H102e, Val02]. It is also of interest in relation to the analysis of events with a lepton and missing transverse momentum [H102d], which see a 4.8-σ excess at large transverse hadronic momenta. In contrast to these other lepton pair analyses no excess has been be identified. But it has been proven that our experimental device is fully reliable in the considered acceptance region and electroweak muon pair production is sufficiently well understood. Although neither excess has been confirmed by the ZEUS experiment, the search for an understanding of the observed deviations motivates further research also in the di-muon channel. A further attempt to verify or falsify the H1 results could only be achieved by a significant increase in the integrated luminosity. Relaxing the muon quality requirements and extending the polar angular range will lead to a small improvement on the cost of higher systematic uncertainties.

The main difference to the electron analysis is the ambiguity due to the presence the beam electron, which enhances contributions of rare processes and is responsible for a large increase of the Standard Model prediction. To complement the analysis of all di-lepton channel still the μe channel is missing, though the appearance of high mass events may be already excluded in the analysed acceptance region.

Muon pair production, where one muon remains undetected causing missing transverse momentum, forms the most important background to the isolated lepton analysis. Muon pairs with large hadronic transverse momenta have been measured, one event has been found in the region of the isolated lepton excess. The prospects to obtain a definite conclusion on the behaviour of the spectrum tail are limited. In any case, not only the two-photon process, but the complete electroweak contribution, which increases the prediction by at most 20 %, have to be taken into account for judgements on this spectrum. Additional contributions from Bremsstrahlung with photon conversion into low invariant mass muon pairs outside the analysed phase space may lead to an increased background expectation. The use of the muon trigger as adapted in this work would improve the isolated muon analysis. It should allow to extend the phase space towards lowest hadronic transverse momenta. This region has been inaccessible due to restrictions to hadronic final state triggers.

Selection

A.1   Track Selection

Combined			Central			Forward		
p_t	>	0.15 GeV	p_t	>	0.1 GeV	p	>	0.5 GeV
θ_{min}	>	0.0°	θ_{min}	>	20.0°	θ_{min}	<	6.0°
θ_{max}	<	40.0°	θ_{max}	>	160.0°	θ_{max}	<	25.0°
R $_{Start}$	<	50 cm	R $_{Start}$	<	60 cm	R_0	<	10 cm
DCA	<	5.0 cm	DCA	<	5.0 cm	N_{seg}	>	2
σ_{p_t}/p_t	<	1.0	RPTPHTH	=	1.0	$N_{plan.\ seg}$	>	1
$\chi^2_{\text{FT-CT-link}}$	<	50.0	Length	>	10.0 cm	χ^2_{trackfit}	<	10.0
$\chi^2_{\text{vertexfit}}$	<	50.0				$\chi^2_{\text{vertexfit}}$	<	25.0

Table A.1: *Track selection.*

- R $_{Start}$: radial distance of the first hit to the z-axis

- R $_0$: radial distance of a non vertex fitted track to the nominal vertex

- DCA: distance of closest approach to the primary event vertex

- $\chi^2_{\text{FT-CT-link}}$: χ^2 of the fit linking the forward and the central track segment

- $\chi^2_{\text{vertexfit}}$: χ^2 of the fit to the primary event vertex

- χ^2_{trackfit}: χ^2 of the fit to the hits in the tracking detectors

- Length: difference of the radii at the start and at the end of a track

- σ_{p_t}/p_t: relative error of the momentum measurement

- $N_{\text{plan. seg}}$: number of hit planar segments

- N_{seg}: number of hit planar and radial segments

- RPTPHTH: variable used to remove double tracks

A.2   Muon Selection

Condition		Barrel	Forward Endcap		Backward Endcap	
			$< 25°$	$> 25°$	$< 145°$	$> 145°$
	$\rho_{xy,x,x}$	100 cm	100 cm		100 cm	
	$\rho_{z,y,y}$	100 cm	100 cm		100 cm	
I	N_{first}	> 3	> 3		> 3	
	$N_{lay,iron}$	> 2	> 6	> 3	> 3	> 6
II	N_{total}	> 5	> 5	> 5	> 5	> 5

Table A.2: *Layer conditions for muon identification. Conditions I or II have to be fulfilled.*

- $\rho_{z,y,xy}$: radial distances of the extrapolated iron track to the vertex

- N_{first}: layer number of first layer which have been hit

- $N_{lay,iron}$: number of hit streamer tube layers excluding the muon boxes

- N_{total}: total number of hits, i.e.: $N_{total} = N_{lay,iron} + N_{lay,muonboxes} + N_{Towers} + N_{Strips}$

Data Tables

B.1 Inclusive Muon Pair Production

$M_{\mu,\mu}$ [GeV]	$d\sigma/dM_{\mu,\mu}$ [pb/GeV]	δ_{stat} [%]	δ_{tot} [%]
5.00	20.1	4.4	9.2
6.80	11.2	5.8	9.9
8.70	6.61	7.6	11
10.55	3.39	11	13
12.75	2.90	11	14
15.85	1.40	17	19
19.30	0.75	23	24
23.90	0.45	29	30
30.00	0.36	33	35
40.00	0.11	57	59
55.00	0.06	70	72
90.00	—	—	—

Table B.1: *Differential cross section $d\sigma/dM_{\mu,\mu}$ (large binning). The first row gives the lower bin edge. δ_{stat} gives the statistical error and δ_{tot} the total error.*

P_t^X [GeV]	$d\sigma/dP_t^X$ [pb/GeV]	δ_{stat} [%]	δ_{tot} [%]
0	46.9	2.9	8.5
12	0.29	33	36
25	0.03	100	102
40	0.03	100	102
80	—	—	—

Table B.2: *Differential cross section $d\sigma/dP_t^X$. For details see table B.1.*

$M_{\mu,\mu}$ [GeV]	$d\sigma/dM_{\mu,\mu}$ [pb/GeV]	δ_{stat} [%]	δ_{tot} [%]
5.00	4.30	9.4	12
5.32	4.89	8.9	12
5.68	3.82	9.9	13
6.02	4.08	9.7	13
6.46	4.10	9.7	13
6.96	4.11	9.8	13
7.57	3.78	10	13
8.17	3.04	11	14
8.91	3.46	11	13
9.77	2.50	12	15
10.69	1.78	15	17
11.78	1.63	15	17
12.89	1.09	18	20
14.05	1.32	17	19
15.40	0.93	20	22
17.10	0.66	24	26
19.10	0.48	29	30
21.65	0.53	27	28
26.00	0.31	35	36
31.00	0.31	35	37
40.00	0.11	57	58
53.00	0.03	99	100
70.00	0.03	100	100
110.0	—	—	—

Table B.3: *Differential cross section $d\sigma/dM_{\mu,\mu}$ (fine binning). For details see table B.1.*

P_t^{μ} [GeV]	$d\sigma/dP_t^{\mu}$ [pb/GeV]	δ_{stat} [%]	δ_{tot} [%]
1.8	66.3	2.5	8.4
4.0	18.2	4.3	9.2
6.2	5.74	7.6	11
8.8	2.38	12	15
12.5	1.00	18	21
17.5	0.29	31	37
25.0	0.18	38	40
40.0	0.02	100	103
60.0	—	—	—

Table B.4: *Differential cross section $d\sigma/dP_t^{\mu}$. For details see table B.1.*

$W_{\gamma,p}$ [GeV]	$d\sigma/dW_{\gamma,p}$ [pb/GeV]	δ_{stat} [%]	δ_{tot} [%]
40	6.84	7.2	12
80	13.0	5.2	9.7
120	13.4	5.6	10
160	7.86	7.2	11
200	4.24	9.8	13
240	1.51	16	19
280	0.47	25	26
320	—	—	—

Table B.5: *Differential cross section $d\sigma/dW_{\gamma,p}$. For details see table B.1.*

B.2 Electroweak Muon Pair Production

$M_{\mu,\mu}$ [GeV]	$d\sigma^{ine}/dM_{\mu,\mu}$ [pb/GeV]	δ_{stat} [%]	δ_{tot} [%]
5.00	8.38	7.3	11
6.80	5.10	9.1	12
8.70	3.18	12	14
10.55	1.55	16	19
12.75	1.78	16	18
15.85	0.70	25	27
19.30	0.32	37	38
23.90	0.26	40	41
30.00	0.19	48	50
40.00	0.10	62	64
55.00	0.04	100	112
90.00	—	—	—

Table B.6: *Differential cross section $d\sigma^{ine}/dM_{\mu,\mu}$ (inelastic electroweak muon pair production). For details see table B.1.*

$M_{\mu,\mu}$ [GeV]	$d\sigma^{ela}/dM_{\mu,\mu}$ [pb/GeV]	δ_{stat} [%]	δ_{tot} [%]
5.00	11.8	6.0	10
6.80	6.39	8.1	11
8.70	3.27	11	14
10.55	2.04	15	17
12.75	1.27	18	20
15.85	0.81	23	25
19.30	0.50	30	31
23.90	0.23	44	45
30.00	0.20	49	50
40.00	—	—	—
55.00	0.03	100	107
90.00	—	—	—

Table B.7: *Differential cross section $d\sigma^{ela}/dM_{\mu,\mu}$ (elastic electroweak muon pair production). For details see table B.1.*

Bibliography

[Abe98] T. Abe *et al.*, *GRAPE-Dilepton (Version 1.0): A generator for dilepton production in e p collisions* Contributed to the Proceedings of the Workshop on Monte Carlo Generators for HERA Physics, Hamburg, Germany, 27- 30 Apr 1998. 23, 29

[Abe01] T. Abe, *GRAPE-Dilepton (Version 1.1): A generator for dilepton production in e p collisions*, Comput. Phys. Commun. **136** (2001) 126 [[arXiv:hep-ph/0012029]. 23

[Abepr] T. Abe, *private communication*. 17

[Acc93] E. Accomando and S. Petrarca, *Searching a doubly charged Higgs boson at HERA*, Phys. Lett. B **323** (1994) 212 [arXiv:hep-ph/9401242]. 22

[Acc95] E. Accomando, M. Iori and M. Mattioli, H^{--} *events in the ZEUS detector*, [arXiv:hep-ph/9505274]. 22

[ALLM] H. Abramowicz and A. Levy, *The ALLM parameterization of sigma(tot)(gamma* p): An update*, [arXiv:hep-ph/9712415]. 25, 27

[Agr92] J. Agrawal, P. H. Frampton and D. Ng, *Dilepton production in e- p and e+ e- colliders*, Nucl. Phys. B **386**, 267 (1992) [arXiv:hep-ph/9206244]. 22

[Art91] N. Arteaga-Romero, C. Carimalo and P. Kessler, *High P_t lepton pair production at e p colliders: Comparison between various production mechanisms*, Z. Phys. C **52** (1991) 289. 10, 15, 16, 18, 19, 90

[Bar91] S. P. Baranov, O. Dünger, H. Shooshtari and J. A. Vermaseren, LPAIR: A generator for lepton pair production, *in *Hamburg 1991, Proceedings, Physics at HERA, vol. 3* 1478-1482. (see HIGH ENERGY PHYSICS INDEX 30 (1992) No. 12988)* 23

[Bau92] U. Baur, J. A. Vermaseren and D. Zeppenfeld, *Electroweak vector boson production in high-energy e p collisions*, Nucl. Phys. B **375** (1992) 3. 18, 21, 30, 32

[Baw93] A. C. Bawa, K. Charchula and W. J. Stirling, *Photoproduction of large mass lepton pairs at HERA as a probe of the small x structure of the proton,* Phys. Lett. B **313** (1993) 461 [arXiv:hep-ph/9307340]. 17

[Ber87] Ch. Berger and W. Wagner, *Photon-Photon Reactions*, Phys. Rept. **146** (1987) 1. 13

[Ber02] Ch. Berger, *Elementarteilchenphysik,* Springer (2002). 14, 15

[Bet34] H. Bethe and W. Heitler, *On The Stopping Of Fast Particles And On The Creation Of Positive Electrons*, Proc. Roy. Soc. Lond. A **146** (1934) 83. 10

[Blu93] W. Blum and L. Rolandi, *Particle Detection with Drift Chambers*, Springer (1993). 65

[Bra76] F. W. Brasse *et al.*, *Parametrization Of The Q**2 Dependence Of Virtual Gamma P Total Cross-Sections In The Resonance Region*, Nucl. Phys. B **110** (1976) 413. 27

[Blo87] V. Blobel, The BOS System, DESY R1-88-01 (1988). 48, 64

[Bur95] H. Burkhardt and B. Pietrzyk, *Update of the hadronic contribution to the QED vacuum polarization*, Phys. Lett. B **356** (1995) 398 [Phys. Lett. B **513** (1995) 46]. 24

[CTEQ] H. L. Lai *et al.* [CTEQ Collaboration], *Global QCD analysis of parton structure of the nucleon: CTEQ5 parton distributions,* Eur. Phys. J. C **12** (2000) 375 [arXiv:hep-ph/9903282]. 28

[Die02] K. P. Diener, C. Schwanenberger and M. Spira, *Photoproduction of W Bosons at HERA: QCD Corrections,* [arXiv:hep-ph/0203269]. 32

[Due94] O. Dünger, *Untersuchung der Myonpaar-Erzeugung durch Photon-Photon-Kollision am e-p-Speicherring*, Interner Bericht DESY F11/F22-94-01, (1994). 23

[Dut98] B. Dutta and R. N. Mohapatra, *Phenomenology of light remnant doubly charged Higgs fields in the supersymmetric left-right model,* Phys. Rev. D **59** (1999) 015018 [arXiv:hep-ph/9804277]. 22

[Egl97] S. Egli, *Calculating Event weights in case of downscaling of trigger levels 1-4*, Internal H1-Note H1-04/97-517. 43

[Fra92] P. H. Frampton and D. Ng, *Dileptons: Present status and future prospects,* Phys. Rev. D **45** (1992) 4240. 22

[Fra98] L. L. Frankfurt, M. F. McDermott and M. Strikman, *Diffractive photoproduction of Upsilon at HERA,* JHEP **9902**, 002 (1999) [arXiv:hep-ph/9812316]. 20, 32

[GEA] R. Brun *et al.*, *Geant - Detector Description and Simulation Tool*, CERN Program Library Long Writeup W5013, CERN-DD-78-2-REV. 23

[GRV] M. Gluck, E. Reya and A. Vogt, *Dynamical parton distributions revisited*, Eur. Phys. J. C **5** (1998) 461 [arXiv:hep-ph/9806404]. 28

[H197a] H1 Collaboration, *The H1 detector at HERA*, Nucl. Instrum. Meth. A **386** (1997) 310. 35

[H197b] H1 Collaboration, *The Tracking, calorimeter and muon detectors of the H1 experiment at HERA*, Nucl. Instrum. Meth. A **386** (1997) 348. 35

[H198] H1 Collaboration, *Observation of events with an isolated high energy lepton and missing transverse momentum at HERA*, Eur. Phys. J. C **5** (1998) 575 [arXiv:hep-ex/9806009]. 6, 89

[H199] H1 Collaboration, *Measurement of open beauty production at HERA*, Phys. Lett. B **467** (1999) 156 [Erratum-ibid. B **518** (2001) 331] [arXiv:hep-ex/9909029]. 32

[H100] H1 Collaboration, *Elastic photoproduction of J/psi and Upsilon mesons at HERA*, Phys. Lett. B **483** (2000) 23 [arXiv:hep-ex/0003020]. 6

[H102a] H1 Collaboration, *Diffractive photoproduction of psi(2S) mesons at HERA*, [arXiv:hep-ex/0205107]. 73

[H102b] H1 Collaboration, *Search for Doubly Charged Higgs Production at HERA*, Conference paper no. 1020 subm. to ICHEP 2002 (Amsterdam), (http://www-h1.desy.de/h1/www/publications/htmlsplit/H1prelim-02-162.long.html). 92

[H102c] H1 Collaboration, *Muon Pair Production in ep collisions at HERA*, Conference paper no. 1021 subm. to ICHEP 2002 (Amsterdam), (http://www-h1.desy.de/h1/www/publications/htmlsplit/H1prelim-02-051.long.html). 7

[H102d] H1 Collaboration, *Observation of isolated leptons with missing P_t and comparision to W production at HERA*, Conference paper no. 1022 subm. to ICHEP 2002 (Amsterdam), (http://www-h1.desy.de/h1/www/publications/htmlsplit/H1prelim-01-051.long.html). 6, 96

[H102e] H1 Collaboration, *Multi-electron Production at High Transverse Momentum in ep collisions at HERA*, Conference paper no. 1019 subm. to ICHEP 2002 (Amsterdam), (http://www-h1.desy.de/psfiles/confpap/ICHEP2002/H1prelim-02-052.ps). 6, 96

[H1SWa] H. Albrecht, M. Erdmann, P. Schleper, *A guide to H1PHAN an H1 physics analysis package*, H1 internal software manual (1997). 64

[HM84] F. Halzen and A. D. Martin, *Quarks and Leptons: An Introductory Course in Modern Particle Physics*, John Wiley & Sons, (1984). 26

[Hei98] B. Heinemann, *Measurement of Charged Current and Neutral Current Cross Sections in Positron-Proton Collisions at $\sqrt{s} = 300$ GeV*, Ph.D. Thesis, University of Hamburg (1999). 45

[Hof99] D. Hoffmann and L. Favart, *Lepton pair Monte Carlo generators for HERA physics*, IIHE-99-01 *Contributed to the Proceedings of the Workshop on Monte Carlo Generators for HERA Physics, Hamburg, Germany, 27- 30 Apr 1998.* 29

[Hof00] D. Hoffmann, *Zwei-Elektron-Ereignisse im H1-Detektor*, Ph.D. Thesis, University of Hamburg (2000). 31

[Ing97] G. Ingelman, J. Rathsman and G. A. Schuler, *AROMA 2.2 - A Monte Carlo Generator for Heavy Flavour Events in ep Collisions*, Comput. Phys. Commun. **101** (1997) 135 [hep-ph/9605285]. 32

[Ish93] T. Ishikawa, T. Kaneko, K. Kato, S. Kawabata, Y. Shimizu and H. Tanaka [MINAMI-TATEYA group Collaboration], *GRACE manual: Automatic generation of tree amplitudes in Standard Models: Version 1.0*, KEK-92-19. 23

[Itt98] H. Itterbeck, *Techniques and Physics of the Central-μ-Trigger System of the H1-Detector at Hera*, Ph.D. Thesis, RWTH Aachen, PITHA 98/01, (1998). 45, 46, 49

[JB79] F. Jaquet, A. Blondel, *Proceedings of the workshop: Study for an ep facility in Europe*, DESY 79-048 (1979) 391. 77

[Kae00] H.C. Kaestli, *Muon Pair Production with high Invariant Mass in e+p-Collisions at HERA*, Ph.D. Thesis, ETH Zuerich, ETHZ-IPP I.R.2000-04 (2000). 23

[Kle92] C. Kleinwort, U.-P. Krueger, *Track Reconstruction in the Iron*, H1 Software Note 35, (1992). 64

[Kes75] P. Kessler, *The Williams-Weizsäcker Methoa and Similiar Methods in Quantum Electrodynamics* Acta Phys. Austr. **41**, (1975) 141-188. 13

[Keu98] C. Keuker, *The Central Muon Data Acquisition of the H1 Experiment and its Application*, Ph.D. Thesis, RWTH Aachen, Pitha 98/01 (1998). 65

[Kim01] S. M. Kim, *A test of SU(15) at HERA using the HELAS program*, Mod. Phys. Lett. A **16** (2001) 2115 [arXiv:hep-ph/0111071]. 22

[Kru01] K. Krüger, *Photoproduction of J/Ψ Mesons at Medium and Low Elasticities at Hera*, Ph.D. Thesis University of Hamburg (2001). 51, 65

[Lan98] U. Langenegger, *A Measurement of the Beauty and Charm Production Cross Section at the ep Collider HERA*, Ph.D. Thesis, ETH Zürich, (1998). 64, 72

[Lei02] B. Leissner, *Muon Pair Production*, X International Workshop on Deep Inelastic Scattering (DIS2002), Cracow (2002). 7

[Lep80] G. P. Lepage, *Vegas: An Adaptive Multidimensional Integration Program*, CLNS-80/447. 33

[Lev91] G. Levman, *Muon pair production by two photon collisions at HERA*, In *Hamburg 1991, Proceedings, Physics at HERA, vol. 1* 623-628. (see HIGH ENERGY PHYSICS INDEX 30 (1992) No. 12988). 17, 90

[Lev02] *internal H1 information*, 2002. 86

[Lis93] B. List, *Diffraktive J/Ψ -Produktion in Elektron-Positron-Stößen am Speicherring HERA*, Diploma Thesis, Technische Univeristät Berlin, H1-internal note (H1-10/93-319) (1993). 32

[Mal00] N. Malden, *W production in ep collisions*, Ph.D. Thesis, University of Manchester, (2000). 6, 89

[Meh02] A. Mehta, *private communication*, (2002). 87

[Moh00] S. Mohrdiek, *Inelastische J/Psi-Erzeugung in Elektroproduktion am H1-Experiment bei HERA*, Ph.D. Thesis, University of Hamburg (2000). 60, 65, 66

[Muc00] A. Mücke, R. Engel, J. P. Rachen, R. J. Protheroe and T. Stanev, *Monte Carlo simulations of photohadronic processes in astrophysics*, Comput. Phys. Commun. **124** (2000) 290 [arXiv:astro-ph/9903478]. 23

[Olz00] J. Olzem, *Untersuchungen zur Datenqualität des Myon-Detektors im H1-Experiment*, Diploma Thesis, RWTH Aachen, (2000). 45, 47

[OPA93] OPAL Collaboration, *A Study of muon pair production and evidence for tau pair production in photon-photon collisions at LEP*, Z. Phys. C **60** (1993) 593. 10, 13

[OPA01] OPAL Collaboration, *Search for doubly charged Higgs bosons with the OPAL detector at LEP*, Phys. Lett. B **526** (2002) 221 [arXiv:hep-ex/0111059]. 22, 92

[PDG96] R. M. Barnett *et al.* [Particle Data Group Collaboration], *Review of particle physics. Particle Data Group*, Phys. Rev. D **54** (1996) 1. 91

[PDG] D. E. Groom *et al.* [Particle Data Group Collaboration], *Review Of Particle Physics*, Eur. Phys. J. C **15** (2000) 1. 18, 19

[Plo93] H. Plothow-Besch, *PDFLIB: A Library of all available parton density functions of the nucleon, the pion and the photon and the corresponding alpha-s calculations*, Comput. Phys. Commun. **75** (1993) 396. 28

[Puk99] A. Pukhov *et al.*, *CompHEP: A package for evaluation of Feynman diagrams and integration over multi-particle phase space. User's manual for version 33*, [arXiv:hep-ph/9908288]. 33

[Sak69] J. J. Sakurai, *Vector Meson Dominance And High-Energy Electron Proton Inelastic Scattering*, Phys. Rev. Lett. **22** (1969) 981. 16

[Sch93] G. A. Schuler and T. Sjöstrand, *Towards a complete description of high-energy photoproduction*, Nucl. Phys. B **407** (1993) 539. 16

[Sch01] F.P. Schilling, *Diffractive Jet Production in Deep-Inelastic e+p Collisions at HERA*, Ph.D. Thesis, University of Heidelberg, (2001). 73

[Smi01] D. Schmidt, *Diffraktive Photoproduktion von Charmonium im H1-Detektor bei HERA*, Ph.D. Thesis, University of Hamburg, (2001). 65, 73, 87

[Smi94] G. Schmidt, *Nachweis von Myonen im H1-Kalorimeter*, Diploma Thesis, University of Hamburg, H1-IN-341, (1994). 65

[Smi02] C. Schmitz, *Elektroproduktion von Myon-Paaren im Massenbereich der Υ-Resonanz*, Diploma Thesis, RWTH Aachen, (2002). 20, 73

[Swa98] A. Schwank, *Effizienzbestimmung von Detektorkomponenten des H1-Experiments mit Hilfe kosmischer Strahlung*, Diploma Thesis, University of Hamburg (1998). 66

[Sjo01] T. Sjöstrand, L. Lonnblad and S. Mrenna, *PYTHIA 6.2: Physics and manual*, [arXiv:hep-ph/0108264]. 23, 33

[SY72] A. Suri and D. Yennie, *The Space-Time Phenomenology of Phton Absorption and Inelastic Electron Scattering*, Ann. Phys. **72**, 243 (1972). 27

[Swa89] M. L. Swartz, *Limits On Doubly Charged Higgs Bosons And Lepton Flavor Violation*, Phys. Rev. D **40** (1989) 1521. 92

[Val02] C. Valleè, *Lepton pairs at high transverse momentum at HERA*, X International Workshop on Deep Inelastic Scattering (DIS2002), Cracow (2002). 6, 31, 91, 96

[Ver83] J. A. Vermaseren, *Two Photon Processes At Very High-Energies*, Nucl. Phys. B **229** (1983) 347. 23

[Wes00] L. West, *How to use the Heavy Flavour Working Group Track, Muon and Electron Selection Code*, H1 internal software manual (2000). 64

[Wil98] L. Willmann *et al.*, *New bounds from searching for muonium to antimuonium conversion,*
Phys. Rev. Lett. **82** (1999) 49 [arXiv:hep-ex/9807011]. 22

[www1] T. Abe, *GRAPE*, http://www.awa.tohoku.ac.jp/∼tabe/grape/. 25

[Zeu93] ZEUS Collaboration, *The ZEUS Detector at Hera, Status Report 1993*, DESY, Hamburg
(1993). 35

[Zeu98] ZEUS Collaboration, *Measurement of elastic Upsilon photoproduction at HERA*, Phys.
Lett. B **437** (1998) 432 [arXiv:hep-ex/9807020]. 6

[Zeu00] ZEUS Collaboration, *Search for events with isolated high-energy leptons and missing
transverse momentum at HERA*, Conference paper no. 1041 subm. to ICHEP 2000 (Os-
aka), (http://www-zeus.desy.de/physics/phch/conf/osaka_paper.html#EXO) 6

Curriculum Vitae

Status	Name:	Boris Leißner
	Date of Birth:	01/11/1973
	Place of Birth:	Rheydt, Germany
	Marital Status:	Unmarried
	Nationality:	German

Education	02/99	-	10/02	Ph.D. in Physics at the H1 experiment
	10/93	-	12/98	Diplom in Physics at the RWTH Aachen
	08/84	-	06/93	St. Ursula Gymnasium Geilenkirchen

Activities	01/02	-	12/02	Scientific associate
				I. Physikalisches Institut der RWTH Aachen
	02/99	-	12/01	DFG Graduate College Scholarship
	08/97	-	12/98	Student associate
				I. Physikalisches Institut der RWTH Aachen
	03/96	-	08/97	Student associate
				Institut für Bauforschung der RWTH Aachen

Danksagung

Allen die mich bei der Durchführung und Erstellung dieser Arbeit unterstützt haben möchte ich herzlich danken.

Herrn Professor Christoph Berger gilt mein besonderer Dank für die Vergabe des interessanten und vielseitigen Promotionsthemas und seine effektive Unterstützung. Herrn Professor Günther Flügge danke ich für sein Engagement als Berichter.

Für viel Geduld und stete Hilfsbereitschaft sei Dr. Klaus Rabbertz gedankt. Dr. Jürgen Scheins bereicherte in erstaunlich vielen Dimensionen den physikalischen Alltag. Unendliche Diskussionen konnte ich mit Dr. Sascha Caron führen, dessen verläßliche Unterstützung einen großen Beitrag zum Gelingen dieser Arbeit darstellt.

Desweiteren möchte ich mich bei allen Mitgliedern der HIP-Gruppe bedanken, insbesondere bei den beiden Gruppenleitern Dr. Andrew Mehta und Dr. Cristinel Diaconu. Feinheiten des Englischen vermittelte mir Dr. Nicholas Malden, und mit vielen zahlreichen Hinweisen standen mir Professor Joachim Meyer, Dr. Hans-Ulrich Martyn, Gilles Frising und Martin Wessels zur Seite. Eine schöne fruchtbare Zusammenarbeit erlebte ich mit Jan Olzem und Carsten Schmitz.

Natürlich geht auch ein Dank an H1AACI+III: Adil Aktas, Carlo Duprel, Lars Finke, Dr. Thomas Hadig, Thomas Kluge, Linus Lindfeld, Dr. J.J. Lomo, Dr. Peer-Oliver Meyer, Markus Stoye, Ingo Strauch, Anja Vest, Dr. Markus Wobisch ... und alle anderen, die ich womöglich vergessen habe.

Karin und Jürgen Leißner danke ich, daß sie mich immer in allen Lebenslagen maßgeblich unterstützt haben und somit auch einen großen Beitrag zum Erfolg dieser Dissertation leisteten.

Ganz besonders danke ich Dr. Elisa Bernardini für ihr überaus großes Verständnis und natürlich auch für interessante Einblicke in die Welt noch bizarrerer Teilchen.